TIME-DOMAIN ANALYSIS OF FRACTIONAL WAVE EQUATIONS AND IMPLEMENTATIONS OF PERFECTLY MATCHED LAYERS IN NONLINEAR ULTRASOUND SIMULATIONS

By

Xiaofeng Zhao

A DISSERTATION

Submitted to
Michigan State University
in partial fulfillment of the requirements
for the degree of

Electrical Engineering - Doctor of Philosophy

2018

ABSTRACT

TIME-DOMAIN ANALYSIS OF FRACTIONAL WAVE EQUATIONS AND IMPLEMENTATIONS OF PERFECTLY MATCHED LAYERS IN NONLINEAR ULTRASOUND SIMULATIONS

By

Xiaofeng Zhao

The attenuation of ultrasound propagating in human tissue follows a power law with respect to frequency that is modeled by several different fractional partial differential equations. These models for the power law attenuation of medical ultrasound have been developed using fractional calculus, where each contains one or more time-fractional or space-fractional derivatives. To demonstrate the similarities and differences in the solutions to causal and noncausal fractional partial differential equations, time-domain Green's functions are calculated numerically for the fractional wave equations. For three time-fractional wave equations, namely the power law wave equation, the Szabo wave equation, and the Caputo wave equation, these Green's functions are evaluated for water with a power law exponent of $y = 2$, liver with a power law exponent of $y = 1.139$, and breast with a power law exponent of $y = 1.5$. Simulation results show that the noncausal features of the numerically calculated time-domain response are only evident in the extreme nearfield region and that the causal and the noncausal Green's functions converge to the same time-domain waveform in the farfield. When noncausal time-domain Green's functions are convolved with finite-bandwidth signals, the noncausal behavior in the time-domain is eliminated, which suggests that noncausal time-domain behavior only appears in a very limited set of circumstances and that these time-fractional models are equally effective for most numerical calculations.

For the calculation of space-fractional wave equations, time-domain Green's functions are numerically calculated for two space-fractional models, namely the Chen-Holm and Treeby-Cox wave equations. Numerical results are computed for these in breast and liver. The results show that these two space-fractional wave equations are causal everywhere. Away

from the origin, the time-domain Green's function for the dispersive Treeby-Cox space-fractional wave equation is very similar to the time-domain Green's functions calculated for the corresponding time-fractional wave equations, but the time-domain Green's function for the nondispersive Chen-Holm space-fractional wave equation is quite different. To highlight the similarities and differences between these, time-domain Green's functions are compared and evaluated at different distances for breast and liver parameters. When time-domain Green's functions are convolved with finite-bandwidth signals, the phase velocity difference in these two space-fractional wave equations is responsible for a time delay that is especially evident in the farfield.

The power law wave equation is also utilized to implement a perfectly matched layer (PML) for numerical calculations with the Khokhlov - Zabolotskaya - Kuznetsov (KZK) equation. KZK simulations previously required a computational grid with a large radial distance relative to the aperture radius to delay the reflections from the boundary. To decrease the size of the computational grid, an absorbing boundary layer derived from the power law wave equation. Simulations of linear pressure fields generated by a spherically focused transducer are evaluated for a short pulse. Numerical results for linear KZK simulations with and without the absorbing boundary layer are compared to the numerical results with a sufficiently large radial distance. Simulation results with and without the PML are also evaluated, where these show that the absorbing layer effectively attenuates the wavefronts that reach the boundary of the computational grid.

ACKNOWLEDGEMENTS

The last six years have been a very rewarding experience. I can only make such a statement due to the diligence of others who have made a profound impact in my life.

First and foremost, I would like to express my sincere gratitude to Dr. Robert McGough for his gracious support throughout my entire Ph.D. program. Dr. McGough's creativity, enthusiasm, and problem-solving acumen always inspired me in pursuing every research goal. He has been a great mentor and has always made sure I understand the importance of good scientific work. He has made a great deal of effort to ensure my success as a Ph.D. student. I am very grateful for his never-ending help, patience, understanding, and encouragement in past few years.

I would also like to thank my committee members: Dr. Edward Rothwell, Dr. Selin Aviyente, and Dr. Brian Feeny for their mentorship and invaluable advice. I really appreciate their guidance in my Ph.D. program and instruction in my course study of Electromagnetic Fields and Time-Frequency Wavelet Analysis.

Furthermore, I would like to thank my colleagues from the Biomedical Ultrasonics and Electromagnetics Laboratory: James Kelly, Drew Murray, Kirk Sales, Peter Beard and Leslie P. Thomas. It is my honor to have the opportunity to work with all of them.

In addition, I would like to give special thanks to Bin Fan, Yiqun Yang, Pedro Nariyoshi and Jie Li. Thank you for your support, company, and help over the past few years.

Finally, I would like to thank my family for all of their encouragement and support throughout my life and studies. To my mom and dad, the things I have done in my life are only possible as result of your sacrifice. I moved to an unknown country and could not accompany you in the last few years. I have not always been the best son or cherished this sacrifice. I want to let you know that I have learned from my mistakes that I have made in life and that I love you from the bottom of my heart.

TABLE OF CONTENTS

LIST OF FIGURES

Chapter 1

Introduction

1.1 Ultrasound attenuation in soft tissue

As sound waves propagate, the medium is temporarily displaced in a direction parallel (longitudinal wave) or perpendicular (transverse wave) to the direction of energy transport and then the medium returns to the equilibrium state. When ultrasound travels through a medium, the intensity diminishes with distance. In a lossless medium, the amplitude is only reduced by the spreading of the wave. However, when ultrasound propagates through soft tissue, the amplitude is reduced as a function of propagation distance, and the center frequency of the signal is also downshifted by attenuation. As indicated by Laugier and Haïat [1], Goss et al. [2], and Parker [3], the two main mechanisms that contribute to ultrasound attenuation are absorption and scattering.

Absorption is the conversion of the sound energy to other forms of energy [4, 5], especially heat as a result of friction between the vibrating particles that transmit the acoustic wave within soft tissue. In homogeneous viscous media, the viscous forces between neighboring particles moving with different velocities are the major source of acoustic wave absorption. Acoustic wave attenuation is also caused by scattering, which describes the redirection of the incident wave in multiple directions [6, 7]. In heterogeneous media, where the physical properties such as density or sound speed are different from those of the surrounding medium, scattering also redirects the acoustic energy.

In three-dimensional (3D) space, the amplitude decay and attenuation of ultrasound are mathematically described by $p(r) = \frac{p_0 e^{-\alpha(f)r}}{r}$ for the attenuation given by $\alpha(f) = \alpha_0 |f|^y$, where p is the pressure, α_0 is the attenuation coefficient, r is the distance in 3D, f is the frequency, and y is the power law exponent. For instance, in water, the power law exponent y is equal to 2. However, in most biological tissues, the measured power law exponents y are within the range of $0.7 \leq y \leq 1.5$ for the range of frequencies utilized in medical ultrasound [8]. For example, measured values for the power law exponent are $y = 1.139$ in human liver [9] and $y = 1.5$ in human breast [10]. The power law exponents and attenuation coefficients vary for different tissues, and measurements of these parameters have been widely evaluated for medical ultrasound in human tissue [11, 12, 13].

1.2 Nonlinear ultrasound

The fundamental equations of nonlinear ultrasound are derived from the three constitutive relations, namely the equation of motion, the continuity equation, and the equation of state [14]. For small pressure amplitudes, the linearized versions of these three fundamental equations are combined to produce a linear wave equation. However, when the pressure amplitudes are sufficiently large, the second order terms in these fundamental equations must be retained, and the combination of the three constitutive relations yields a nonlinear wave equation. The amount of nonlinearity in a material through which a finite-amplitude ultrasonic wave propagates is expressed by the nonlinearity parameter B/A. The values of A and B are the coefficients of the first and second order terms of the Taylor series expansion for the equation of state, which relates the pressure to the density. Some values of B/A in biological tissues are given by Wells [15].

Some common models that describe nonlinear ultrasound propagation include the Westervelt equation, the Khokhlov-Zabolotskaya-Kuznetsov (KZK) equation, and Burgers equation. A general wave equation that accounts for nonlinearity up to second-order is given by the Westervelt equation [16]. After a parabolic approximation is applied, the Westervelt equation

reduces to the KZK equation, which accounts for the combined effects of nonlinearity, diffraction, and absorption in directional sound beams. Solutions to this equation are commonly used to model problems in nonlinear acoustics. Several numerical approaches that solve the KZK equation have been proposed by Lee and Hamilton [17], Cleveland [18], and Berntsen [19]. When the diffraction term is discarded, the KZK equation reduces to Burgers equation, which describes the combined effects of nonlinearity and attenuation on the propagation of progressive plane waves. Solutions to Burgers equation can be obtained with several different methods [20, 21].

Nonlinear wave propagation has been widely analyzed in the medical ultrasound field. Two common applications include high intensity focused ultrasound (HIFU) in therapeutic ultrasound [22, 23, 24] and harmonic imaging in diagnostic ultrasound [25, 26, 27]. HIFU generates high intensity pressure fields in the focal zone to heat tumors or break up kidney stones [28]. Compared to diagnostic ultrasound, HIFU uses higher energies and lower frequencies. In harmonic imaging, since scattering and first reflections are reduced in the second harmonic, the resulting images provide better contrast, better resolution, and diminished effects of undesirable sidelobes.

1.3 Fractional derivative operators

Fractional derivative operators are applied widely in the field of fractional calculus. A variety of fractional derivatives are defined to replace the integer order derivative, including the Riemann–Liouville fractional derivative [29], the Caputo fractional derivative [30], the Atangana–Baleanu derivative [31], the Katugampola fractional derivative [32], and so on. Two of these fractional derivative operators are utilized here, namely the Riemann–Liouville fractional derivative and the Caputo fractional derivative [33]. The Riemann–Liouville

fractional derivative is defined by

$$D_L^y f(t) = \begin{cases} \frac{1}{\Gamma(n-y)} \frac{d^n}{dt^n} \int_a^t \frac{f(\tau)}{(t-\tau)^{y+1-n}} d\tau, & n-1 < y < n \subset \mathrm{N}, \\ \frac{d^n}{dt^n} f(t), & y = n \subset \mathrm{N}, \end{cases} \tag{1.1}$$

where $y > 0$, $t > a$, and $y, a, t \subset \mathrm{R}$. The gamma function, which frequently appears in fractional calculus, is defined as

$$\Gamma(z) = \int_0^\infty t^{z-1} e^{-t} dt. \tag{1.2}$$

The Caputo fractional derivative takes the following form:

$$D_C^y f(t) = \begin{cases} \frac{1}{\Gamma(n-y)} \int_a^t \frac{f^{(n)}(\tau)}{(t-\tau)^{y+1-n}} d\tau, & n-1 < y < n \subset \mathrm{N}, \\ \frac{d^n}{dt^n} f(t), & y = n \subset \mathrm{N}. \end{cases} \tag{1.3}$$

These two fractional derivatives are similar, where the main difference is the order in which the differentiation and integration operations are performed. For a fractional derivative operator, the derivative of a function evaluated at a point is no longer a local property, so additional knowledge of previous states is required in either time or space.

The properties of integer derivatives for Fourier and Laplace transforms are readily extended to fractional derivatives [33]. The 1D Laplace transform for the integer derivative is defined as

$$\mathcal{L}\{f(t)\} = \int_0^\infty e^{-st} f(t)\, dt. \tag{1.4}$$

This is extended to the fractional Riemann Liouville derivative as [29]

$$\mathcal{L}\{D_L^y f(t)\} = s^y F(s) - \sum_{k=0}^{n-1} s^k \left[D_L^{y-k-1} f(t) \right]_{t=0} \tag{1.5}$$

and to the Caputo derivative as [30]

$$\mathcal{L}\left\{D_C^y f\left(t\right)\right\} = s^y F\left(s\right) - \sum_{k=0}^{n-1} s^{y-k-1} f^{(k)}\left(0\right). \tag{1.6}$$

For the Fourier transform in 1D

$$\mathcal{F}\left\{f\left(t\right)\right\} = \int_{-\infty}^{\infty} f\left(t\right) e^{-j\omega t} dt, \tag{1.7}$$

both Riemann–Liouville and Caputo derivatives are the same [34, 35]:

$$\mathcal{F}\left\{D_L^y f\left(t\right)\right\} = \left(j\omega\right)^y F\left(\omega\right), \tag{1.8}$$

$$\mathcal{F}\left\{D_C^y f\left(t\right)\right\} = \left(j\omega\right)^y F\left(\omega\right). \tag{1.9}$$

1.4 Dispersion relations for fractional wave equations

When the effects of attenuation are included through the term $\varepsilon L_{r,t}\left(p\right)$, the wave equation becomes

$$\nabla^2 p - \frac{1}{c_0^2}\frac{\partial^2 p}{\partial t^2} - \varepsilon L_{r,t}\left(p\right) = 0, \tag{1.10}$$

where the fractional operator $\varepsilon L_{r,t}\left(p\right)$ may be either time-fractional or space-fractional or both. After Fourier transforms are evaluated in both time and space domains, the dispersion relation for Eq. 1.10 is given by

$$-k^2 + \frac{\omega^2}{c_0^2} - \varepsilon \tilde{L}\left(k, \omega\right) = 0. \tag{1.11}$$

When $L_{r,t}(p)$ contains only time-fractional derivatives, $\varepsilon\tilde{L}(k,\omega) = \varepsilon\tilde{L}(\omega)$, and the analytical expression for the wavenumber is then represented by

$$k(\omega) = \sqrt{\frac{\omega^2}{c_0^2} - \varepsilon\tilde{L}(\omega)}. \tag{1.12}$$

The relationship of phase velocity and attenuation is then obtained from the real and imaginary parts of Eq. 1.12.

For the general case when the loss term $\varepsilon\tilde{L}(k,\omega)$ contains at least one space-fractional operator, the wavenumber in Eq. 1.11 is calculated with the binomial approximation

$$k(\omega) \approx \frac{\omega}{c_0}\left[1 - \frac{c_0^2}{2\omega^2}\varepsilon\tilde{L}(k,\omega) - \frac{c_0^4}{8\omega^4}\varepsilon^2\tilde{L}^2(k,\omega) - \frac{c_0^6}{16\omega^6}\varepsilon^3\tilde{L}^3(k,\omega) + \ldots\right]. \tag{1.13}$$

The right-hand side of Eq. 1.13 includes several terms that contains $\tilde{L}(k,\omega)$, which is a function of k. To obtain an expression for the wavenumber $k(\omega)$ that is independent of k on the right-hand side, further approximations are required.

1.4.1 First order approximation

If $O(\varepsilon^2)$ and higher order terms in Eq. 1.13 are discarded, and the first-order approximation for Eq. 1.13 is then given by

$$k(\omega) \approx \frac{\omega}{c_0} - \frac{c_0}{2\omega}\varepsilon\tilde{L}\left(k^+,\omega\right), \tag{1.14}$$

where k^+ is obtained by setting $\tilde{L}(k,\omega) = 0$, which yields $k^+ \approx \frac{\omega}{c_0}$. This expression is substituted back to Eq. 1.14 and the $O(\varepsilon)$ terms are ignored, which yields

$$k(\omega) \approx \frac{\omega}{c_0} - \frac{c_0}{2\omega}\varepsilon\tilde{L}\left(\frac{\omega}{c_0},\omega\right). \tag{1.15}$$

1.4.2 Second order approximation

To obtain a more accurate approximation for the wavenumber, third order and higher terms are discarded from Eq. 1.13. Then, the second-order approximation is given by

$$k(\omega) \approx \frac{\omega}{c_0} - \frac{c_0}{2\omega}\varepsilon\tilde{L}\left(k^+,\omega\right) - \frac{c_0^3}{8\omega^3}\varepsilon^2\tilde{L}^2\left(k^+,\omega\right). \tag{1.16}$$

Similarly, k^+ is approximated by substituting ω/c_0 into Eq. 1.16

$$k^+ \approx \frac{\omega}{c_0} - \frac{c_0}{2\omega}\varepsilon\tilde{L}\left(\frac{\omega}{c_0},\omega\right), \tag{1.17}$$

and then terms that are third order or higher in ε are discarded.

1.5 Thesis structure

For certain time-fractional and space-fractional models, exact and approximate time-domain Green's functions have been derived and evaluated numerically. More accurate expressions for the phase velocity and attenuation are also derived for several fractional calculus models. To demonstrate some of the similarities and differences in these fractional partial differential equations, causality is analyzed for each of these, the time-domain Green's functions are compared, and full width at half maximum (FWHM) values for each time-domain Green's function are evaluated for breast and liver models.

Chapter 2 numerically evaluates time-domain Green's functions for three time-fractional models, namely the power law wave equation, the Szabo wave equation, and the Caputo wave equation. These Green's functions are evaluated for water with a power law exponent of $y = 2$, breast with a power law exponent of $y = 1.5$, and liver with a power law exponent of $y = 1.139$. The causality of each fractional wave equation is analyzed, and the time-domain Green's functions for these three time-fractional models are compared at different distances. To demonstrate the effects of power law attenuation and dispersion on transient excitations, a

three-cycle Hanning-weighted pulse is also convolved with the time-domain Green's functions for these three time domain Green's functions.

Chapter 3 evaluates improved approximations for the frequency-dependent phase velocity and attenuation that were derived from two space-fractional models, namely the Chen-Holm and Treeby-Cox space-fractional wave equations, and these are evaluated using parameters for breast and liver. After the causality of the two space-fractional models is established, the amplitudes and FWHM values of the time-domain Green's functions are evaluated at short distances from the origin. In addition, a three-cycle Hanning weighted pulse is convolved with each time-domain Green's function to show how differences in these Green's functions influence the results for a finite bandwidth excitation.

Chapter 4 introduces new expressions that describe perfectly matched layers (PML) for numerical simulations with the transient KZK equation. Artificial attenuation in these new PMLs is implemented through terms derived from the power law wave equation with $y = 0$ and $y = 2$. These expressions are further simplified by retaining only one term, which is sufficient to reduce reflections from the radial boundary. For a spherically focused transducer with aperture radius $a = 1.5$ cm and radius of curvature $R = 6$ cm, simulations in both linear lossless and nonlinear media validate the effectiveness of these new PMLs. Similar simulations are then evaluated for the continuous wave KZK equation in both linear lossless and nonlinear media.

Chapter 2

Time fractional wave equations[1]

2.1 Introduction

The attenuation of compressional ultrasound waves in soft tissue is described by a power law of the form $\alpha(f) = \alpha_0 |f|^y$, where f is the frequency in MHz, α_0 is the attenuation constant in Np/m/Hz^y or dB/m/Hz^y, and y is the power law exponent. Examples of measured values for the power law exponent are $y = 2$ in water, $y = 1.139$ in human liver [9], and $y = 1.5$ in human breast [10]. Additional values for mammalian tissues with various power law exponents are tabulated in the book by Duck [8], and other attenuation values are compiled in papers by Goss et al. [36, 37].

The corresponding wave equations that describe power law attenuation in soft tissue utilize fractional derivatives, which are non-integer order derivatives. These fractional derivatives are often time-fractional [38, 39, 40], although space-fractional derivatives are also used [41, 42]. Examples of time-fractional wave equations that model the attenuation and dispersion of ultrasound in soft tissue include the Szabo wave equation [38], the Caputo wave equation [30], and the power law wave equation [39]. The Szabo and power law wave equations were developed for medical ultrasound applications, and the Caputo wave equation [30] was originally defined for applications in geophysics and then independently considered by Wismer as a model for attenuation and dispersion in soft tissue [40].

[1]Reproduced from X. Zhao and R. J. M Gough, Time-domain comparisons of power law attenuation in causal and noncausal time-fractional wave equations, *The Journal of the Acoustical Society of America*, 139(5):30213031, 2016, with the permission of the Acoustical Society of America.

These time-fractional wave equations are particularly amenable to analytical methods for analyzing causality, including the Paley-Wiener criterion [43], Kramers-Kronig analysis [44], and a time causal theory [38]; however, inconsistent conclusions are often reached with different methods, especially for power law exponents $y \geq 1$. In an effort to resolve some of these apparent inconsistencies, time-domain Green's functions are calculated numerically for the Blackstock wave equation, the Stokes wave equation, the Szabo wave equation, the Caputo wave equation, and the power law wave equation. In addition, a three-cycle Hanning-weighted pulse is convolved with each of these to show the effects of causal and noncausal Green's functions on the calculated signals. The results show that noncausal behavior is only evident very close to the source in time-domain Green's function calculations, that this noncausal behavior is no longer evident after convolution with a short pulse, and that time-domain calculations with these causal and noncausal time-fractional models converge a short distance from the source.

2.2 Power law attenuation and dispersion

The frequency-dependent attenuation $\alpha(\omega)$ of ultrasound in soft tissue is described by the power law [45]

$$\alpha\left(\omega\right) = \alpha_0 \left|\omega\right|^y, \tag{2.1}$$

where y is the power-law exponent, α_0 is the attenuation constant, and ω is the angular frequency in radians/second. The corresponding frequency-dependent sound speed (dispersion) $c(\omega)$ satisfies [45]

$$\frac{1}{c\left(\omega\right)} = \frac{1}{c_0} + \alpha_0 \tan\left(\frac{\pi y}{2}\right) \left|\omega\right|^{y-1}. \tag{2.2}$$

In Eq. 2.2, c_0 is the sound speed at $\omega = 0$ for $1 < y \leq 2$, and c_0 is the sound speed at $\omega = \infty$ for $0 \leq y < 1$. When $y = 2$, Eq. 2.2 is nondispersive because the ω dependence in Eq. 2.2 disappears. For the numerical calculations that follow, the attenuation constant α_0 with units Np/cm/MHz^y is multiplied by 100 and divided by 10^{6y} and $(2\pi)^y$ to convert

cm into m, MHz into Hz, and frequency in Hz into angular frequency in radians/second, respectively.

2.3 The Szabo wave equation

For an attenuation constant α_0 with units Np/m/Hz^y, the Szabo wave equation [38] is given by

$$\nabla^2 p - \frac{1}{c_0^2}\frac{\partial^2 p}{\partial t^2} - \frac{2\alpha_0}{c_0 \cos(\pi y/2)}\frac{\partial^{y+1} p}{\partial t^{y+1}} = 0, \tag{2.3}$$

where p represents the pressure in Pa and t is the time in seconds. The Szabo wave equation is a time-fractional extension of the Blackstock wave equation [46], where the third term approximately describes the effects of power law attenuation and dispersion in Eqs. 2.1 and 2.2 over the range of frequencies where the smallness approximation [38] holds. There is no known exact time-domain Green's function for the Szabo wave equation, but the 3D frequency-domain Green's function for the Szabo wave equation is

$$G(r,\omega) = \frac{e^{-\frac{r}{c_0}\sqrt{-\omega^2 + \frac{2\alpha_0 c_0}{\cos(\pi y/2)}(j\omega)^{y+1}}}}{4\pi r} \tag{2.4}$$

for frequencies $\omega \geq 0$, where $r = \sqrt{x^2+y^2+z^2}$ is the distance from a point source at the origin to an observation point at (x, y, z).

The phase velocity and attenuation are derived by solving the dispersion relation

$$k^2 = \frac{\omega^2}{c_0^2} - \frac{2\alpha_0}{c_0 \cos(\pi y/2)}(-j\omega)^{y+1} \tag{2.5}$$

for k. By taking the square root of Eq. 2.5 and utilizing the binomial approximation, an approximate expression for the wave number is obtained

$$\begin{aligned} k \approx \tfrac{\omega}{c_0}\left\{1 + j\alpha_0 c_0 \left[1 - j\tan(\pi y/2)\right]\omega^{y-1}\right\} \\ + \tfrac{\alpha_0^2 c_0}{2}\left[1 - j2\tan(\pi y/2) - \tan^2(\pi y/2)\right]\omega^{2y-1}. \end{aligned} \tag{2.6}$$

The approximate phase velocity is then extracted from the real part of the wavenumber divided by ω

$$\frac{1}{c\left(\omega\right)} \approx \frac{1}{c_0} + \tan\left(\pi y/2\right)\alpha_0\omega^{y-1} + \frac{1}{2}\left(1 - \tan^2\left(\pi y/2\right)\right)\alpha_0^2 c_0 \omega^{2y-2} \tag{2.7}$$

and the approximate attenuation is the imaginary part of the wavenumber

$$\alpha\left(\omega\right) \approx \alpha_0\omega^y - \tan\left(\pi y/2\right)\alpha_0^2 c_0 \omega^{2y-1}. \tag{2.8}$$

When the power law exponent y is equal to 2, the Szabo wave equation reduces to the Blackstock equation

$$\nabla^2 p - \frac{1}{c_0^2}\frac{\partial^2 p}{\partial t^2} + \frac{2\alpha_0}{c_0}\frac{\partial^3 p}{\partial t^3} = 0, \tag{2.9}$$

where the 3D frequency-domain Green's function for the Blackstock equation is given by

$$G(r,\omega) = \frac{e^{-\frac{r}{c_0}\sqrt{-\omega^2 - 2\alpha_0 c_0 (j\omega)^3}}}{4\pi r}. \tag{2.10}$$

2.4 The power law wave equation

The power-law wave equation [39], which is closely related to the Szabo wave equation, is given by

$$\nabla^2 p - \frac{1}{c_0^2}\frac{\partial^2 p}{\partial t^2} - \frac{2\alpha_0}{c_0\cos\left(\pi y/2\right)}\frac{\partial^{y+1} p}{\partial t^{y+1}} - \frac{\alpha_0^2}{\cos^2\left(\pi y/2\right)}\frac{\partial^{2y} p}{\partial t^{2y}} = 0. \tag{2.11}$$

The first three terms in the power law wave equation also appear in the Szabo wave equation, where the fourth time-fractional term yields a complex wavenumber that exactly satisfies Eqs. 2.1 and 2.2 for all frequencies ω. The 3D frequency-domain Green's function for the power law wave equation is

$$G(r,\omega) = \frac{e^{-j\omega r/c_0} e^{-\alpha_0 (j\omega)^y r/\cos(\pi y/2)}}{4\pi r}. \tag{2.12}$$

By expanding the argument of the second exponential function in Eq. 2.12 after applying Euler's formula with $j^y = e^{j\pi y/2}$ and collecting real and imaginary terms, the attenuation and dispersion relations in Eqs. 2.1 and 2.2 are exactly recovered. Furthermore, unlike the other time-fractional wave equations evaluated here, the power law wave equation has an exact closed form 3D time-domain Green's function, which is

$$g\left(r,t\right) = \frac{1}{4\pi r}\frac{1}{\left(\alpha_0 r\right)^{1/y}}\tilde{f}_y\left[\frac{t-\frac{r}{c_0}}{\left(\alpha_0 r\right)^{1/y}}\right]. \tag{2.13}$$

In Eq. 2.13, $\tilde{f}_y$ is the probability density function (pdf) for a maximally skewed stable distribution [47] with parameter y. Since the power law wave equation exactly satisfies Eq. 2.1 and Eq. 2.2, demonstrating whether the time-domain Green's function in Eq. 2.13 is causal or noncausal is equivalent to demonstrating whether the combination of Eqs. 2.1 and 2.2 is causal or noncausal.

For the power law exponent $y = 2$, the 3D frequency-domain Green's function in Eq. 2.12 reduces to

$$G(r,\omega) = \frac{e^{-j\omega r/c_0}e^{-\alpha_0\omega^2 r}}{4\pi r}, \tag{2.14}$$

which is a Gaussian function multiplied by the $1/\left(4\pi r\right)$ geometric spreading factor and a complex exponential delay term. The inverse Fourier transform of Eq. 2.14 is exactly equal to the time-shifted Gaussian function

$$g\left(r,t\right) = \frac{1}{4\pi r}\frac{1}{\sqrt{4\pi\alpha_0 r}}e^{-(t-r/c_0)^2/(4\alpha_0 r)}, \tag{2.15}$$

which is equivalent to the time-domain Green's function in Eq. 2.13 with the power law exponent $y = 2$. Although the expressions in Eqs. 2.14 and 2.15 are only applicable to a few materials with frequency-squared attenuation such as water and air, these expressions are nevertheless convenient for preliminary evaluations and comparisons.

2.5 The Caputo wave equation

The Caputo wave equation [30], which is a time-fractional extension of the Stokes wave equation [48], is given by

$$\nabla^2 p - \frac{1}{c_0^2}\frac{\partial^2 p}{\partial t^2} + \tau^{y-1}\frac{\partial^{y-1}}{\partial t^{y-1}}\nabla^2 p = 0 \tag{2.16}$$

where τ is the fractional relaxation time. The Caputo wave equation approximately satisfies the attenuation and dispersion relations in Eqs. 2.1 and 2.2, respectively, and no exact closed form time-domain Green's function is available for the Caputo wave equation. However, there is an exact 3D frequency-domain Green's function for the Caputo wave equation, which is

$$G(r,\omega) = \frac{1}{1+(j\omega\tau)^{y-1}}\frac{e^{-\frac{j\omega r}{c_0}\frac{1}{\sqrt{1+(j\omega\tau)^{y-1}}}}}{4\pi r}. \tag{2.17}$$

for frequencies $\omega \geq 0$.

To obtain an expression that relates the value of the power law attenuation constant α_0 to the fractional relaxation time τ, the power law wave equation and the Caputo wave equation are Fourier-transformed in time and space. After solving for the square of the wavenumber and taking the square root of both sides, the smallness approximation [38] is applied to the expression obtained from the Caputo wave equation. The resulting conversion factor [41] is

$$\tau^{y-1} = -2\alpha_0 c_0 / \cos(\pi y/2). \tag{2.18}$$

The expression in Eq. 2.18 is singular at $y = 1$, the Szabo and power law wave equations are also singular at $y = 1$, and the Caputo wave equation is non-attenuating at $y = 1$, so only values of the power law exponent that satisfy $1 < y \leq 2$ are considered in the following numerical evaluations.

The phase velocity and attenuation are derived by solving the dispersion relation

$$k^2 = \frac{\omega^2}{c_0^2} + \frac{2\alpha_0 c_0}{\cos\left(\pi y/2\right)} \left(j\omega\right)^{y-1} k^2. \tag{2.19}$$

A second order approximation for the wavenumber is given by collecting terms that contain k^2 in Eq. 2.19 on the left side and then taking the square root, followed by the binomial approximation

$$\begin{aligned} k \approx \tfrac{\omega}{c_0} \left\{1 - j\alpha_0 c_0 \left[1 + j\tan\left(\pi y/2\right)\right] \omega^{y-1}\right\} \\ -\tfrac{3\alpha_0^2 c_0}{2} \left[1 + j2\tan\left(\pi y/2\right) - \tan^2\left(\pi y/2\right)\right] \omega^{2y-1}. \end{aligned} \tag{2.20}$$

The approximate phase velocity is then obtained from the real part of the wavenumber divided by ω,

$$\frac{1}{c\left(\omega\right)} \approx \frac{1}{c_0} + \tan\left(\pi y/2\right) \alpha_0 \omega^{y-1} - \frac{3}{2}\left(1 - \tan^2\left(\pi y/2\right)\right) \alpha_0^2 c_0 \omega^{2y-2} \tag{2.21}$$

and the approximate attenuation is the imaginary part of the wavenumber,

$$\alpha\left(\omega\right) \approx \alpha_0 \omega^y + 3\tan\left(\pi y/2\right) \alpha_0^2 c_0 \omega^{2y-1}. \tag{2.22}$$

2.6 Methods

Time-domain Green's functions for the power law wave equation are rapidly and accurately evaluated in Matlab with the STABLE toolbox [47, 49]. In these calculations, which numerically evaluate stable pdfs, the index parameter is defined as the power law exponent y, the skewness parameter is equal to 1, the scale parameter is equal to $\left(\alpha_0 r\right)^{1/y}$, and the location parameter is equal to zero. The STABLE toolbox evaluates stable pdfs at single points in time or limited ranges of time values without numerical artifacts, which is advantageous for calculations of time-domain Green's functions.

The time-domain Green's functions for the Blackstock, Stokes, Caputo, and Szabo wave equations are computed in Matlab with inverse fast Fourier transforms (IFFTs). For these calculations, a time window T is defined as an integer multiple of the scale factor $(\alpha_0 r)^{1/y}$ such that the numerical error is 1% or less. The time window T is then extended as needed to fill a larger display window for comparisons with other materials at the same distance. Other parameters that are required for these calculations include the frequency sampling, which is defined as $\Delta f = 1/T$, and the center of each time window, which is located at $t = r/c$. Each time-domain Green's function is computed with 100 time samples per scale parameter, which consistently yields smooth time-domain waveforms for each result. If the time window defined for the time-domain Green's function calculation is larger than the desired display window, then the computed waveform is cropped after the IFFT is evaluated.

In calculations of time-domain Green's functions for the Blackstock and Stokes wave equations with the IFFT, the time window is defined as $T \gg (\alpha_0 r)^{1/y}$, and even larger time windows are needed for IFFT-based calculations of the time-domain Green's functions for the Caputo and Szabo wave equations to avoid problems with frequency-domain aliasing. Similar to the time-domain Green's functions for the power law wave equation, the time-domain Green's functions for the Caputo and Szabo wave equations have 'heavy tails' that decay as $1/t^{y+1}$ when $0 < y < 2$. These 'heavy tails' cause undesirable wrap-around artifacts in the time-domain unless the time window T is sufficiently large and the frequency sampling $\Delta f = 1/T$ is sufficiently small. Also, for IFFT calculations with nonzero start time t_0, the frequency-domain Green's function is multiplied by $e^{j\omega t_0}$. This accounts for start times before $t = 0$ when noncausal results are shown close to the source and also for calculations at larger distances with later start times.

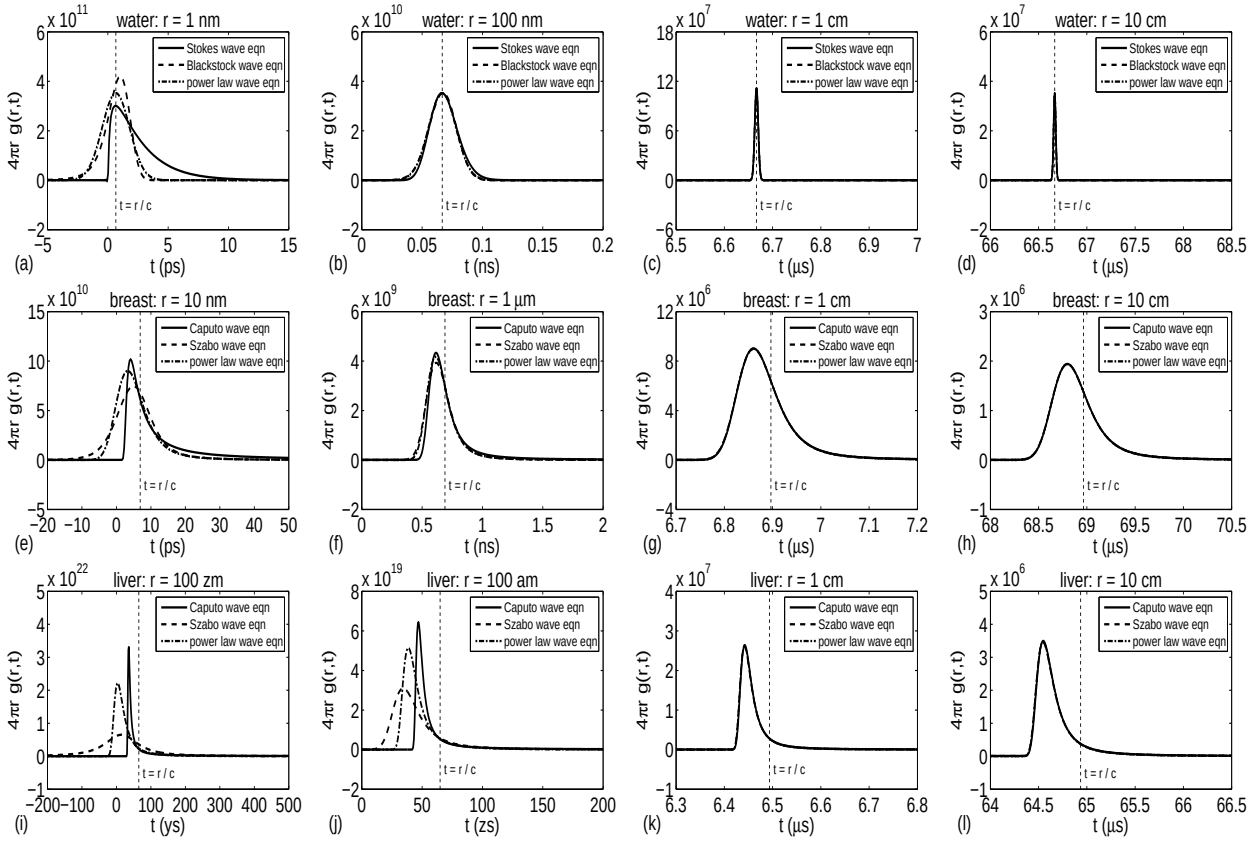

Figure 2.1: (a-d) Simulated time-domain Green's functions of the Caputo, Szabo, and power law wave equations calculated for water with $y = 2$, $\alpha_0 = 2.5328 \times 10^{-4}$ Np/cm/MHz^2, and $c_0 = 1500$ m/s and scaled by $4\pi r$ at (a) $r = 1$ nm, (b) $r = 100$ nm, (c) $r = 1$ cm, and (d) $r = 10$ cm. (e-h) Simulated time-domain Green's functions of the Caputo, Szabo, and power law wave equations calculated for breast with $y = 1.5$, $\alpha_0 = 0.086$ Np/cm/MHz$^{1.5}$, and $c_0 = 1450$ m/s and scaled by $4\pi r$ at (e) $r = 10$ nm, (f) $r = 1\,\mu$m, (g) $r = 1$ cm, and (h) $r = 10$ cm. (i-l) Simulated time-domain Green's functions of the Caputo, Szabo, and power law wave equations calculated for liver with $y = 1.139$, $\alpha_0 = 0.0459$ Np/cm/MHz$^{1.139}$, and $c_0 = 1540$ m/s and scaled by $4\pi r$ at (i) $r = 100$ zm, (j) $r = 100$ am, (k) $r = 1$ cm, and (l) $r = 10$ cm.

2.7 Results

2.7.1 Time-domain Green's functions for acoustic propagation in water

Time-domain Green's functions multiplied by $4\pi r$ are shown in Figs. 2.1(a-d) for acoustic propagation in water with $y = 2$. The results in these figures are calculated with $c_0 = 1500\text{m/s}$ and $\alpha_0 = 2.5328 \times 10^{-4}$ Np/cm/MHz^2. In Figs. 2.1(a-d), the time-domain Green's function for the Stokes wave equation is indicated by a solid line, the time-domain Green's function for the Blackstock wave equation (Eq. 2.9) is represented by a dashed line, and the time-domain Green's function for the power law wave equation is indicated by a dash-dot line. The time-domain Green's function for the power law wave equation is directly calculated from the Gaussian function in Eq. 2.15, and the time-domain Green's functions for the Blackstock and Stokes wave equations apply IFFTs to the values obtained from the frequency-domain Green's functions in Eqs. 2.4 and 2.17, respectively, with the power law exponent $y = 2$. A thin dashed line is also included as a reference in each of the subfigures in Fig. 2.1 to indicate the arrival time $t = r/c_0$ for a lossless medium with a constant sound speed c_0.

The time-domain Green's functions for the Stokes, Blackstock, and power law wave equations evaluated in water are shown in Figs. 2.1(a-d) at distances of $r = 1$ nm, $r = 100$ nm, $r = 1$ cm, and $r = 10$ cm. The computed Green's functions are multiplied by $4\pi r$ so that the spherical spreading contribution is eliminated and only the effects of propagation, dispersion, and attenuation as a function of time are included in these plots. The units defined for the horizontal axis are picoseconds, nanoseconds, or microseconds. Fig. 2.1(a) shows the result evaluated at a distance $r = 10^{-n}$ m for the smallest integer value of n, specifically $n = 9$, that clearly demonstrates noncausal behavior in the time-domain Green's functions for both the Blackstock and power law wave equations. Fig. 2.1(b) shows the result at a distance $r = 10^{-n}$ m for the largest integer value of n, namely $n = 7$, where the noncausal behavior

is not clearly evident in plots of the time-domain Green's functions for the Blackstock and power law wave equations when displayed on a linear vertical scale. Figs. 2.1(c-d) show the results at $r = 1$ cm and $r = 10$ cm, respectively, which are representative distances for applications of diagnostic and therapeutic ultrasound. The time-domain Green's functions for the Blackstock and Stokes wave equations define time windows T for IFFT calculations as 40, 40, 300, and 500 times the scale factor $(\alpha_0 r)^{1/y}$ calculated for each respective plot in Figs. 2.1(a-d). The results in Figs. 2.1(a-d) are then cropped and displayed in time windows that are approximately 25, 25, 197, and 312 scale factors wide, respectively. Figs. 2.1(a-d) demonstrate that the time-domain Green's functions for the Blackstock and power law wave equations produce noncausal time-domain waveforms very close to the source and that these transition over a short distance to waveforms that are difficult to distinguish from causal waveforms in the time-domain.

Fig. 2.1(a) indicates that the time-domain Green's functions for the Blackstock and power law wave equations with $y = 2$ evaluated at $r = 1$ nm yield similar, yet distinct, results, where both of these are clearly noncausal with significant nonzero contributions between $t = -5$ ps and $t = 0$. Whereas the time-domain Green's function for the power law wave equation is a Gaussian function in time, the time-domain Green's function for the Blackstock wave equation is slightly skewed to the right in this location. The time-domain Green's function for the Stokes wave equation evaluated at $r = 1$ nm first demonstrates nonzero values after time $t = 0$, and the shape of the time-domain Green's function for the Stokes wave equation is clearly different from the other two time-domain Green's functions.

The time-domain Green's functions evaluated at $r = 100\,\text{nm}$ in Fig. 2.1(b) have nearly converged to the same result. All three waveforms are now clearly offset from $t = 0$, where some small differences remain, and all three waveforms appear to be causal in these plots. However, since the time-domain Green's function for the power law wave equation is a time-shifted Gaussian function, even though the result appears to be causal, the time-domain result is nonzero for all values of $t < 0$, so the Green's function for the power law wave

equation is noncausal. In Figs. 2.1(c-d), all three time-domain Green's functions evaluated at $r = 1\,\text{cm}$ and at $r = 10\,\text{cm}$ agree closely, which indicates that as the distance r increases, the time-domain Green's functions for the Blackstock and Stokes wave equations converge to the Gaussian function in Eq. 2.15.

2.7.2 Time-domain Green's functions for acoustic propagation in breast

Figs. 2.1(e-h) describe the time-domain Green's functions multiplied by $4\pi r$ for the Caputo wave equation (solid line), the Szabo wave equation (dashed line), and the power law wave equation (dot-dashed line) calculated for human breast with $y = 1.5$, $c_0 = 1450$ m/s, and $\alpha_0 = 0.086$ Np/cm/MHz$^{1.5}$. The results are computed at $r = 10\,\text{nm}$, $r = 1\,\mu\text{m}$, $r = 1\,\text{cm}$, and $r = 10$ cm. The units defined for the horizontal axis in Figs. 2.1(e-h) are again picoseconds, nanoseconds, or microseconds. Fig. 2.1(e) contains the result evaluated at a distance $r = 10^{-n}$ m for the smallest integer value of n, specifically $n = 8$, that clearly demonstrates noncausal behavior in the time-domain Green's functions for both the Szabo and power law wave equations. Fig. 2.1(f) displays the result at a distance $r = 10^{-n}$ m for the largest integer value of n, namely $n = 6$, where the noncausal behavior is not clearly evident in plots of the time-domain Green's functions for both the Szabo and power law wave equations when displayed on a linear vertical scale. Figs. 2.1(g-h) describe the results at $r = 1$ cm and $r = 10$ cm. The time-domain Green's functions for the Szabo and Caputo wave equations define the time windows T for IFFT calculations as 300, 60, 30, and 30 times the scale factor $(\alpha_0 r)^{1/y}$ calculated at each distance r for each respective plot in Figs. 2.1(e-h). The results in Figs. 2.1(e-h) are then cropped and displayed in time windows that are approximately 23, 30, 16, and 17 scale factors wide, respectively.

Fig. 2.1(e), which shows the time-domain Green's functions calculated for breast at $r =$ 10 nm, indicates that the Szabo and power law wave equations are noncausal and that the Caputo wave equation is causal. In this location, the time-domain Green's functions

for the Szabo and power law wave equations are clearly nonzero before time $t = 0$, and the time-domain Green's function for the Caputo wave equation first demonstrates nonzero values after time $t = 0$. The shapes of the three time-domain waveforms also demonstrate significant differences at this distance.

Fig. 2.1(f), which is evaluated at $r = 1\,\mu$m, shows that the three waveforms calculated for breast are starting to converge at this distance. However, at $r = 1\,\mu$m, identifying noncausal contributions, if present, is difficult in the time-domain when the Green's functions are plotted on a linear scale. Similar to the Gaussian function, the stable pdf in the numerator of Eq. 2.13 is strictly positive [39] for all values of t when $y = 1.5$, so the power law wave equation is noncausal at all distances for $y = 1.5$.

Figs. 2.1(g-h), which are evaluated at $r = 1$ cm and $r = 10$ cm, respectively, show that the time-domain Green's functions for the three time-fractional wave equations in Eqs. 2.3, 2.11, and 2.16 converge to the same result at these distances. Unlike the results shown in Figs. 2.1(b-d), which are either approximately or exactly represented by symmetric, time-shifted Gaussian functions, the time-domain Green's functions in Figs. 2.1(f-h) are skewed (asymmetric) with a 'heavy tail,' which are characteristics of the maximally-skewed stable probability distribution (pdf) in Eq. 2.13.

2.7.3 Time-domain Green's functions for acoustic propagation in liver

Figs. 2.1(i-l) show the simulated Green's functions for the Caputo wave equation (solid line), the Szabo wave equation (dashed line), and the power law wave equation (dot-dashed line) for human liver with $y = 1.139$, $\alpha_0 = 0.0459$ Np/cm/MHz$^{1.139}$, and $c_0 = 1540$ m/s. In Figs. 2.1(i-l), the three time-domain Green's functions are multiplied by $4\pi r$ and then evaluated at $r = 100$ zm, $r = 100$ am, $r = 1$ cm, and $r = 10$ cm. The units defined for the horizontal axis in Figs. 2.1(i-l) are yoctoseconds (ys or 10^{-24} seconds), zeptoseconds (zs or 10^{-21} seconds), or microseconds (μs). Fig. 2.1(i) contains the result evaluated at a distance

$r = 10^{-n}$ m for the smallest integer value of n, specifically $n = 19$, that clearly demonstrates noncausal behavior in the time-domain Green's functions for both the Szabo and power law wave equations, and Fig. 2.1(j) displays the result at a distance $r = 10^{-n}$ m for the largest integer value of n, namely $n = 16$, where the noncausal behavior is not clearly evident in any of the three time-domain Green's functions when shown on a linear scale. Figs. 2.1(k-l) show the results at $r = 1$ cm and $r = 10$ cm, respectively. The time-domain Green's functions for the Szabo and Caputo wave equations define time windows T for IFFT calculations as 12000, 4000, 60, and 40 times the scale factor $(\alpha_0 r)^{1/y}$ calculated at each distance r for each respective plot in Figs. 2.1(i-l). The results in Figs. 2.1(i-l) are then cropped and displayed in windows that are approximately 55, 37, 47, and 31 scale factors wide, respectively.

Fig. 2.1(i) depicts the time-domain Green's functions calculated for human liver at $r =$ 100 zm (where 1 zeptometer = 1 zm = 10^{-21} m). In Fig. 2.1(i), the time-domain Green's functions for the Szabo and power law wave equations are clearly noncausal, and the time-domain Green's function for the Caputo wave equation begins a short time after $t = 0$. In Fig. 2.1(j), which is evaluated at $r = 100$ am, the time-domain Green's functions of all three wave equations are still distinct, and all three appear to start after $t = 0$.

Figs. 2.1(k-l) display the time-domain Green's function calculated for human liver at $r = 1$ cm and at $r = 10$ cm, respectively. These figures indicate that the three time-domain Green's functions again converge to the same result as the distance increases. The waveforms in Figs. 2.1(k-l) are clearly distinct from the waveforms shown in Figs. 2.1(g-h) in terms of both the overall shape and the temporal extent. Also, the power law wave equation maintains the same shape for the time-domain Green's function at all distances, but the shapes of the time-domain Green's functions for the Szabo and Caputo wave equations are noticeably different at shorter distances.

2.7.4 Vertical axis scaling

In each subfigure of Fig. 2.1, the maximum value of the vertical axis is determined by the largest of the three peak values in that subfigure. The peak value of $4\pi r g(r,t)$ for the power

law wave equation when $y = 2$ is equal to $1/\sqrt{4\pi\alpha_0 r}$. Similarly, the peak value of the scaled stable pdf in Eq. 2.13 is approximately equal to $1/\left[2\sqrt{\pi}(\alpha_0 r)^{1/y}\right]$. Thus, when the peaks of the three time-domain Green's functions start to converge, each decays as $r^{-1/y}$. The limits of the vertical axes are proportional to the peak of the scaled stable pdf, and before the peak values converge, the axes are autoscaled.

2.7.5 Comparisons between time-domain Green's functions for acoustic propagation

To enable comparisons between the time-domain Green's functions calculated in water, breast, and liver, Figs. 2.1(c), 2.1(g), and 2.1(k), which occupy the third column of Fig. 2.1, are all calculated at $r = 1$ cm, and Figs. 2.1(d), 2.1(h), and 2.1(l), which occupy the fourth column of Fig. 2.1, are all calculated at $r = 10$ cm. Figs. 2.1(a), 2.1(b), 2.1(e), 2.1(f), 2.1(i), and 2.1(j) are all computed at different distances, so the figures in the first two columns of Fig. 2.1 are not compared. Figs. 2.1(c), 2.1(g), and 2.1(k) are all shown in a $0.5\,\mu$s wide time window, and Figs. 2.1(d), 2.1(h), and 2.1(l) are all shown in a $2.5\,\mu$s wide time window, where the size of each time window is determined by the temporal extent of the time-domain Green's functions calculated for ultrasound parameters in breast.

When displayed in these two time windows, the time-domain Green's function for acoustic propagation in water exhibits nearly negligible dispersion, the time-domain Green's function for acoustic propagation in liver shows moderate dispersion, and the time-domain Green's function for acoustic propagation in breast is much more dispersive than water or liver. Furthermore, the time-domain Green's function for acoustic propagation in water is nearly impulsive relative to breast and liver. Also, each figure in Fig. 2.1 exhibits different arrival times. This is in part due to the different values for c_0 in water, breast, and liver, where the thin dashed lines that indicate the arrival time for a lossless medium with sound speed c_0 each occur at a different time, as observed along the third and the fourth columns of Fig. 2.1. The time-domain Green's functions for acoustic propagation in breast and liver also demonstrate

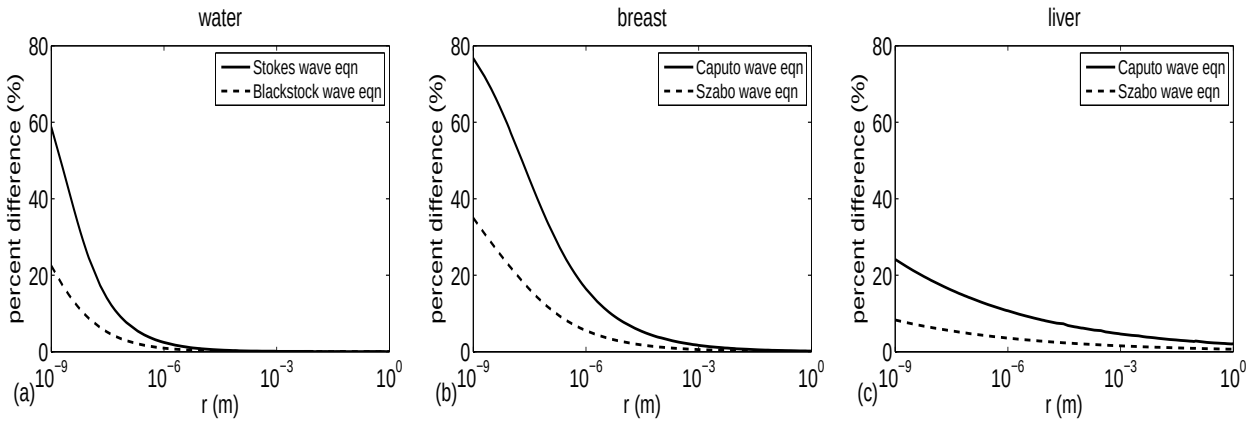

Figure 2.2: a) The percent difference between the time-domain Green's functions for the Blackstock and Stokes wave equations and the time-domain Green's function for the power law wave equation as a function of distance calculated for water with $y = 2$, $\alpha_0 = 2.5328 \times 10^{-4}$ Np/cm/MHz^2, with $c_0 = 1500$m/s. b-c) The percent difference between the time-domain Green's functions for the Szabo and Caputo wave equation and the time-domain Green's functions for the power law wave equation as a function of distance calculated for breast with $y = 1.5$, $\alpha_0 = 0.086$ Np/cm/MHz$^{1.5}$, and $c_0 = 1450$ m/s and calculated for liver with $y = 1.139$, $\alpha_0 = 0.0459$ Np/cm/MHz$^{1.139}$, and $c_0 = 1540$ m/s.

much earlier arrival times than the time $t = r/c_0$ predicted for lossless propagation, where the earlier arrival times in the lossy models are due to dispersion. Furthermore, the peak value of the time-domain Green's function for acoustic propagation is largest in water and smallest in breast, as indicated by comparisons between the values on the vertical axes (noting the exponents in the upper left hand corner of each subfigure) in Figs. 2.1(c), 2.1(g), and 2.1(k) ($r = 1$ cm) and Figs. 2.1(d), 2.1(h), and 2.1(l) ($r = 10$ cm). Comparisons along the third and fourth columns of Fig. 2.1 also show that the shapes and extents of the time-domain Green's functions for acoustic propagation in water, breast, and liver differ significantly, as determined by the values of the power law exponent y and the scale factor $(\alpha_0 r)^{1/y}$.

2.7.6 Convergence of the Green's functions for acoustic propagation in the time domain

Figs. 2.1(a-d) demonstrate that the time-domain Green's functions for the Blackstock and Stokes wave equations multiplied by $4\pi r$ converge to a Gaussian function, and Figs. 2.1(e-h) and 2.1(i-l) show that the time-domain Green's functions for the Szabo and Caputo wave

equations multiplied by $4\pi r$ converge to maximally skewed stable pdfs. This suggests that the time-domain Green's function for the power law wave equation is an effective approximation for the time-domain Green's functions of the Blackstock and Stokes wave equations when $y = 2$ and the Szabo and Caputo wave equations when $1 < y < 2$. To characterize the convergence of these time-domain Green's functions, the percent difference between $g(r,t)$ and a reference $g_{ref}(r,t)$ is defined as $||g(r,t) - g_{ref}(r,t)||_2 \,/\, ||g_{ref}(r,t)||_2 \times 100\%$, where $g(r,t)$ is the time-domain Green's function calculated at a given distance r for the Blackstock, Stokes, Szabo, or Caputo wave equation, and the reference time-domain Green's function $g_{ref}(r,t)$ for these calculations is the time-domain Green's function for the power law wave equation. In Fig. 2.2, these percent differences are calculated from $r = 1$ nm to $r = 1$ m for each material. Fig. 2.2(a) shows the convergence of the time-domain Green's functions for the Stokes and Blackstock wave equations to the time-domain Green's function of the power law wave equation calculated for water with $y = 2$, $\alpha_0 = 2.5328 \times 10^{-4}$ Np/cm/MHz^2, and $c_0 = 1500$m/s. Fig. 2.2(b) shows the convergence of the time-domain Green's functions for the Szabo and Caputo wave equations to the time-domain Green's function of the power law wave equation calculated for breast with $y = 1.5$, $\alpha_0 = 0.086$ Np/cm/MHz$^{1.5}$, and $c_0 = 1450$ m/s. Fig. 2.2(c) shows the convergence of the time-domain Green's functions for the Szabo and Caputo wave equations to the time-domain Green's function of the power law wave equation calculated for liver with the power law exponent $y = 1.139$, $\alpha_0 = 0.0459$ Np/cm/MHz$^{1.139}$, and $c_0 = 1540$ m/s.

In each medium, the percent differences calculated with the time-domain Green's functions for the Blackstock and Szabo wave equations are consistently smaller than those calculated for the Stokes and Caputo wave equations, respectively. In Fig. 2.2(a), the percent difference for the time-domain Green's function of the Blackstock wave equation calculated for water is 23% at $r = 1$ nm, and the percent difference for the time-domain Green's function of the Stokes wave equation calculated for water is 59% at $r = 1$ nm. Both time-domain Green's functions achieve rapid reductions in the percent difference calculated

for water between 1 nm and 1 μm. The percent difference for the time-domain Green's function of the Blackstock wave equation calculated for water reaches 0.0009% at $r = 1$ m, and the percent difference for the time-domain Green's function of the Stokes wave equation calculated for water reaches 0.0024% at $r = 1$ m. In Fig. 2.2(b), the percent difference for the time-domain Green's function of the Szabo wave equation calculated for breast is 35% at $r = 1$ nm, and the percent difference for the time-domain Green's function of the Caputo wave equation calculated for breast is 77% at $r = 1$ nm. The time-domain Green's functions calculated for breast converge more slowly than those calculated for water, where the percent difference for the time-domain Green's function of the Szabo wave equation calculated for breast reaches 0.055% at $r = 1$ m, and the percent difference for the time-domain Green's function of the Caputo wave equation calculated for breast reaches 0.17% at $r = 1$ m. In Fig. 2.2(c), the percent difference for the time-domain Green's function of the Szabo wave equation calculated for liver is 8% at $r = 1$ nm, and the percent difference for the time-domain Green's function of the Caputo wave equation calculated for liver is 24% at $r = 1$ nm. Although the percent differences evaluated at $r = 1$ nm are smaller in liver than in water, the rate of convergence of these time-domain Green's functions is slower in liver than in water or breast, where the percent difference for the time-domain Green's function of the Szabo wave equation calculated for liver reaches 0.66% at $r = 1$ m, and the percent difference for the time-domain Green's function of the Caputo wave equation calculated for breast reaches 2% at $r = 1$ m.

2.7.7 Characterizing the noncausal component of the time-domain Green's functions for the Blackstock, Szabo, and power law wave equations

In numerical calculations with the Blackstock, Szabo, and power law wave equations, there is a threshold distance above which the noncausal time-domain Green's function is very small for all times $t \leq 0$. The distance beyond which the noncausal component of

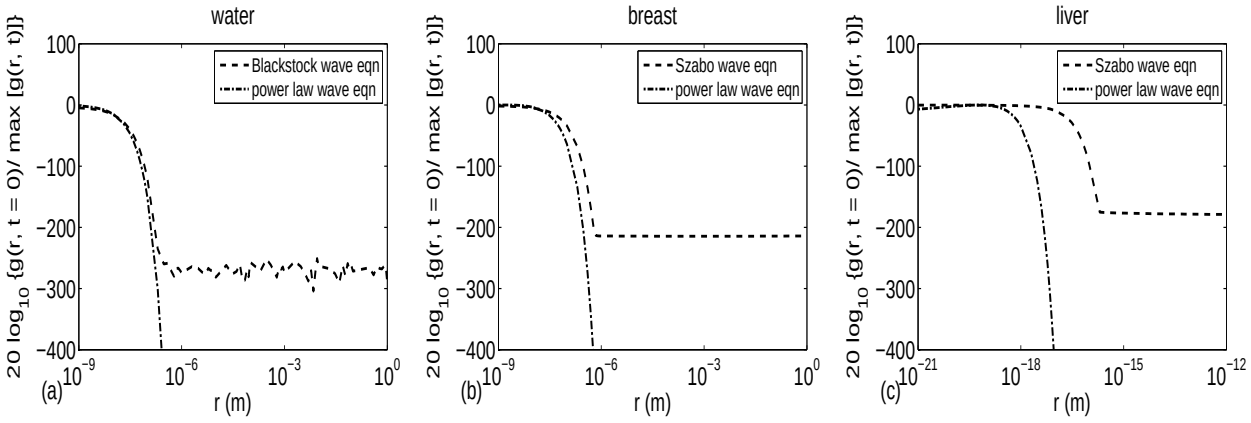

Figure 2.3: Relative noncausal contributions of the Blackstock, Szabo, and power law wave equations characterized with $20\log_{10}\{g(r,t=0)/\max[g(r,t)]\}$ as a function of distance r. This quantity is calculated for a) water with $y = 1.139$, $\alpha_0 = 0.0459$ Np/cm/MHz$^{1.139}$, and $c_0 = 1540$ m/s from $r = 1$ nm to $r = 1$ m, b) breast with $y = 1.5$, $\alpha_0 = 0.086$ Np/cm/MHz$^{1.5}$, and $c_0 = 1450$ m/s from $r = 1$ nm to $r = 1$ m, and c) liver with $y = 1.139$, $\alpha_0 = 0.0459$ Np/cm/MHz$^{1.139}$, and $c_0 = 1540$ m/s from $r = 1$ zm to $r = 1$ pm.

the time-domain Green's functions for the Blackstock, Szabo, and power law wave equation becomes negligible is characterized here with an approach similar to that in [38] by computing the quantity $20\log_{10}\{g(r,t=0)/\max[g(r,t)]\}$, which calculates the value of $g(r,t)$ evaluated at time $t = 0$ divided by the maximum value of $g(r,t)$ in dB, where the time-domain Green's functions in the numerator and the denominator are each calculated with a fixed value of r, and the maximum value of $g(r,t)$ is evaluated with respect to the time t. In Fig. 2.3, this expression is evaluated across nine decades at 10 equally spaced samples within each decade. The time-domain Green's functions for the Stokes and Caputo wave equations are not characterized with this approach because both of these are always causal for the y values considered here (i.e., 2, 1.5, and 1.139).

The results of this calculation are shown in Figs. 2.3(a-c) for water, breast, and liver. Figs. 2.3(a) and 2.3(b) show that $20\log_{10}\{g(r,t=0)/\max[g(r,t)]\}$ evaluated for water and for breast with the time-domain Green's function of the power law wave equation rapidly drops from approximately 0 dB to -400 dB between $r = 1$ nm and $1\,\mu$m. Fig. 2.3(c) shows that $20\log_{10}\{g(r,t=0)/\max[g(r,t)]\}$ calculated for liver with the time-domain Green's function of the power law wave equation rapidly decays from approximately 0 dB to -400 dB

between $r = 10$ am and $100\,f$m. Fig. 2.3(a) shows that $20\log_{10}\{g(r,t=0)/\max[g(r,t)]\}$ calculated for water with the time-domain Green's function of the Blackstock wave equation closely tracks the same curve for the time-domain Green's function of the power law wave equation until a threshold between -200 and -300 dB is reached. Fig. 2.3(b) shows that $20\log_{10}\{g(r,t=0)/\max[g(r,t)]\}$ calculated for breast with the time-domain Green's function of the Szabo wave equation follows the same trend as the corresponding curve for the time-domain Green's function of the power law wave equation until a threshold near -200 dB is reached. Also, there is a greater difference between the two curves in Fig. 2.3(b) than in Fig. 2.3(a). Fig. 2.3(c) shows that, for calculations with the time-domain Green's function of the Szabo wave equation evaluated for liver, the value of $20\log_{10}\{g(r,t=0)/\max[g(r,t)]\}$ rapidly decays from approximately 0 dB to a value between -100 and -200 dB between $r = 1$ am and $1\,f$m. There is a much larger difference between the values of $20\log_{10}\{g(r,t=0)/\max[g(r,t)]\}$ calculated for liver with the Szabo and power law wave equations than for water or breast. In each calculation of $20\log_{10}\{g(r,t=0)/\max[g(r,t)]\}$ that evaluates $g(r,t)$ for the Blackstock and Szabo wave equations, the lower threshold is a limitation of numerical calculations with the IFFT, whereas the STABLE toolbox avoids these problems with a numerical approach that is optimized for calculations of stable pdfs [47].

2.7.8 Time-domain Green's functions convolved with a three cycle Hanning-weighted pulse

To demonstrate the effects of power law attenuation and dispersion on transient excitations, three cycle Hanning-weighted pulses [50, 51] are convolved with time-domain Green's functions multiplied by $4\pi r$, and the results are shown in Fig. 2.4. In each medium, the convolved waveforms are evaluated at (a) $r = 100\,\mu$m, (b) $r = 1$ mm, (c) $r = 1$ cm, and (d) $r = 10$ cm. In Fig. 2.4, the center frequency of the Hanning-weighted pulse is $f_0 = 7.5$ MHz,

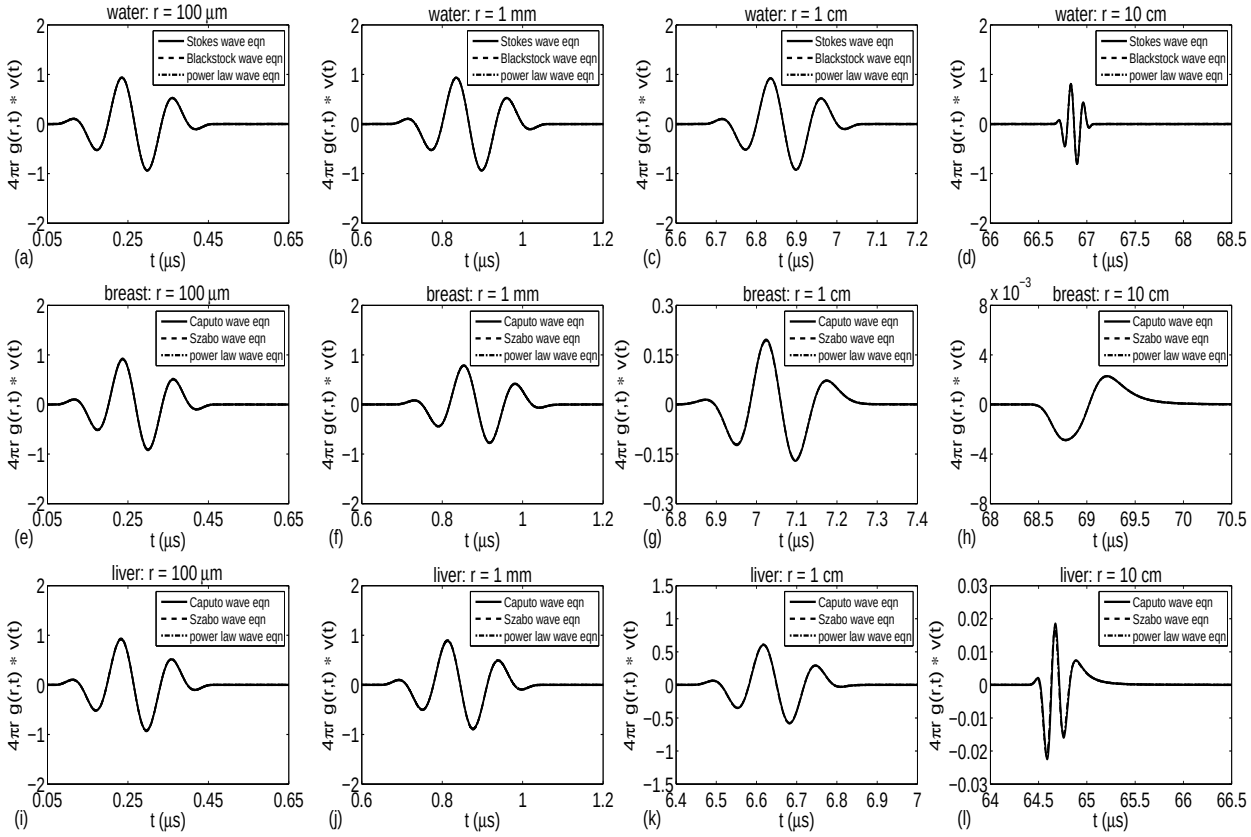

Figure 2.4: Simulated three-cycle Hanning-weighted pulse with a center frequency of $f_0 = 7.5$ MHz convolved with time-domain Green's functions multiplied by $4\pi r$ calculated for water at (a) $r = 100\,\mu$m, (b) $r = 1$ mm, (c) $r = 1$ cm, and (d) $r = 10$ cm, calculated for breast at (e) $r = 100\,\mu$m, (f) $r = 1$ mm, (g) $r = 1$ cm, and (h) $r = 10$ cm, and calculated for liver at (i) r= $100\,\mu$m, (j) $r = 1$ mm, (k) $r = 1$ cm, and (l) $r = 10$ cm.

which is a representative frequency for medical ultrasound that highlights some of the differences between the waveforms computed for these three materials.

In Figs. 2.4(a-d), which show the convolved waveforms for water, there is no attenuation or dispersion of the pulse at all four distances, and the results obtained from the Stokes, Blackstock, and power law wave equations are nearly identical. The only differences in Figs. 2.4(a-d) are due to the differences in propagation delays and the different time scale that is employed in Fig. 2.4(d) to facilitate comparisons with Figs. 2.4(h) and 2.4(l). Figs. 2.4(a-d) demonstrate that, at these distances, the time-domain Green's functions for the Blackstock, Stokes, and power law wave equation are effectively delta functions for a three cycle Hanning-weighted pulse with a 7.5 MHz center frequency and that dispersion in water is only observed over much longer distances in water for this short pulse.

Figs. 2.4(e-h) describe the time-domain Green's functions for acoustic propagation in breast convolved with a three-cycle Hanning-weighted pulse with center frequency $f_0 =$ 7.5 MHz evaluated at the same four distances. At $r = 100\,\mu$m, $r = 1$ mm, and at shorter distances, the causal and noncausal time-domain Green's functions evaluated at these distances are all effectively equivalent to delta functions in these convolutions, so at $r = 100\,\mu$m, $r = 1$ mm, and at shorter distances, there is minimal attenuation and dispersion of this short pulse. In Fig. 2.4(g), there is a slight difference between the three waveforms at $r = 1$ cm, and some attenuation and dispersion is also observed in Fig. 2.4(g) at $r = 1$ cm. Fig. 2.4(h) indicates that the three convolution results are approximately the same and that the attenuation and dispersion are significant for breast at $r = 10$ cm. The signal amplitude drops off considerably in Fig. 2.4(h), and there is also considerable filtering and spreading of the signal in the time domain in Fig. 2.4(h) relative to Figs. 2.1(e-g). Fig. 2.4(h) also shows that, unlike the result shown in water at $r = 10$ cm in Fig. 2.4(d), the 7.5 MHz center frequency has been completely removed by the effects of power law attenuation and dispersion at the distance $r = 10$ cm.

Figs. 2.4(i-l) show the results obtained when the time-domain Green's functions for acoustic propagation in liver are convolved with a three-cycle Hanning-weighted pulse with a $f_0 = 7.5$ MHz center frequency. Figs. 2.4(i) and 2.4(j) demonstrate that the three convolution results are nearly equivalent and that there is minimal attenuation or dispersion at $r = 100\,\mu$m and at $r = 1$ mm. Fig. 2.4(k) indicates that there is a small difference between the three waveforms at $r = 1$ cm, and there is minimal attenuation and dispersion observed in Fig. 2.4(k) relative to Figs. 2.4(i-j). In Fig. 2.4(l), which is evaluated at $r = 10$ cm, some differences are observed in the three convolution results because of the differences that are observed at this distance in Fig. 2.2(c), and there is a moderate amount of attenuation and dispersion relative to that observed at shorter distances in Figs. 2.4(i-k).

Some interesting trends are also observed when the waveforms evaluated at the same distance are compared for different media. For example, the waveforms in Figs. 2.4(a), 2.4(e), and 2.4(i), which are calculated at $r = 100\,\mu$m, are all displayed within the same time window. These three figures are all very similar, and no attenuation or dispersion is evident in any of these. The waveforms in Figs. 2.4(b), 2.4(f), and 2.4(j), which are calcuated at $r = 1$ mm, are also evaluated in the same time window. These three figures are also very similar, again with no attenuation or dispersion, although the waveform locations vary due to the differences in the sound speeds c_0 for the three media. The waveforms in Figs. 2.4(c), 2.4(g), and 2.4(k), which are evaluated at $r = 1$ cm, are all shown in $0.6\,\mu$s wide time windows with different start times. These figures demonstrate more obvious shifts in the waveform locations due to sound speed differences, show some variation in the attenuation in the three media, and indicate the onset of dispersion in the signal calculated for breast. The convolution results in Figs. 2.4(d), 2.4(h), and 2.4(l), which are evaluated at $r = 10$ cm, are all shown in $2.5\,\mu$s wide time windows with different start times. At $r = 10$ cm, the waveform calculated for water still shows no evidence of attenuation and dispersion, the waveform calculated for liver demonstrates some attenuation and dispersion,

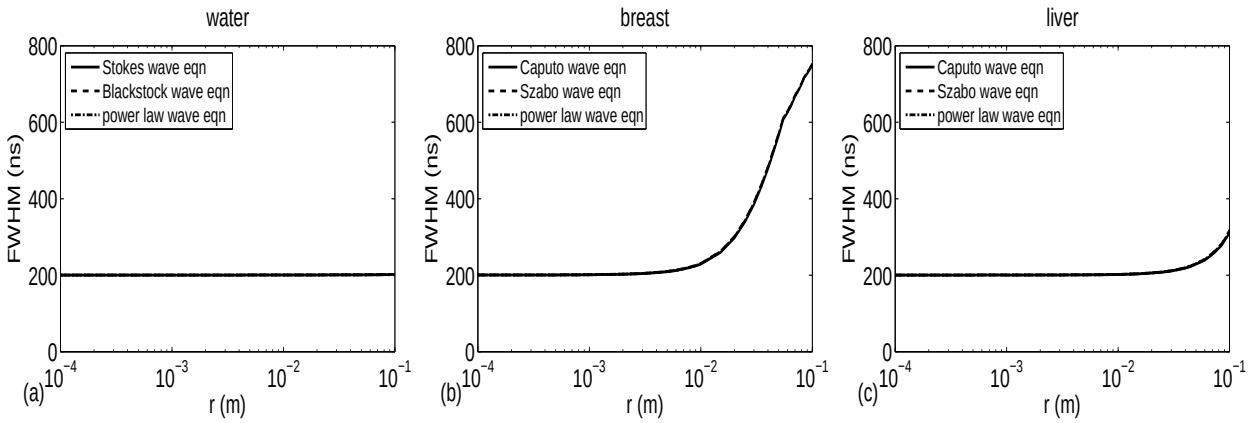

Figure 2.5: The FWHM of the envelope of $v(t) * 4\pi r g(r,t)$ calculated for a) water, b) breast, and c) liver, where $v(t)$ is a three cycle Hanning-weighted pulse and $g(r,t)$ is the time-domain Green's function for the Stokes, Blackstock, Caputo, Szabo, or power law wave equation.

and the waveform calculated for breast demonstrates the most attenuation and dispersion of these three materials.

2.7.9 Characterizing the dispersion of $\mathbf{v(t) * 4\pi rg(r,t)}$ with the full width at half maximum (FWHM) of the envelope

Fig. 2.5 characterizes the dispersion by evaluating the full width at half maximum (FWHM) of the envelope of the convolution $v(t) * 4\pi r g(r,t)$ for each time-domain Green's function. The FWHM are shown in Figs. 2.5(a-c) for water, breast, and liver, respectively, where the results are evaluated for distances r between 100 μm and 10 cm. The FWHM in Fig. 2.5 is calculated by evaluating the Hilbert transform of $v(t) * 4\pi g(r,t)$ and taking the absolute value of the result to obtain the envelope of the waveform. Then, the time at which the peak value of the envelope occurs is determined, the times at which the half peak value is reached are extracted, and then the difference between the largest and the smallest times at which the half peak value occurs determines the FWHM.

In Figs. 2.5(a-c), the FWHM is calculated for the envelope of $v(t) * 4\pi r g(r,t)$, where $v(t)$ is a 3 cycle Hanning-weighted pulse with a center frequency of 7.5 MHz, and $g(r,t)$ represents the time-domain Green's function for the Stokes, Blackstock, Caputo, Szabo, or power law wave equation. In Fig. 2.5(a), the FWHM values calculated with the time-domain Green's

functions of the Stokes, Blackstock, and power law wave equations for water are all equal to 200.42 ns at $r = 100\,\mu$m and are all equal to 201.76 ns at $r = 10$ cm. The FWHM of the 3 cycle Hanning-weighted pulse with a center frequency of 7.5 MHz is equal to 200 ns, which suggests that the dispersion is negligible in water for a pulse with 7.5 MHz center frequency for all distances r between $100\,\mu$m and 10 cm. In Fig. 2.5(b), the FWHM values calculated with the time-domain Green's functions of the Caputo, Szabo, and power law wave equations for breast are equal to 200.49 ns, 200.5 ns, and 200.5 ns, respectively, at $r = 100\,\mu$m and are equal to 750.81 ns, 753.56 ns, and 752.82 ns, respectively, at $r = 10$ cm. Thus, for all three convolution calculations in breast, the dispersion is negligible at $r = 100\,\mu$m, but there is significant dispersion at $r = 10$ cm. In Fig. 2.5(c), the FWHM values calculated with the time-domain Green's functions of the Caputo, Szabo, and power law wave equations for liver are equal to 200.46 ns, 200.44 ns, and 200.44 ns, respectively, at $r = 100\,\mu$m and are equal to 311.28 ns, 318.23 ns, and 316.41 ns, respectively, at $r = 10$ cm. Thus, for all three convolution calculations in liver, the dispersion is negligible at $r = 100\,\mu$m, and there is moderate dispersion at $r = 10$ cm. Also, as indicated by the results shown in Figs. 2.5(a-c) and by the FWHM values given above, the FWHM of the envelope of each convolution calculation are in close agreement in all three materials and for all three time-domain Green's functions when $v(t)$ is represented by a 7.5 MHz center frequency pulse.

2.8 Discussion

2.8.1 Causal and noncausal time-domain Green's functions for acoustic propagation

Although the Blackstock wave equation is noncausal and the Szabo and power law wave equations are noncausal for $1 < y \leq 2$, clear demonstrations of noncausal behavior are challenging to find in locations far from the source, as shown in Fig. 2.1 for time-domain Green's functions calculations in water, breast, and liver, especially when the results are plotted on

a linear scale. However, in locations very close to the source, i.e., for water with $r \leq 1$ nm, for breast with $r \leq 10$ nm, and for liver with $r \leq 100$ zm, the noncausal contributions are clearly evident in each of these time-domain Green's function calculations. This suggests that successfully observing obvious examples of noncausal time-domain behavior produced by the Blackstock, Szabo, and power law wave equations primarily involves knowing where to look.

Fig. 2.2(a) shows that the time-domain Green's functions for the Stokes and Blackstock wave equations converge to the time-domain Green's function for the power law wave equation in calculations for water, and Figs. 2.2(a-b) show that the time-domain Green's functions for the Caputo and Szabo wave equations converge to the time-domain Green's function for the power law wave equation in calculations for breast and water, respectively, albeit at different rates. Figs. 2.1(c-d) and Fig. 2.2(a) indicate that the time-domain Green's function for the Stokes and Blackstock wave equations converge to a Gaussian function, which is the time-domain Green's function for the power law wave equation when $y = 2$. Figs. 2.1(e-f) and Fig. 2.2(b) indicate that the time-domain Green's function for the Caputo and Szabo wave equations converge to a maximally skewed stable distribution, and Figs. 2.1(k-l) and Fig. 2.2(c) also indicate that the time-domain Green's functions for the Caputo and Szabo wave equations scaled by $4\pi r$ converge to a maximally skewed stable distribution, which is the time-domain Green's function for the power law wave equation scaled by $4\pi r$ when $0 \leq y < 1$ or $1 < y \leq 2$. These figures show that, beyond a certain small distance, the time-domain Green's function for the power law wave equation is an effective approximation for the time-domain Green's functions of the Stokes, Blackstock, Caputo, and Szabo wave equations.

Fig. 2.3, which plots $20 \log_{10} \{g(r, t = 0) / \max [g(r, t)]\}$ for the Blackstock, Szabo, and power law wave equations, demonstrates that the noncausal contributions to these noncausal time-domain Green's functions are miniscule beyond a certain distance. Fig. 2.3 also demonstrates that calculations of time-domain Green's functions at $t = 0$ with the IFFT

quickly reaches a lower limit beyond a certain distance that depends on the material and on the simulation parameters. Our experience is that the STABLE toolbox achieves much better accuracy than the IFFT and is much more convenient for calculating stable pdfs and for calculating $20\log_{10}\{g(r,t=0)/\max[g(r,t)]\}$, since there is no need to compute the entire time-domain Green's function for either of these with the STABLE toolbox.

2.8.2 Convolving time-domain Green's functions with 3 cycle Hanning-weighted pulses

In Fig. 2.4, noncausal time-domain contributions are not evident in any of the numerical calculations performed with the noncausal time-domain Green's functions. This suggests that the noncausal contributions are effectively 'filtered out' by the 3 cycle Hanning-weighted pulse with a center frequency of 7.5 MHz and that the causal and noncausal models for $4\pi r g(r,t)$ considered here are equally effective for these calculations. Fig. 2.5 also suggests that convolutions between the 7.5 MHz center frequency pulse and the noncausal and the causal models for $4\pi r g(r,t)$ are all effectively represented by delta functions at the origin in all three materials for distances $r \leq 100\,\mu$m. Furthermore, Fig. 2.5 indicates that there is very little difference between the FWHM of the envelope of $4\pi r g(r,t) * v(t)$ for the causal and noncausal wave equations evaluated in these three materials, which suggests that convergence of the FWHM is achieved in all materials at all distances shown. This is in contrast to the results shown in Figs. 2.1 and 2.2, which suggest that convergence in the norm of the difference is achieved near a value of 5%.

2.8.3 Causality in acoustic wave propagation

Fig. 2.1 indicates that the concept of causality, when applied as a distinction between the time-domain Green's functions for the Stokes, Blackstock, and power law wave equations when $y = 2$ and also for the Caputo, Szabo, and power law wave equations when $1 < y < 2$, is only important very close to the source. Elsewhere, establishing the absence or presence of causality of these wave equations appears to be a purely academic exercise

because the Stokes, Blackstock, and power law wave equations generate very similar results for $y = 2$ and because the Caputo, Szabo, and power law wave equations generate very similar results for $1 < y < 2$ beyond a certain distance where the noncausal contributions are negligible. However, causality is still a very important concept for acoustic wave propagation, especially for distinguishing incoming noncausal Green's functions from outgoing causal Green's functions and for maintaining consistency between the attenuation and dispersion in acoustic wave propagation, which suggests that the importance of causality in acoustic wave propagation depends on the context. The results presented in Figs. 2.1-2.5 suggest that, except for locations very close to the source, the Stokes, Blackstock, and power law wave equations are all effective models for acoustic propagation in water and that the Caputo, Szabo, and power law wave equations are all effective models for acoustic propagation in soft tissue that either exactly or approximately satisfy the attenuation and dispersion relations in Eqs. 2.1 and 2.2, respectively.

2.9 Conclusion

Time-domain Green's functions for three time-fractional wave equations are numerically evaluated and the results are compared at different distances for water, breast, and liver. The results demonstrate that the Szabo and power law wave equations are noncausal and that the Caputo wave equation is causal, where the Szabo wave equation is a time-fractional extension of the noncausal Blackstock wave equation, and the Caputo wave equation is a time-fractional extension of the causal Stokes wave equation. Examples of noncausal behavior are observed in the time-domain Green's functions for the Blackstock, Szabo, and power law wave equations when these are evaluated very close to the source, i.e., at $r \leq 1$ nm for water, at $r \leq 10$ nm for breast, and at $r \leq 1$ zm for liver, but at much larger distances, the noncausal components of these time-domain Green's functions are miniscule. Comparisons also show that the time-domain Green's functions for the Caputo, Szabo, and power law wave equations with $1 < y < 2$ converge to the same result and that the time-domain Green's

functions for the Stokes, Blackstock, and power law wave equation with $y = 2$ converge to the same result. When these time-domain Green's functions are convolved with a three-cycle Hanning-weighted pulse, no noncausal behavior is observed in the time-domain results, and the FWHMs of the envelopes of the convolution results are all approximately the same, which indicates that the Caputo, Szabo, and power law wave equations are equally effective for these time-domain calculations.

Chapter 3

Space fractional wave equations[2]

3.1 Introduction

For time-fractional models of power law attenuation, the close connection between power law attenuation and fractional calculus is evident in the expression for the derivative operation $(j\omega)^y$ in the frequency domain, which contains the power law term ω^y. Similar expressions are also available for space-fractional models of power law attenuation after some additional mathematical manipulations.

Time-fractional and space-fractional wave equations that describe power law attenuation are often characterized through the attenuation and phase velocity, which are obtained from the imaginary and real parts of the wavenumber k, respectively. Other methods for analyzing time-fractional wave equations include the Kramers-Kronig relations [44], the Paley-Wiener theorem [43], and time-causal theories [45], and time-fractional wave equations are also evaluated through time-domain analysis of the material impulse response function (MIRF) [52] and time-domain Green's functions [53, 39]. Much of this analysis concentrates on the causality; however, the distinction between these is very subtle because the attenuation is very similar in the fractional calculus models that are presently used for medical ultrasound. Furthermore, all of the noncausal time-fractional models for power law attenuation demonstrate causal behavior at the origin (r=0), where the effects of attenuation

[2]This article has been submitted to The Journal of the Acoustical Society of America. After this paper is published, it will be found at http://asa.scitation.org/journal/jas.

and dispersion vanish. When present, the noncausal components of power law attenuation models are only evident in time-domain Green's functions evaluated very close to the origin [53]. For example, the noncausal components of the time-domain Green's function for the power law wave equation are only observed in the results of numerical calculations within 10 nm of the source for breast and only within 10 zm of the source for liver. Elsewhere, examples of noncausal behavior in the time-domain are very difficult to identify because several of the causal and noncausal time-fractional models for power law attenuation converge to the same result a short distance from the origin [53].

Determining whether a space-fractional model is causal or noncausal requires a different approach because the dispersion relations for space-fractional equations are transcendental equations. This is further confounded by the various claims that appear in the literature, where one paper indicates that the Chen-Holm space-fractional wave equation is causal [41], two other papers claim that the Chen-Holm space-fractional wave equation is noncausal [54, 55], and another paper suggests that the Treeby-Cox space-fractional wave equation is causal [42]. If these space-fractional wave equations are noncausal, then some evidence of noncausal behavior is expected close to the origin, as demonstrated in [53] for two time-fractional wave equations that are noncausal for power law exponents $1 < y < 2$. Similarly, if these space-fractional wave equations are causal, then the time-domain Green's functions are expected to consistently equal zero at all times $t < 0$, including all locations very close to the origin. Since these results have not yet been demonstrated for either of these space-fractional wave equations, additional evaluations are needed.

To definitively establish whether the Chen-Holm and Treeby-Cox wave equations are causal or noncausal and also to evaluate the similarities and differences in the time-domain Green's functions for both of these space-fractional wave equations, some new analytical expressions and numerical results are introduced. These are developed and evaluated after the fractional partial differential equations, the dispersion relations, and the time-domain Green's functions are presented for the Chen-Holm and the Treeby-Cox space-fractional

wave equations. The power law wave equation, which is a time-fractional wave equation, is also provided as a reference. Analytical expressions showing that the Chen-Holm and the Treeby-Cox space-fractional wave equations are both causal are then introduced. Next, a method is described for numerically calculating the time-domain Green's functions for these two space-fractional wave equations. Results are then presented showing that there is a small but noticeable difference between numerically calculated values for the attenuation and dispersion and the values predicted by previously published models and that the discrepancy is eliminated when additional terms are included in the approximations for the attenuation and dispersion. Results obtained from numerical evaluations of the time-domain Green's functions also reinforce that both of these space-fractional wave equations are causal. Although both of these space-fractional wave equations demonstrate similar attenuation as a function of frequency, the phase velocities for the Chen-Holm and Treeby-Cox wave equations are quite different. The results also show that the time-domain Green's functions for the Treeby-Cox wave equation and the power law wave equation yield approximately the same result a short distance from the origin. When convolved with a short input pulse, the time-domain Green's functions for the Treeby-Cox wave equation and the power law wave equation are also nearly identical, but the results obtained with the time-domain Green's function for the Chen-Holm wave equation are also different. Except for some very limited circumstances, the Treeby-Cox space-fractional wave equation and the time-fractional power law wave equation yield similar results, even though the former is causal and the latter is noncausal for power law exponents $1 < y \leq 2$.

3.2 The Chen-Holm space-fractional wave equation

The space-fractional wave equation developed by Chen and Holm [41] to describe power law attenuation is given by

$$\nabla^2 p - \frac{1}{c_0^2}\frac{\partial^2 p}{\partial t^2} - \tau \frac{\partial}{\partial t}\left(-\nabla^2\right)^{y/2} p = 0, \tag{3.1}$$

where $\tau = 2\alpha_0 c_0^{y-1}$ is the fractional relaxation time [41], p represents the pressure in Pa, and t is the time in seconds. The first two terms in Eq. 3.1 are recognized as the lossless wave equation, and the third term, which contains a fractional Laplacian, produces power law attenuation. There is no known exact analytical closed-form time-domain Green's function for the Chen-Holm wave equation, so numerical evaluations are required. To derive an approximate expression for these numerical calculations, the transfer function for an impulsive forcing function applied to the Chen-Holm wave equation is expressed in terms of the spatial Fourier transform variable k and the Laplace transform variable s, which is

$$G(k,s) = \frac{c_0^2}{\left(s + \tau k^y c_0^2/2\right)^2 + k^2 c_0^2 - \tau^2 k^{2y} c_0^4/4}. \tag{3.2}$$

The inverse Laplace transform of Eq. 3.2 then yields

$$\hat{g}(k,t) = e^{-\tau k^y c_0^2 t/2} \sin\left(k c_0 t \sqrt{1 - \tau^2 k^{2y-2} c_0^2/4}\right) \frac{c_0}{k\sqrt{1-\tau^2 k^{2y-2} c_0^2/4}} u(t) \quad \text{for} \quad k < \left(\frac{2}{\tau c_0}\right)^{\frac{1}{y-1}} \tag{3.3}$$

and

$$\hat{g}(k,t) = e^{-\tau k^y c_0^2 t/2} \sinh\left(k c_0 t \sqrt{\tau^2 k^{2y-2} c_0^2/4 - 1}\right) \frac{c_0}{k\sqrt{\tau^2 k^{2y-2} c_0^2/4-1}} u(t) \quad \text{for} \quad k > \left(\frac{2}{\tau c_0}\right)^{\frac{1}{y-1}}. \tag{3.4}$$

At $k = (2/\tau c_0)^{1/(y-1)}$, $\hat{g}(k,t) = t c_0^2 e^{-\tau k^y c_0^2 t/2} u(t)$, so $\hat{g}(k,t)$ is continuous with respect to k and t. In all three of these expressions for $\hat{g}(k,t)$, $u(t)$ is the unit step function, which guarantees that the time-domain response is equal to 0 for all times $t < 0$ and that $\hat{g}(k,t)$ is causal. The time-domain Green's function is then obtained by evaluating

$$g(r,t) = \frac{4\pi}{(2\pi)^3 r} \int_0^\infty \hat{g}(k,t) \sin(kr)\, k dk, \tag{3.5}$$

where $r = \sqrt{x^2 + y^2 + z^2}$ is the distance from a point source at the origin to an observation point at (x, y, z). The integral in Eq. 3.5 also contains the unit step function $u(t)$ through

the expressions for $\hat{g}(k,t)$, so the time-domain Green's function $g(r,t)$ for the Chen-Holm space-fractional wave equation is also causal. Although Eqs. 3.3 and 3.4 are analytical expressions, the time-domain Green's function $g(r,t)$ in Eq. 3.5 is evaluated numerically.

Approximate expressions for the phase velocity and attenuation are derived from the dispersion relation

$$k^2 = \frac{\omega^2}{c_0^2} + j\omega\tau k^y \tag{3.6}$$

with $\tau = 2\alpha_0 c_0^{y-1}$. After taking the square root of both sides of Eq. 3.6, factoring out ω/c_0 on the right hand side, and keeping the first three terms in the binomial approximation, the wavenumber is rewritten as $k \approx \omega/c_0 + j\alpha_0 c_0^y k^y + \alpha_0^2 c_0^{2y+1}\omega^{-1}k^{2y}/2$. On the right hand side, k^y is replaced by the approximation $(\omega/c_0)^y\,(1 + jy\alpha_0 c_0\omega^{y-1})$ and k^{2y} is replaced by the approximation $(\omega/c_0)^{2y}$, respectively, and all third order and higher terms with respect to α_0 are discarded. The approximate phase velocity is then obtained from the real part of the wavenumber divided by ω,

$$\frac{1}{c\,(\omega)} \approx \frac{1}{c_0} - \left(y - \frac{1}{2}\right)\alpha_0^2 c_0\omega^{2y-2}. \tag{3.7}$$

The attenuation $\alpha\,(\omega) = \alpha_0\omega^y$, which is obtained from the imaginary part of the resulting approximation for k, is the same expression given in Eq. 2.1. In Treeby and Cox [42], the attenuation for the Chen-Holm wave equation is also $\alpha\,(\omega) = \alpha_0\omega^y$, but the approximate phase velocity for the Chen-Holm wave equation is instead expressed as $c\,(\omega) \approx c_0$.

3.3 The Treeby-Cox space-fractional wave equation

Treeby and Cox [42] recognized that the Chen-Holm space-fractional wave equation correctly models the power law attenuation described by Eq. 2.1 but that the dispersion for the Chen-Holm wave equation differs from the desired expression given in Eq. 2.2. To address this problem, Treeby and Cox inserted a second space-fractional term that accounts

for the dispersion, and the resulting expression is given by [42]

$$\nabla^2 p - \frac{1}{c_0^2}\frac{\partial^2 p}{\partial t^2} + \left\{-\tau\frac{\partial}{\partial t}\left(-\nabla^2\right)^{y/2} + \eta\left(-\nabla^2\right)^{(y+1)/2}\right\} p = 0, \tag{3.8}$$

where $\tau = 2\alpha_0 c_0^{y-1}$ and $\eta = 2\alpha_0 c_0^y \tan(\pi y/2)$. In Eq. 3.8, the third and fourth terms account for the effects of attenuation and dispersion, respectively. Similar to the Chen-Holm wave equation, there is no known exact analytical closed-form time-domain Green's function for the Treeby-Cox wave equation, so numerical evaluations are required. To derive an approximate expression for these numerical calculations, the transfer function for an impulsive forcing function applied to the Treeby-Cox wave equation is expressed in terms of the spatial Fourier transform variable k and the Laplace transform variable s, which is

$$G(k,s) = \frac{c_0^2}{\left(s + \tau k^y c_0^2/2\right)^2 + k^2 c_0^2 - \tau^2 k^{2y} c_0^4/4 - \eta c_0^2 k^{y+1}}. \tag{3.9}$$

After the inverse Laplace transform of Eq. 3.9 is evaluated, the result is

$$\begin{gathered}\hat{g}(k,t) = e^{-\tau k^y c_0^2 t/2}\sin\left(k c_0 t\sqrt{1 - \tau^2 k^{2y-2} c_0^2/4 - \eta k^{y-1}}\right) \\ \frac{c_0}{k\sqrt{1-\tau^2 k^{2y-2} c_0^2/4 - \eta k^{y-1}}} u(t) \quad \text{for} \quad k < \kappa\end{gathered} \tag{3.10}$$

and

$$\begin{gathered}\hat{g}(k,t) = e^{-\tau k^y c_0^2 t/2}\sinh\left(k c_0 t\sqrt{\tau^2 k^{2y-2} c_0^2/4 + \eta k^{y-1} - 1}\right) \\ \frac{c_0}{k\sqrt{\tau^2 k^{2y-2} c_0^2/4 + \eta k^{y-1} - 1}} u(t) \quad \text{for} \quad k > \kappa,\end{gathered} \tag{3.11}$$

where $\kappa = \left[\left(\eta + \sqrt{\eta^2 + \tau^2 c_0^2}\right)/2\right]^{-1/(y-1)}$. At $k = \kappa$, $\hat{g}(k,t) = t c_0^2 e^{-\tau \kappa^y c_0^2 t/2} u(t)$, so the expression for $\hat{g}(k,t)$ is continuous with respect to k and t. The unit step function $u(t)$ in all three of these expressions for $\hat{g}(k,t)$ indicates that $\hat{g}(k,t)$ is causal. The time-domain Green's function for the Treeby-Cox space-fractional wave equation is calculated with Eq. 3.5 combined with the expressions for $\hat{g}(k,t)$, and due to the presence of $u(t)$ in each expression

for $\hat{g}(k,t)$, the time-domain Green's function $g(r,t)$ for the Treeby-Cox space-fractional wave equation is also causal.

The phase velocity and attenuation for the Treeby-Cox space-fractional wave equation are derived from the dispersion relation

$$k^2 = \frac{\omega^2}{c_0^2} + j2\alpha_0 c_0^{y-1}\omega k^y + 2\alpha_0 c_0^y \tan(\pi y/2)\, k^{y+1}, \tag{3.12}$$

starting with the assumption that the attenuation and dispersion are both small relative to ω/c_0. The binomial approximation is then applied to Eq. 3.12, and the first three terms are retained, yielding

$$\begin{aligned} k \approx \tfrac{\omega}{c_0} + \alpha_0 c_0^y \left(jk^y + \tan(\pi y/2)\, c_0\omega^{-1}k^{y+1}\right) \\ -\tfrac{1}{2}\alpha_0^2 c_0^{2y+1}\omega^{-1}\left(jk^y + \tan(\pi y/2)\, c_0\omega^{-1}k^{y+1}\right)^2. \end{aligned} \tag{3.13}$$

On the right hand side, k^y is replaced with $(\omega/c_0)^y\left[1 + y\alpha_0 c_0\omega^{y-1}\left(j + \tan(\pi y/2)\right)\right]$ and k^{y+1} is replaced with $(\omega/c_0)^{y+1}\left[1 + (y+1)\,\alpha_0 c_0\omega^{y-1}\left(j + \tan(\pi y/2)\right)\right]$, respectively, and all third order and higher terms with respect to α_0 are discarded. The approximate phase velocity is obtained from the real part of the wavenumber divided by ω,

$$\frac{1}{c(\omega)} \approx \frac{1}{c_0} + \tan(\pi y/2)\,\alpha_0\omega^{y-1} + \left[-y + \frac{1}{2} + \left(y + \frac{1}{2}\right)\tan^2(\pi y/2)\right]\alpha_0^2 c_0\omega^{2y-2}, \tag{3.14}$$

and the approximate attenuation is the imaginary part of the wavenumber,

$$\alpha(\omega) \approx \alpha_0\omega^y + 2y\tan(\pi y/2)\,\alpha_0^2 c_0\omega^{2y-1}. \tag{3.15}$$

Treeby and Cox [42] instead express the approximate phase velocity and attenuation for the Treeby-Cox wave equation as $1/c(\omega) \approx 1/c_0 + \tan(\pi y/2)\,\alpha_0\omega^{y-1}$ and $\alpha(\omega) \approx \alpha_0\omega^y$, respectively.

3.4 Methods

3.4.1 Dispersion Relations

The attenuation and phase velocity of the power law wave equation are calculated with Eqs. 2.1 and 2.2, respectively. For the Chen-Holm and the Treeby-Cox space-fractional wave equations, since there is no analytical solution, the phase velocity and attenuation are both calculated using the "fsolve" routine in Matlab. This Matlab function applies the Levenberg–Marquardt algorithm to numerically determine the complex value of k that solves the dispersion relations in Eqs. 3.6 and 3.12 using the initial value $k = \omega/c_0$.

3.4.2 The Pantis Method

Numerical calculations of the time-domain Green's functions for the Chen-Holm and Treeby-Cox wave equations are challenging because Eq. 3.5 is a highly oscillatory improper integral. When applied to this problem, most standard numerical integration techniques perform poorly, so an alternative approach is required. The Pantis method [56, 57] provides an ideal solution to this problem, where the improper integral in Eq. 3.5 is rewritten as the sum of a proper integral and an improper integral according to

$$g(r,t) = \frac{4\pi}{(2\pi)^3 r} \int_0^\infty k\hat{g}(k,t) \sin(kr)\, dk = \frac{4\pi}{(2\pi)^3 r} \left[I_1(r,t) + I_2(r,t) \right], \tag{3.16}$$

with

$$I_1(r,t) = \int_0^{m\pi/r} k\hat{g}(k,t) \sin(kr)\, dk, \tag{3.17}$$

and

$$I_2(r,t) = \int_{m\pi/r}^\infty k\hat{g}(k,t) \sin(kr)\, dk. \tag{3.18}$$

The integral $I_1(r,t)$ is evaluated with Filon's method [58, 59, 60], which approximates $k\hat{g}(k,t)$ with a piecewise second order polynomial. Filon's method is implemented within a Matlab

routine [59], where the input parameters include the Matlab function handle, the lower and upper limits of integration, and the number of points at which the integrand is evaluated. Each numerical evaluation of $I_1(r,t)$ with Filon's method is calculated with 70,000 abscissas, which is sufficient for convergence at all temporal and spatial points evaluated here for both breast and liver. After integrating by parts and recognizing that $[k\hat{g}(k,t)]\Big|_{k=\infty} = 0$, the integral $I_2(r,t)$ over the upper subinterval is rewritten as

$$I_2(r,t) = k\hat{g}(k,t)\frac{\cos(kr)}{r}\Bigg|_{k=m\pi/r} - \frac{\partial}{\partial k}\left[k\hat{g}(k,t)\right]\frac{\sin(kr)}{r^2}\Bigg|_{k=m\pi/r}$$

$$- \int_{m\pi/r}^{\infty} \frac{\partial}{\partial k}\left[k\hat{g}(k,t)\right]\frac{\sin(kr)}{r^2}dk. \tag{3.19}$$

For these calculations, m is an odd integer, and only the first term in Eq. 3.19 is retained. Thus, $I_2(r,t) \approx -m\pi\hat{g}(m\pi/r,t)/r^2$, which is an effective approximation for these calculations when m is sufficiently large and when the contribution from $I_2(r,t)$ is relatively small. Also, when m is an odd integer, the second term in Eq. 3.19 disappears, and when m is odd, $I_1(r,t)$ is consistently positive for the expressions considered here. An odd value of m is advantageous for these calculations because an even value of m can yield a negative value for $I_1(r,t)$, which is undesirable because $g(r,t) \geq 0$ for all values of r and t. The value $m = 1601$ yields effective results for all (r,t) pairs evaluated here. Also, to avoid problems with numerical overflow when the argument of the $\sinh(\cdot)$ function grows large, $\exp(-a)\sinh(b)$ is instead calculated using $\left(e^{b-a} - e^{-b-a}\right)/2$.

3.4.3 Time windows for computed time-domain Green's functions

The start and end times for all time-domain Green's function calculations are adjusted manually for each location such that each waveform fills a significant portion of the time window. For both the Chen-Holm wave equation and the Treeby-Cox wave equation, $g(r,t) = 0$ at $t = 0$ because $\hat{g}(k,t) = 0$ for all values of k when $t = 0$, which is the analytical result obtained through direct substitution of $t = 0$ into Eqs. 3.3-3.4 and Eqs. 3.10-3.11. The unit

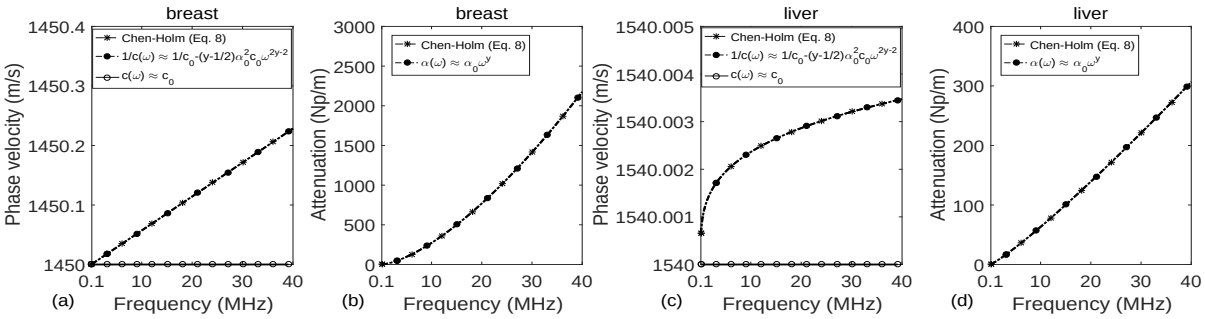

Figure 3.1: Phase velocity and attenuation in breast and liver obtained from the dispersion relation in Eq. 3.6 for the Chen-Holm wave equation ($*$) and two different approximations ($\bullet$ and $\circ$) to the dispersion relation for the Chen-Holm wave equation.

step function $u(t)$ also guarantees that $\hat{g}(k,t) = 0$ for all $t < 0$, so $g(r,t) = 0$ for all $t < 0$ in the Chen-Holm and Treeby-Cox wave equations. For the power law wave equation, the time-domain Green's function is calculated in Matlab with the STABLE toolbox [47, 53], which numerically evaluates the expression for the stable pdf in Eq. 2.13. The time window defined for time domain Green's function calculations very close to the source includes negative time values to capture the noncausal components of the response in these locations. In all plots, the arrival time r/c_0 in a lossless medium is also indicated to provide a time reference.

3.5 Results

3.5.1 Phase velocity and attenuation in breast and liver

Fig. 3.1 shows the exact and approximate frequency-dependent phase velocity and attenuation for the Chen-Holm space-fractional wave equation using values for human breast with $y = 1.5$, $\alpha_0 = 0.086$ Np/cm/MHz$^{1.5}$, and $c_0 = 1450$ m/s and using values for human liver with $y = 1.139$, $\alpha_0 = 0.0459$ Np/cm/MHz$^{1.139}$, and $c_0 = 1540$ m/s. The frequency range is 0.1 to 40 MHz, and the step size on the horizontal axis is $\Delta f = 0.3$ MHz for each of the phase velocity and attenuation plots. For the Chen-Holm wave equation, the result obtained with the Matlab "fsolve" routine applied to Eq. 3.6 is indicated by dashed lines with star markers

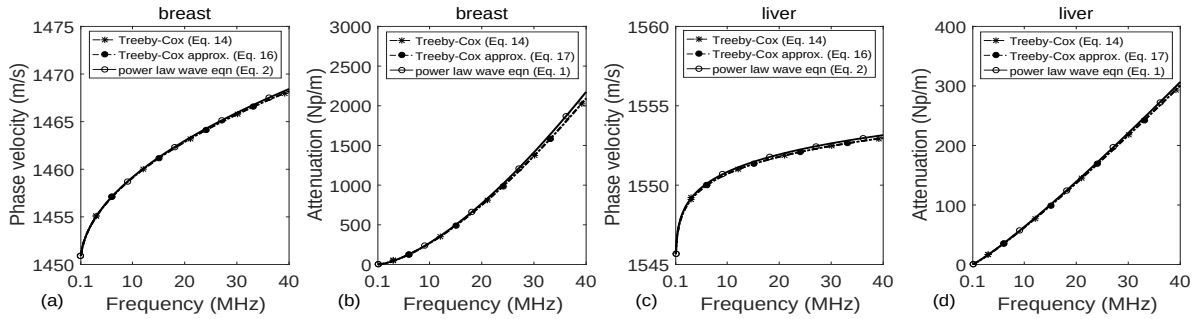

Figure 3.2: Phase velocity and attenuation in breast and liver obtained from the dispersion relation in Eq. 3.12 for the Treeby-Cox wave equation ($*$), the approximations to the dispersion relation for the Treeby-Cox wave equation given in Eqs. 3.14-3.15 ($\bullet$), and the attenuation and phase velocity for the power law wave equation given in Eqs. 2.1-2.2 ($\circ$).

($*$), and the approximate solution from Eq. 3.7 is indicated by dot-dashed lines with solid dot markers ($\bullet$). The zero-order approximation to the phase velocity $c(\omega) \approx c_0$ is indicated by a solid line with circle markers ($\circ$) in Figs. 3.1(a) and 3.1(c). Figs. 3.1(a) and 3.1(c) show that the approximation to $c(\omega)$ introduced in Eq. 3.7 demonstrates excellent agreement with the numerical solution of Eq. 3.6. Figs. 3.1(a) and 3.1(c) also indicate that the phase velocity of the Chen-Holm wave equation is not quite equal to c_0 because $c(\omega)$ increases slightly as the frequency increases. In addition, Fig. 3.1(b) shows that the attenuation predicted by the Chen-Holm wave equation follows the power law indicated by Eq. 2.1 very closely in breast. Furthermore, Figs. 3.1(a) and 3.1(c) demonstrate that the change in the phase velocity in liver over this frequency range is much less than the change in the phase velocity in breast, and Figs. 3.1(b) and 3.1(d) indicate that the attenuation of liver is much smaller than that of breast.

Fig. 3.2 shows the exact and approximate values for the phase velocity and attenuation of the Treeby-Cox space-fractional wave equation and the exact phase velocity and attenuation of the power law wave equation using the same parameters evaluated in Fig. 3.1. For the Treeby-Cox wave equation, the numerical results obtained with the Matlab "fsolve" routine applied to Eq. 3.12 are indicated by dashed lines with star markers ($*$), and the approximate solution from Eq. 3.14 is indicated by dot-dashed lines with solid dot markers ($\bullet$). For the

power law wave equation, which exactly satisfies Eqs. 2.1 and 2.2, the results are indicated by solid lines with circle markers (○). Figs. 3.2(a-d) show that the approximations introduced in Eqs. 3.14-3.15 closely match the numerical values obtained from Eq. 3.12. Fig. 3.2 also shows that the phase velocity and attenuation curves are similar for the power law wave equation and the Treeby-Cox wave equation; however, there is a small but noticeable difference between these curves that is associated with the higher order terms on the right hand side of Eqs. 3.14-3.15. Fig. 3.2(b) indicates that the difference between the attenuation for the Treeby-Cox wave equation and the power law wave equation increases slightly as the frequency grows larger. For example, at $f = 40$ MHz, the phase velocities obtained from Eq. 3.12 (the dispersion relation for the Treeby-Cox wave equation) with the "fsolve" routine in Matlab, Eqs. 3.14-3.15 (approximations to the phase velocity and the attenuation for the Treeby-Cox wave equation), and Eqs. 2.1-2.2 (the exact attenuation and phase velocity for the power law wave equation) in breast are 1468.2 m/s, 1468.2 m/s, and 1468.4 m/s, and the corresponding attenuations are 2096.6 Np/m, 2093.7 Np/m, and 2175.6 Np/m, respectively. At $f = 40$ MHz, the corresponding phase velocities in liver are 1553.0 m/s, 1553.0 m/s, and 1553.1 m/s, and the attenuations are 300.79 Np/m, 300.68 Np/m, and 306.59 Np/m, respectively. Thus, at $f = 40$ MHz and at all other frequencies evaluated in Fig. 3.2, Eqs. 3.14-3.15 are better approximations for the phase velocity and attenuation of the Treeby-Cox wave equation than Eqs. 2.2 and 2.1, where the largest differences are observed at $f = 40$ MHz. Also, the phase velocity and attenuation are slightly smaller for the Treeby-Cox wave equation than for the power law wave equation. Figs. 3.2(a) and 3.2(c) also demonstrate that the change in the phase velocity in liver over this frequency range is smaller than the change in the phase velocity in breast, and Figs. 3.2(b) and 3.2(d) show that the attenuation for liver is much less than that for breast over the range of frequencies evaluated here. In Figs. 3.2(a) and 3.2(c), the differences in the phase velocities for the power law wave equation and the Treeby-Cox wave equation are due to the contribution from the third term in Eq. 3.14, and in Figs. 3.2(b) and 3.2(d), the differences in the attenuation for

the power law wave equation and the Treeby-Cox wave equation are due to the contribution from the second term in Eq. 3.15.

3.5.2 Time-domain Green's functions calculated for breast

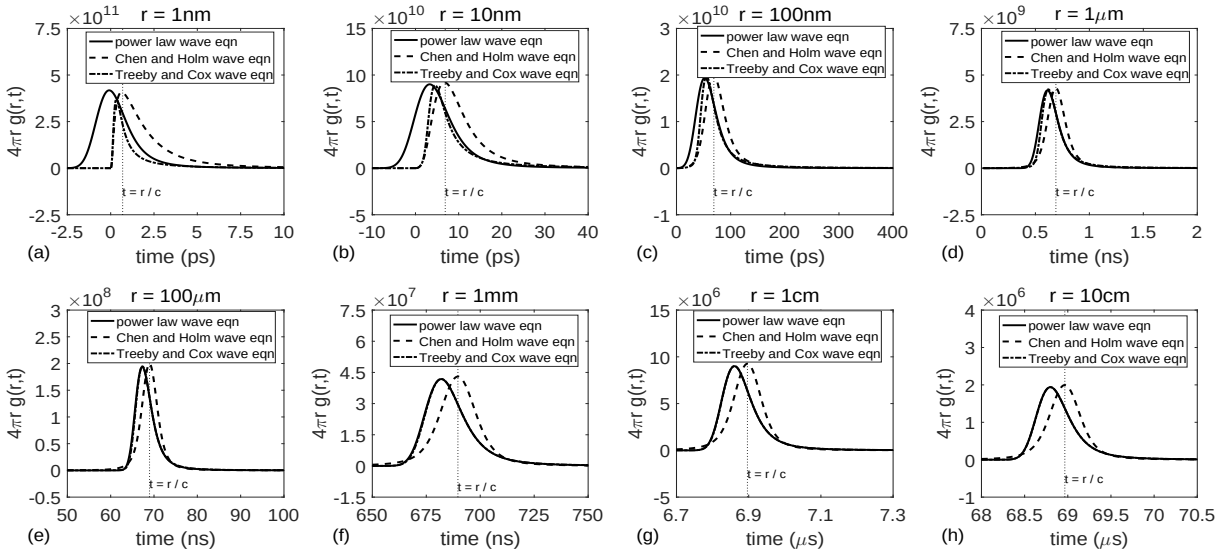

Figure 3.3: Time-domain Green's functions scaled by $4\pi r$ calculated for breast with $y = 1.5$, $\alpha_0 = 0.086$ Np/cm/MHz$^{1.5}$, and $c_0 = 1450$ m/s at (a) $r = 1$ nm, (b) $r = 10$ nm, (c) $r = 100$ nm, (d) $r = 1\,\mu$m, (e) $r = 100\,\mu$m, (f) $r = 1$ mm, (g) $r = 1$ cm, and (h) $r = 10$ cm with the power law (solid line), Chen-Holm (dashed line), and Treeby-Cox (dot-dashed line) wave equations. At all distances, the time-domain Green's functions for the Chen-Holm and Treeby-Cox wave equations evaluated for breast are causal while the time-domain Green's function for the power law wave equation is clearly non-causal for $r = 1\,n$m and $r = 10\,n$m. Beyond about $r = 100\,\mu$m, the time-domain Green's functions for the power law wave equation and the Treeby-Cox wave equation are nearly indistinguishable, while the time-domain Green's function for the Chen-Holm wave equation is distinct from the time-domain Green's functions for the time-fractional power law wave equation and the space-fractional Treeby-Cox wave equation at all distances.

To demonstrate some of the similarities and differences between these three fractional wave equations evaluated at various distances, Fig. 3.3 shows the time-domain Green's functions multiplied by $4\pi r$ for the power law wave equation (solid line), the Chen-Holm wave equation (dashed line), and the Treeby-Cox wave equation (dot-dashed line) calculated for human breast with $y = 1.5$, $c_0 = 1450$ m/s, and $\alpha_0 = 0.086$ Np/cm/MHz$^{1.5}$. The results are computed at $r = 1$ nm, $r = 10$ nm, $r = 100$ nm, $r = 1\,\mu$m, $r = 100\,\mu$m, $r = 1$ mm,

$r = 1$ cm, and $r = 10$ cm. The units defined for the horizontal axis in Fig. 3.3 are picoseconds, nanoseconds, or microseconds. The vertical dashed line describes the time $t = r/c_0$ in each subfigure. Figs. 3.3(a) and 3.3(b) show that the Green's function for the power law wave equation is noncausal at $r = 1$ nm and $r = 10$ nm since the Green's function for the power law wave equation is clearly nonzero before time $t = 0$ in these two subfigures. However, the Green's functions for the Chen-Holm wave equation and the Treeby-Cox wave equation are both causal as these two Green's functions are always equal to zero for all times $t \leq 0$, as demonstrated in sections 3.2 and 3.3, respectively. The amplitudes of the Green's functions for these three wave equations are similar in each individual subfigure, and the amplitudes change by a significant amount in each successive subfigure. For example, the values of the peaks in Fig. 3.3(a) are all approximately 4×10^{11} s^{-1}, and the values of the peaks in Fig. 3.3(b) are all around 9×10^{10} s^{-1}. Three distinct peaks are observed in Figs. 3.3(a) and 3.3(b), and then the peaks of the time-domain Green's functions for the power law wave equation and the Treeby-Cox wave equation start to move much closer together in Figs. 3.3(c) and 3.3(d) while the peak for the Chen-Holm wave equation remains distinct from the peaks for the other two fractional wave equations in each subfigure. In Figs. 3.3(e)-3.3(h), the waveforms for the Chen-Holm wave equation are consistently quite different from those obtained with the power law and Treeby-Cox wave equations. This is expected because the phase velocity for the Chen-Holm wave equation is approximately equal to c_0 for all frequency components; however, the phase velocity demonstrates much greater variation as a function of frequency in the power law and Treeby-Cox wave equations. Furthermore, in Figs. 3.3(e)-3.3(h), the time-domain Green's functions for the power law wave equation and the Treeby-Cox wave equation are nearly indistinguishable, which suggests that these two time-domain Green's functions are converging to the same result. Fig. 3.3 shows that the shape of the time-domain Green's function is the same in all eight subfigures for the power law wave equation, where the amplitude and time-scaling is different in each subfigure. However, the shapes of the time-domain Green's functions for the other two fractional wave equations

change as a function of distance. For instance, Fig. 3.3(a) shows that the waveforms for the Chen-Holm and Treeby-Cox wave equations both experience abrupt changes at $t = 0$, whereas the corresponding waveforms for these two fractional wave equations are smooth at all time points shown in Fig. 3.3(e).

3.5.3 Time-domain Green's functions calculated for liver

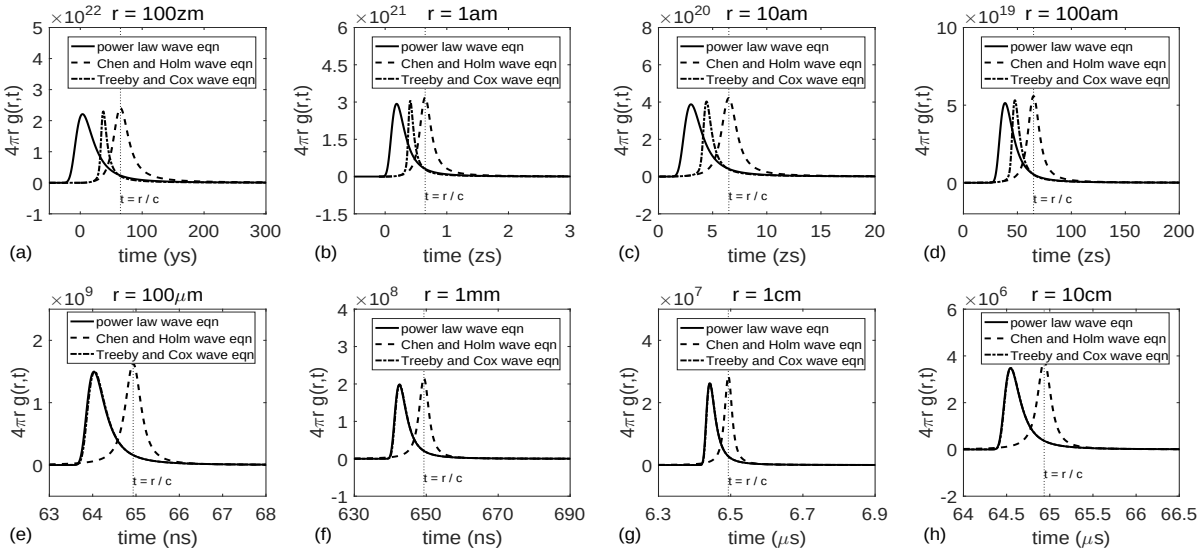

Figure 3.4: Time-domain Green's functions scaled by $4\pi r$ calculated for liver with $y = 1.139$, $\alpha_0 = 0.0459$ Np/cm/MHz$^{1.139}$, and $c_0 = 1540$ m/s at (a) $r = 100$ zm, (b) $r = 1$ am, (c) $r = 10$ am, (d) $r = 100$ am, (e) $r = 100\,\mu$m, (f) $r = 1$ mm, (g) $r = 1$ cm, and (h) $r = 10$ cm with the power law (solid line), Chen-Holm (dashed line), and Treeby-Cox (dot-dashed line) wave equations. At all distances, the time-domain Green's functions for the Chen-Holm and Treeby-Cox wave equations evaluated for liver are causal while the time-domain Green's function for the power law wave equation is clearly non-causal for $r = 100\,z$m. Beyond about $r = 100\,\mu$m, the time-domain Green's functions for the power law wave equation and the Treeby-Cox wave equation are nearly indistinguishable, while the time-domain Green's function for the Chen-Holm wave equation is consistently distinct from the time-domain Green's functions for the time-fractional power law wave equation and the space-fractional Treeby-Cox wave equation at all distances.

Fig. 3.4 shows the time-domain Green's functions multiplied by $4\pi r$ for the power law wave equation (solid line), the Chen-Holm wave equation (dashed line), and the Treeby-Cox

wave equation (dot-dashed line) calculated for human liver with $y = 1.139$, $c_0 = 1540$ m/s, and $\alpha_0 = 0.0459$ Np/cm/MHz$^{1.139}$. In Fig. 3.4, the three time-domain Green's functions are evaluated at $r = 100$ zm, $r = 1$ am, $r = 10$ am, $r = 100$ am, $r = 100\,\mu$m, $r = 1$ mm, $r = 1$ cm, and $r = 10$ cm. The units defined for the horizontal axis in Fig. 3.4 are yoctoseconds (ys or 10^{-24} seconds), zeptoseconds (zs or 10^{-21} seconds), nanoseconds (ns), or microseconds (μs). The vertical dashed line describes the time $t = r/c_0$ in each subfigure. In Fig. 3.4, the first row of subfigures shows that at relatively short distances, the time-domain Green's functions for the power law wave equation, the Chen-Holm wave equation, and the Treeby-Cox wave equation are again all noticeably different. Fig. 3.4(a) shows that the time-domain Green's function for the power law wave equation is noncausal at $r = 100$ zm since this time-domain Green's function is clearly nonzero before time $t = 0$. However, the time-domain Green's functions for the Chen-Holm wave equation and the Treeby-Cox wave equation are both causal as these are consistently equal to zero for all times $t \leq 0$. Figs. 3.4(a)-3.4(d) show that, compared to the results calculated for breast, a much shorter distance is required to show the noncausal behavior of the power law wave equation in liver. The amplitudes of the Green's functions for these three wave equations are again similar in each individual subfigure, and the amplitudes again decrease by a significant amount in each successive subfigure. For instance, the values of the peaks in Fig. 3.4(a) are all approximately 2×10^{22} s^{-1}, and the values of the peaks in Fig. 3.4(b) are all near 3×10^{21} s^{-1}. Three distinct peaks are observed in Figs. 3.4(a)-3.4(d), while the peaks for the power law wave equation and the Treeby-Cox wave equation are very close together in Figs. 3.4(e)-3.4(h). In each subfigure, the location of the peak for the Chen-Holm wave equation is distinct from the peak locations for the other two wave equations. Furthermore, in Figs. 3.4(e)-3.4(h), the time-domain Green's functions for the power law wave equation and the Treeby-Cox wave equation are nearly indistinguishable, and with increasing distance, these two time-domain Green's functions are converging to the same result.

3.5.4 Amplitude and full width at half maximum (FWHM) values in breast and liver

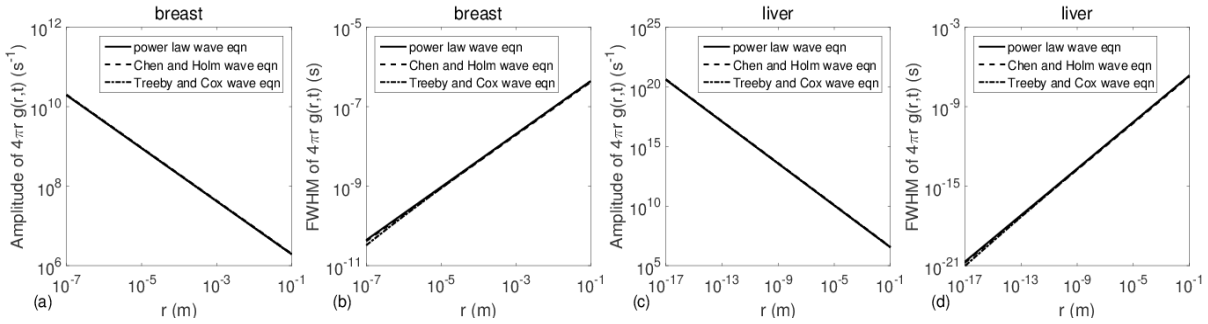

Figure 3.5: The (a,c) amplitudes and (b,d) FWHM values of the time-domain Green's functions calculated for the power law, Chen-Holm, and Treeby-Cox wave equations in (a,b) breast and (c,d) liver. The amplitudes of all three time-domain Green's functions decrease as the distance increases while the FWHM values of all three time-domain Green's functions increase as the distance increases. The amplitudes of the time-domain Green's functions for all three of these fractional wave equations are very similar at each distance, and the FWHM values are all approximately the same at longer distances, although there is a small difference in the FWHM values at shorter distances that diminishes with increasing distance.

Fig. 3.5 shows the amplitudes and full width at half maximum (FWHM) values for the time-domain Green's functions multiplied by $4\pi r$ in breast and liver for the power law wave equation (solid line), the Chen-Holm wave equation (dashed line), and the Treeby-Cox wave equation (dot-dashed line), where these four subfigures summarize the effects of attenuation and dispersion in the time-domain. The initial distances are $r = 100$ nm for breast and $r = 100$ am for liver, and each plot ends at $r = 10$ cm. Figs. 3.5(a) and 3.5(c) indicate that the amplitudes of the time-domain Green's functions for these three fractional wave equations, which are plotted on a log-log scale, decrease with frequency as the distance increases due to the effect of attenuation. Also, the amplitudes of the time-domain Green's functions for three wave equations are all very similar at all distances for both breast and liver. The slopes of the amplitudes in Fig. 3.5(a) and 3.5(c) are -0.6677 and -0.8790, respectively, where the absolute values of these two quantities are approximately equal to the reciprocals of the power law exponents in breast and liver, respectively. Figs. 3.5(b) and 3.5(d), which are plotted

on a log-log scale, show that the FWHM values of the time-domain Green's functions for these three fractional wave equations increase with distance due to the effect of dispersion. In Figs. 3.5(b) and 3.5(d), the FWHM values of the time-domain Green's functions for these three fractional wave equations differ slightly close to the source. For example, the FWHM values of the time-domain Green's functions for the power law, Chen-Holm, and Treeby-Cox wave equations are 4.4×10^{-11} s, 4.1×10^{-11} s, and 3.3×10^{-11} s at $r = 100$ nm in breast, respectively, and 2.0×10^{-21} s, 1.7×10^{-21} s, and 9.4×10^{-22} s at $r = 100$ am in liver, respectively. At larger distances, the FWHM values of the time-domain Green's functions for all three wave equations yield nearly the same result even though the shape of the time-domain Green's function for the Chen-Holm wave equation is distinct from the shapes of the time-domain Green's functions for the power law and Treeby-Cox wave equations. Figs. 3.5(b) and 3.5(d) also show that, at $r = 10$ cm, the FWHM values of the time-domain Green's functions for the power law, Chen-Holm, and Treeby-Cox wave equations are equal to 4.4×10^{-7} s, 4.1×10^{-7} s, and 4.4×10^{-7} s in breast, respectively, and 2.2×10^{-7} s, 1.9×10^{-7} s, and 2.2×10^{-7} s in liver, respectively. In Fig. 3.5(b) and 3.5(d), the slopes of the FWHM values are 0.6711 and 0.8825, which are approximately equal to the reciprocals of the power law exponents in breast and liver, respectively.

3.5.5 Time-domain Green's functions convolved with a three cycle Hanning-weighted pulse

Fig. 3.6 shows the waveforms obtained when a three cycle Hanning-weighted pulse [50, 51] is convolved with the time-domain Green's functions for the power law wave equation (solid line), the Chen-Holm wave equation (dashed line), and the Treeby-Cox wave equation (dot-dashed line) multiplied by $4\pi r$ evaluated at $r = 1$ cm in breast with $y = 1.5$, $\alpha_0 = 0.086$ Np/cm/MHz$^{1.5}$, and $c_0 = 1450$ m/s. This figure shows how power law attenuation and phase velocity influence the shape of a short pulse. In Fig. 3.6, input pulses with two

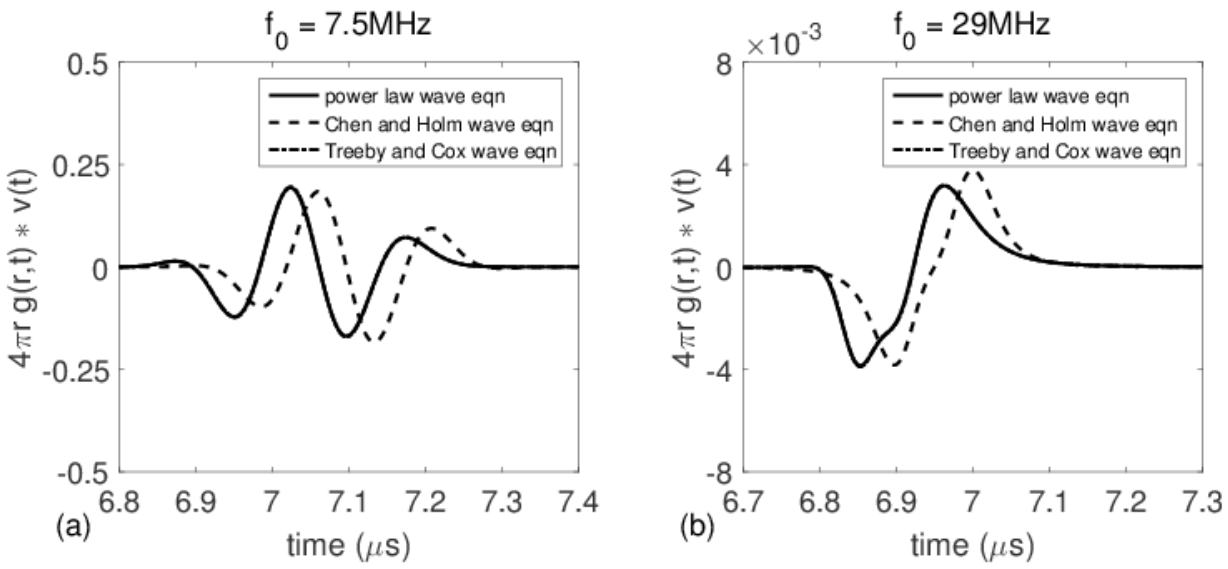

Figure 3.6: Simulated three-cycle Hanning-weighted pulses with center frequencies (a) $f_0 = 7.5$ MHz and (b) $f_0 = 29$ MHz convolved with time-domain Green's functions for the power law, Chen-Holm, and Treeby-Cox wave equations multiplied by $4\pi r$ evaluated for breast at $r = 1$ cm. The convolution results for the power law wave equation and the Treeby-Cox wave equation are very similar while the convolution result for the Chen-Holm wave equation clearly shows a time delay. Significant attenuation and waveform spreading are observed for all three signals in (b) produced by inputs with $f_0 = 29$ MHz, whereas a moderate amount of attenuation and waveform spreading is observed for all three signals in (a) produced by inputs with $f_0 = 7.5$ MHz.

different center frequencies, $f_0 = 7.5$ MHz and $f_0 = 29$ MHz, are evaluated to highlight the differences in the resulting waveforms. Fig. 3.6 indicates that the convolution results for the power law wave equation and the Treeby-Cox wave equation are nearly indistinguishable for pulses with $f_0 = 7.5$ MHz and $f_0 = 29$ MHz while the convolution results for the Chen-Holm wave equation evaluated at these two frequencies contain a significant time delay because of the substantial difference in the phase velocity. In particular, when the time delay is defined as the time between the peaks, the time delay between the convolution results for the power law wave equation and the Chen-Holm wave equation is 35 ns in Fig. 3.6(a), and the time delay between the convolution results for the power law wave equation and the Chen-Holm wave equation is 41 ns in Fig. 3.6(b), whereas the time delay between the convolution results for the power law wave equation and the Treeby-Cox wave equation is less than 1 ns in

Figs. 3.6(a) and 3.6(b). In Fig. 3.6(a), the amplitudes of all three waveforms are comparable and the waveform shapes are also similar. This indicates that the attenuation is nearly the same in all three waveforms and that the amount of waveform spreading (dispersion) for the propagating waveforms is also approximately the same. In Fig. 3.6(b), the amplitudes are again similar and the amount of spreading is similar for all three waveforms. The convolution results for the power law wave equation and the Treeby-Cox wave equation are again nearly indistinguishable, but the waveform shape for the Chen-Holm wave equation convolution result is somewhat different from the other two, where the source of this difference is again the phase velocity. Also, relative to Fig. 3.6(a), the signal amplitude drops off considerably in Fig. 3.6(b), and the filtering and spreading of the signal in the time domain is much more significant in Fig. 3.6(b), where the initial duration of the three cycle 29 MHz pulse is $0.103\,\mu$s. Since the FWHM values are approximately equal to $0.09\,\mu$s for all three of these at $r = 1$ cm, which is larger than one period of the 29 MHz center frequency, namely $0.035\,\mu$s, the attenuation and waveform spreading are more significant in Fig. 3.6(b) than in Fig. 3.6(a). In contrast, one period of the 7.5 MHz center frequency is $0.133\,\mu$s, which is larger than the FWHM values $0.09\,\mu$s of all three time-domain Green's functions at $r = 1$ cm, so there is much less attenuation and waveform spreading in Fig. 3.6(a).

Fig. 3.7 shows the results obtained when a three cycle Hanning-weighted pulse is convolved with the time-domain Green's functions for the power law wave equation (solid line), the Chen-Holm wave equation (dashed line), and the Treeby-Cox wave equation (dot-dashed line) multiplied by $4\pi r$ evaluated at $r = 1$ cm for liver with $y = 1.139$, $\alpha_0 = 0.0459$ Np/cm/MHz$^{1.139}$, and $c_0 = 1540$ m/s. The center frequencies are again equal to $f_0 = 7.5$ MHz and $f_0 = 29$ MHz. As indicated in Fig. 3.7(a), the convolution results for the power law wave equation and the Treeby-Cox wave equation also track very closely for both pulses while the convolution result for the Chen-Holm wave equation contains a noticeable time delay. For example, the time delay between the convolution results for the power law wave equation and the Chen-Holm wave equation is 44 ns in Fig. 3.7(a),

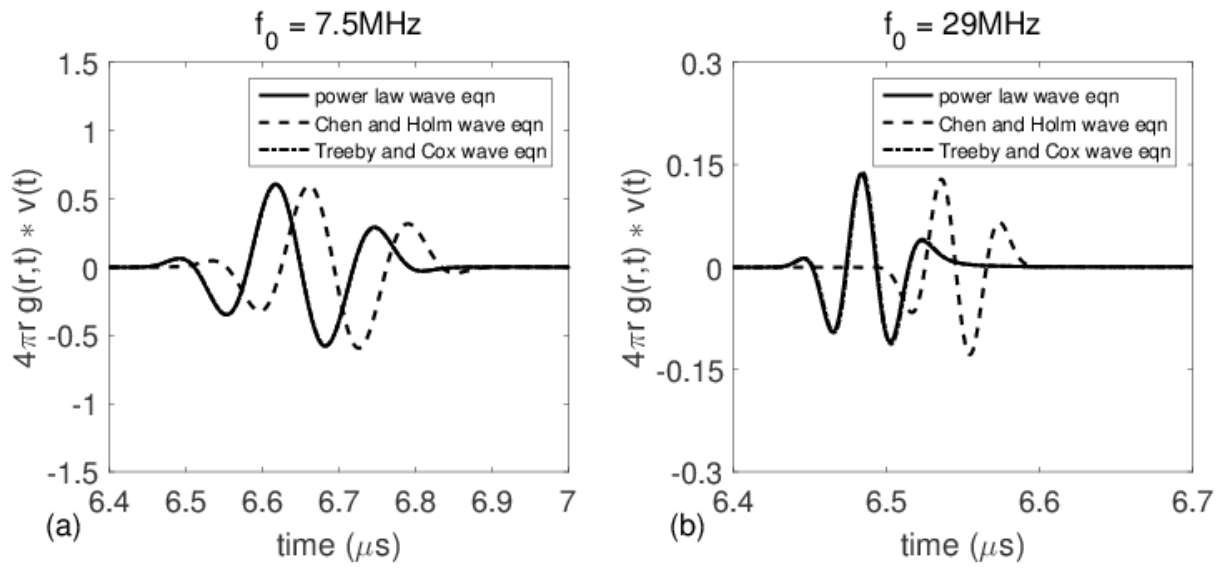

Figure 3.7: Simulated three-cycle Hanning-weighted pulses with center frequencies (a) $f_0 = 7.5$ MHz and (b) $f_0 = 29$ MHz convolved with time-domain Green's functions for the power law, Chen-Holm, and Treeby-Cox wave equations multiplied by $4\pi r$ evaluated for liver at $r = 1$ cm. The convolution results for the power law wave equation and the Treeby-Cox wave equation are very similar while the convolution result for the Chen-Holm wave equation clearly shows a time delay. A moderate amount of attenuation and waveform spreading are observed for all three signals in (b) produced by inputs with $f_0 = 29$ MHz, whereas a smaller amount of attenuation and waveform spreading is observed for all three signals in (a) produced by inputs with $f_0 = 7.5$ MHz.

and the time delay between the convolution results for the power law wave equation and the Chen-Holm wave equation is 52 ns in Fig. 3.7(b), whereas the time delay between the convolution results for the power law wave equation and the Treeby-Cox wave equation is again less than 1 ns in Figs. 3.7(a) and 3.7(b). Fig. 3.7(a) also shows that the amplitudes of all three waveforms are almost the same and the shapes of these waveforms are again similar, which indicates that the amount of attenuation and dispersion is nearly the same in all three waveforms. Fig. 3.7 shows that there is more attenuation and dispersion for the 29 MHz signal in Fig. 3.7(b) relative to the 7.5 MHz signal in Fig. 3.7(a) and that the shape of the three cycle Hanning-weighted input pulse is still recognizable in Fig. 3.7(b).

3.6 Discussion

3.6.1 Numerical evaluations of the inverse 3D Fourier transform

Numerical evaluations of improper integrals with highly oscillatory integrands are often challenging. Certain methods, such as the Matlab "quadgk" routine, which is based on adaptive Gauss-Kronrod quadrature, and the Matlab "integral" routine, which is based on global adaptive quadrature, are able to evaluate some improper integrals. Unfortunately, neither of these methods consistently converge to the correct result when applied to Eq. 3.5. Although Filon's formula provides an effective method for evaluating integrals with highly oscillatory integrands, Filon's formula yields inconsistent results when applied to Eq. 3.5 because the upper limit of integration is infinite. However, the Pantis method [56, 57] solves this problem by applying Filon's formula to the integral $I_1(r,t)$ with finite limits of integration, and then the first term of an infinite sum approximates the contribution from the remaining improper integral $I_2(r,t)$. To determine whether numerical convergence is achieved at a given distance, the result is compared to the result obtained with twice as many Filon abscissas and to a value for m that is twice as large. If the Euclidean norm of the difference between the two results is within 1×10^{-3}, then the two results are sufficiently close and convergence is achieved. For instance, at $r = 1$ nm for breast and $r = 100$ zm for liver, 900 Filon abscissas and $m = 21$ are sufficient to achieve convergence at all time points in Figs. 3.3(a) and 3.4(a). However, at $r = 100\,\mu$m for liver, convergence at all time points is achieved with 35,000 Filon abscissas and $m = 801$. Convergence is achieved at all values of r and t for calculations in breast and liver with 70,000 abscissas and $m = 1601$, so instead of specifying these values at each distance for each material, these two values are used throughout.

Fig. 3.8 describes the time-domain Green's functions scaled by $4\pi r$ calculated with the Pantis method at $r = 1$ cm with different numbers of Filon abscissas and values of

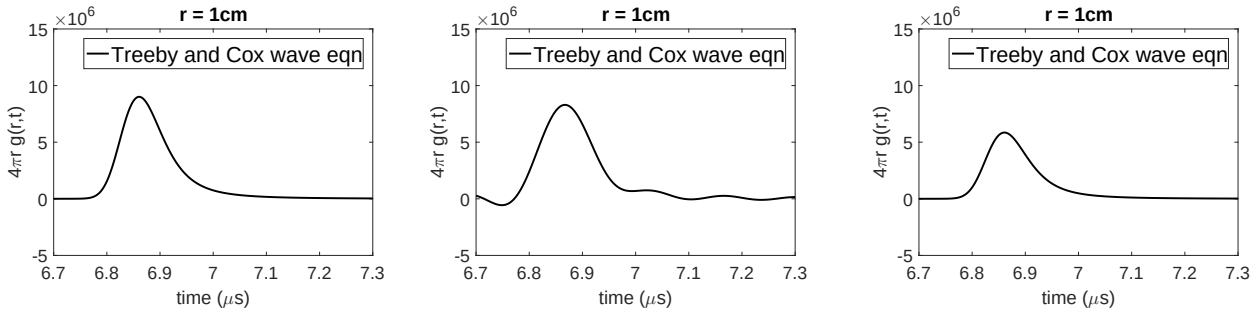

Figure 3.8: Computed time-domain Green's function scaled by $4\pi r$ evaluated for breast at $r = 1$ cm computed with the Pantis method using (a) 2,000 Filon abscissas and $m = 401$, (b) 2,000 Filon abscissas and $m = 101$, and (c) 500 Filon abscissas and $m = 401$.

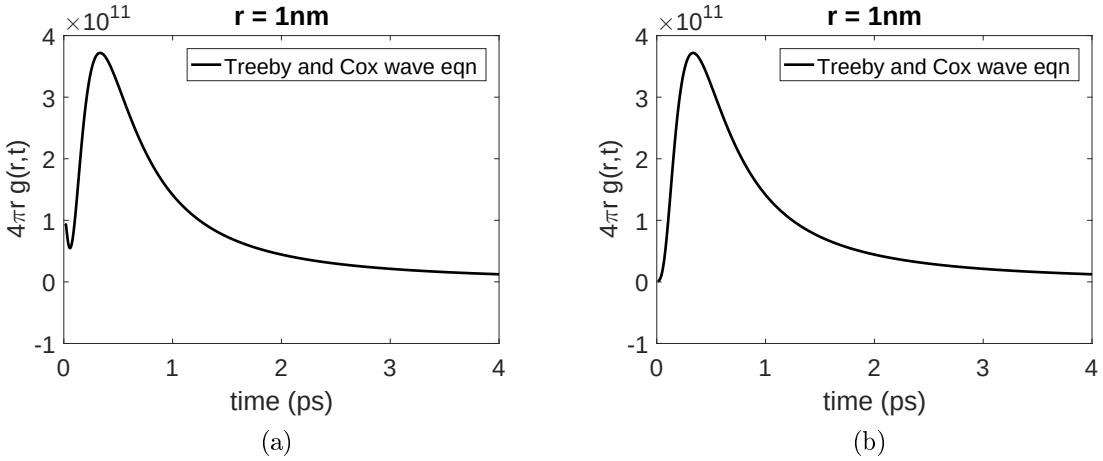

Figure 3.9: Computed time-domain Green's functions scaled by $4\pi r$ evaluated for breast at $r = 1$ nm using 500 Filon abscissas and $m = 5$ (a) without and (b) with the Pantis term.

m. A comparison between Figs. 3.8(a) and 3.8(b) indicates that when m is too small, artificial oscillations appear in the computed Green's function. This problem is addressed by increasing the value of m. Also, a comparison between Figs. 3.8(a) and 3.8(c) shows that when the number of abscissas is insufficient, the amplitude of the waveform is diminished by a significant amount relative to the correct result for the computed time-domain Green's function.

Fig. 3.9 shows the time-domain Green's functions scaled by $4\pi r$ calculated before (a) and after (b) the Pantis method is applied at $r = 1$ nm with 500 Filon abscissas and $m = 5$.

These two waveforms match closely for larger values of t. As indicated in Fig. 3.9, the contribution from $I_2(r,t)$ is particularly important at shorter distances, especially when t is close to 0. For $t \leq 0.5$ ps at $r = 1$ nm in breast, the contribution from $I_2(r,t)$ is larger than 1% of the peak value of the time-domain Green's function. If the $I_2(r,t)$ term is omitted and only the contribution from $I_1(r,t)$ calculated with the Filon's formula is included, artificial oscillations appear in the computed Green's function for small values of t.

3.6.2 Improved approximations for the attenuation and phase velocity

Figs. 3.1 and 3.2 show that the attenuation of the Chen-Holm wave equation is accurately represented by a power law and that the attenuation of the Treeby-Cox wave equation is very close to a power law. Figs. 3.1 and 3.2 also show that a more accurate representation for the attenuation of the Treeby-Cox wave equation is achieved when the second term in Eq. 3.15 is included. In addition, Figs. 3.1 and 3.2 demonstrate that more accurate representation for the phase velocities of the Chen-Holm and Treeby-Cox wave equations are obtained when a second (Chen-Holm) or a third (Treeby-Cox) term is included in the expression for $c(\omega)$. The similarities and differences between these phase velocities are further reinforced when binomial approximations are evaluated for each expression. For instance, the phase velocity obtained from the binomial approximation to Eq. 3.7 is $c(\omega) \approx c_0 + (y - 1/2)\,\alpha_0^2 c_0^3 \omega^{2y-2}$ for the Chen-Holm wave equation when $\omega \ll [(y - 1/2)\,\alpha_0^2 c_0^2]^{-1/(2y-2)}$, which yields $c(\omega) \approx 1450 + 9.0899 \times 10^{-10}\omega$ when $\omega \ll 1.5952 \times 10^{12}$ radians/second (or $f \ll 2.5388 \times 10^{11}$ Hz) for breast. Thus, $c(\omega)$ increases linearly as a function of frequency when the Chen-Holm wave equation is evaluated for breast, as indicated in Fig. 3.1(a). In Fig. 3.1(c), the phase velocity of the Chen-Holm wave equation is approximately $c(\omega) \approx 1540 + 1.6049 \times 10^{-5}\omega^{0.278}$, which holds when $\omega \ll 5.1587 \times 10^{28}$ radians/second (or $f \ll 8.2103 \times 10^{27}$ Hz) for liver. When plotted on the same axes, the results obtained from these approximations are indistinguishable from Eq. 3.7 and are therefore not

shown. When the binomial approximation is applied to Eq. 3.14, this yields $c(\omega) \approx c_0 - \tan(\pi y/2)\,\alpha_0 c_0^2 \omega^{y-1} + [\tan^2(\pi y/2) - (-y + 1/2 + (y+1/2)\tan^2(\pi y/2))]\,\alpha_0^2 c_0^3 \omega^{2y-2}$ for the Treeby-Cox wave equation when $\omega \ll [|\tan(\pi y/2)|\,\alpha_0 c_0]^{-1/(y-1)}$, and similarly, the binomial approximation applied to the phase velocity for the power law wave equation in Eq. 2.2 yields $c(\omega) \approx c_0 - \tan(\pi y/2)\,\alpha_0 c_0^2 \omega^{y-1} + \tan^2(\pi y/2)\,\alpha_0^2 c_0^3 \omega^{2y-2}$ when the angular frequency satisfies $\omega \ll [|\tan(\pi y/2)|\,\alpha_0 c_0]^{-1/(y-1)}$. In Fig. 3.2(a), the frequency-dependent phase velocities of both the Treeby-Cox wave equation and the power law wave equation for breast are represented by the approximate expressions $c(\omega) \approx 1450 + 1.1481 \times 10^{-3}\omega^{0.5} - 4.0367 \times 10^{-25}\omega$ for the Treeby-Cox wave equation and $c(\omega) \approx 1450 + 1.1481 \times 10^{-3}\omega^{0.5} + 9.0899 \times 10^{-10}\omega$ for the power law wave equation, which hold when $\omega \ll 1.5952 \times 10^{12}$ radians/second (or $f \ll 2.5388 \times 10^{11}$ Hz). In Fig. 3.2(c), the phase velocities of the Treeby-Cox wave equation and the power law wave equation for liver are represented by the approximate expressions $c(\omega) \approx 1540 + 0.8864\omega^{0.139} - 3.0994 \times 10^{-4}\omega^{0.278}$ for the Treeby-Cox wave equation and $c(\omega) \approx 1540 + 0.8864\omega^{0.139} + 5.1016 \times 10^{-4}\omega^{0.278}$ for the power law wave equation, respectively, when $\omega \ll 2.0356 \times 10^{23}$ radians/second (or $f \ll 3.2398 \times 10^{22}$ Hz). When plotted on the same axes, the results obtained from these two approximations for $c(\omega)$ are also indistinguishable from Eq. 3.14 and are therefore not shown. The first two terms in these two binomial expressions for the phase velocity of the Treeby-Cox and power law wave equations are the same, and the first term in the expression for the attenuation of the Treeby-Cox wave equation in Eq. 3.15 is also the same as that for the power law wave equation. Thus, although Figs. 3.1 and 3.2 indicate that there is a small but noticeable difference in $\alpha(\omega)$ and $c(\omega)$ for the Treeby-Cox and power law wave equations over the frequency range from 0.1 to 40 MHz, much closer agreement in $\alpha(\omega)$ and $c(\omega)$ for the Treeby-Cox and power law wave equations is expected for smaller values of ω. Furthermore, the first terms in the series expansions for both the attenuation and the phase velocity are the same for all three of these fractional wave equations. However, the second term in the binomial approximation for the phase velocity $c(\omega)$ of the Chen-Holm wave equation is quite different from the second terms in

the binomial approximations for the other two fractional wave equations, where these terms are responsible for the significant differences between the phase velocities shown in Fig. 3.1 and Fig. 3.2.

3.6.3 Time-domain Green's functions

Figs. 3.3 and 3.4 show several examples of time-domain Green's functions for the Chen-Holm and Treeby-Cox fractional wave equations, which are causal for all values of the power law exponent $1 < y \leq 2$. Figs. 3.3 and 3.4 also show that the time-domain Green's function for the power law wave equation is noncausal for $1 < y \leq 2$, which is only evident in the time-domain at very short distances. At longer distances, Figs. 3.3 and 3.4 suggest that the time-domain Green's functions for the Treeby-Cox wave equation and the power law wave equation converge to the same result. Figs. 3.3 and 3.4 also show that amplitudes are similar for all three Green's functions in each subfigure. The amplitudes for all three of these Green's functions are proportional to the scale factor $(\alpha_0 r)^{-1/y}$, which was also demonstrated for the three time-fractional wave equations evaluated in Zhao and McGough [53]. The peak values are all about the same for each subplot in Figs. 3.3 and 3.4, which is confirmed by the results in Figs. 3.5(a) and 3.5(c) showing the amplitudes calculated for the time-domain Green's functions of all three fractional wave equations. Figs. 3.5(a) and 3.5(c) therefore demonstrate that the attenuations are all about the same for all three of these fractional wave equations, which is expected since the attenuations of all three fractional wave equations either exactly or approximately follow the power law described by Eq. 2.1. Figs. 3.3 and 3.4 indicate that three distinct peaks are observed in the time-domain Green's functions at shorter distances, and then the peak locations for the time-domain Green's functions of the power law wave equation and the Treeby-Cox wave equation converge at larger distances. In Figs. 3.3 and 3.4, temporal spreading is observed in all three waveforms. The amount of temporal spreading is also determined by $(\alpha_0 r)^{1/y}$, which appears in the denominator of the argument for the stable distribution in Eq. 2.13. The temporal spreading is also about the same for all three of these fractional wave equations, as shown in Figs. 3.5(b) and 3.5(d).

These plots, which describe the FWHMs of the three fractional wave equations, all match very closely. Thus, the amplitude peaks, the temporal spreading, and the first terms in the series expansions for $\alpha(\omega)$ and $c(\omega)$ are nearly the same for all three of these fractional wave equations, but the remaining terms in the expressions for the phase velocity $c(\omega)$ of the Chen-Holm wave equation are distinct from the corresponding terms in the expressions for the phase velocities of the other two fractional wave equations. This suggests that the attenuation $\alpha(\omega)$ is primarily responsible for both the decay in the peak values and the temporal waveform spreading in these three fractional wave equations. The phase velocity $c(\omega)$, particularly the first non-constant term in the binomial approximation for $c(\omega)$, is responsible for the 'skew' or symmetry/asymmetry of the time-domain Green's functions shown in Figs. 3.3 and 3.4.

3.6.4 Dispersion

The Chen-Holm wave equation is 'dispersionless' in the sense that the phase velocity $c(\omega)$ is nearly equal to a constant, which yields the symmetric time-domain Green's functions depicted in Figs. 3.3 and 3.4, where the axis of symmetry is defined as $t = r/c$ in each subplot. Two other examples of 'dispersionless' wave equations are the Stokes and Blackstock wave equations. Both of these also have nearly constant phase velocity $c(\omega)$, and the time-domain Green's functions for both of these in the far field are approximately represented by Gaussian functions that are centered at $t = r/c$. When $y = 2$ in the power law wave equation, Eq. 2.2 reduces to $c(\omega) = c_0$, which is also dispersionless. Also, the time-domain Green's function for the power law wave equation with $y = 2$ is a Gaussian centered at $t = r/c$. Thus, these four examples of 'dispersionless' lossy wave equations all possess exactly or approximately symmetric time-domain Green's functions.

In acoustics and medical ultrasound, the term 'dispersion' has two different meanings. In some contexts, the dispersion refers to the temporal spreading, and in others, the dispersion describes the frequency-dependent phase velocity $c(\omega)$. However, the contribution from the attenuation $\alpha(\omega)$, not the phase velocity, is responsible for the waveform spreading in

all three of these fractional wave equations. Thus, these two meanings for the dispersion interestingly refer to two completely different aspects of ultrasound propagation in soft tissue. In particular, the Chen-Holm wave equation, which is dispersionless in the sense that $c(\omega)$ is nearly constant, demonstrates a considerable amount of waveform spreading as the propagation distance increases in the time-domain Green's functions shown in Figs. 3.3 and 3.4 and in the FWHM values shown in Figs. 3.5(b) and 3.5(d). This is in contrast to the Treeby-Cox and power law wave equations, which are also dispersive in the sense that the phase velocity $c(\omega)$ varies with frequency. However, all three of these fractional wave equations have approximately the same amount of dispersion in terms of the FWHM values shown in Figs. 3.5(b) and 3.5(d).

3.6.5 Convolving time-domain Green's functions with short pulses

Figs. 3.6 and 3.7 describe the waveforms obtained when a three cycle Hanning-weighted pulse is convolved with the time-domain Green's functions for the three fractional wave equations evaluated in breast and liver. Although Figs. 3.1 and 3.2 indicate that there is a slight difference in the phase velocity for the Treeby-Cox and the power law wave equations at 7.5 MHz and 29 MHz, the time-domain Green's functions for the Treeby-Cox and the power law wave equations are nearly identical in Figs. 3.3(g) and 3.4(g) at $r = 1$ cm, so the results obtained in Figs. 3.6 and 3.7 with the Treeby-Cox and power law wave equation are less sensitive to the differences in the attenuation, which are filtered out after propagating 1 cm. Also, the first two terms in the binomial expansions for the phase velocities of the Treeby-Cox and the power law wave equations are identical. These observations, along with the results shown in Figs. 3.3 and 3.4, suggest that the Treeby-Cox and the power law wave equations exhibit very similar behaviors at distances $r \geq 100\,\mu$m, but at very short distances and for very high frequency excitations, some differences are observed. In addition, the differences between the time-domain Green's function for the Chen-Holm wave equation and the time-domain Green's functions for the other two wave equations shown in Figs. 3.3(g)

and 3.4(g) are also reflected in Figs. 3.6 and 3.7, which is reflected in the differences in the phase velocities.

3.6.6 Comparisons with time-domain Green's functions calculated with 3D FFTs

Time-domain Green's functions are also calculated with 3D fast Fourier transforms (FFTs) using the approach described in Treeby and Cox [61] and compared to the Green's functions results computed with the Pantis method shown in Figs. 3.3 and 3.4. Although the analytical expressions evaluated with each approach are similar, the numerical performance of these two methods is quite different. For example, a single calculation with the Pantis method was completed in 35 seconds on a Microsoft Surface Pro with an Intel Core m3-6Y30 CPU @ 0.90 GHz, whereas the calculation using the same parameters with 3D FFTs required compute servers (Dual Intel Xeon E5-26xx @ 2.3 GHz, 2.4 GHz, and 2.7 GHz) with 48-88 cores and 384-768 GB RAM, which took anywhere between 15 minutes and a few hours depending on a variety of factors including the number of processors available and memory/CPU usage of other jobs running on the compute servers. The calculations with the Pantis method were performed serially, whereas the calculations with 3D FFTs were performed in parallel using 'parfor' calculations in Matlab using up to 36 'workers.' Reasonably accurate results were obtained when calculations with 3D FFTs were performed with 512 x 512 x 512 spatial points (i.e., 512 points in each direction). When 3D FFTs with more points were evaluated (only radix 2 FFTs were considered here), Matlab either crashed or ran out of memory, and when 3D FFTs with fewer points were evaluated, the computed result usually demonstrated severe nonphysical oscillations or other undesirable numerical artifacts.

We also found that time-domain Green's function calculations with 3D FFTs are very sensitive to the grid spacing. For instance, Gibbs oscillations (which often include nonphysical negative values for the time-domain Green's function) were commonly observed in the results

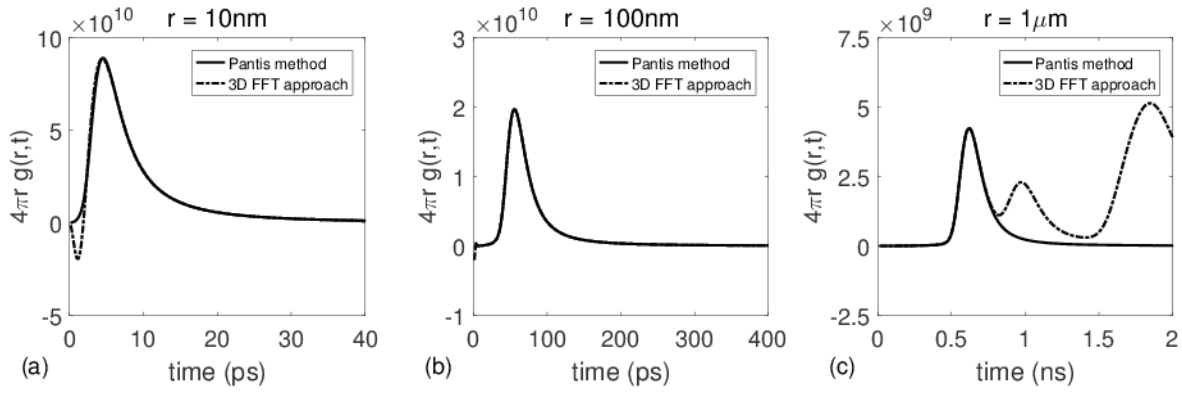

Figure 3.10: Time-domain Green's functions scaled by $4\pi r$ calculated for breast with $y = 1.5$, $\alpha_0 = 0.086$ Np/cm/MHz$^{1.5}$, and $c_0 = 1450$ m/s evaluated at (a) $r = 10$ nm, (b) $r = 100$ nm, and (c) $r = 1\,\mu$m with the Pantis method (solid line) and the 3D FFT approach (dot-dashed line) using $dx = dy = dz = 0.5$ nm in (a), (b), and (c).

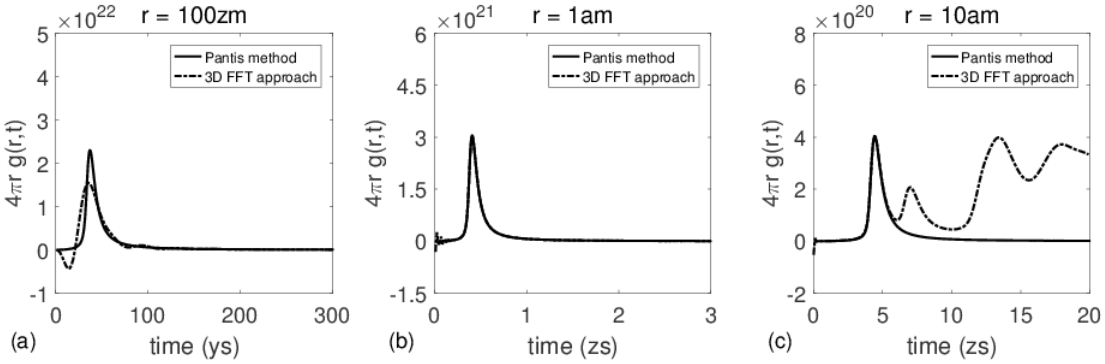

Figure 3.11: Time-domain Green's functions scaled by $4\pi r$ calculated for liver with $y = 1.139$, $\alpha_0 = 0.0459$ Np/cm/MHz$^{1.139}$, and $c_0 = 1540$ m/s evaluated at (a) $r = 100$ zm, (b) $r = 1$ am, and (c) $r = 10$ am with the Pantis method (solid line) and 3D FFT approach (dot-dashed line) using $dx = dy = dz = 50$ zm in (a), (b), and (c).

obtained with 3D FFTs. These oscillations were reduced by decreasing the spacing between adjacent points in the computational grid (i.e., by decreasing dx, dy, and dz). However, if the grid spacing is too small in calculations with 3D FFTs, then this causes problems with frequency-domain aliasing, which introduces errors in the 'heavy tail' of the time-domain Green's function. If the grid spacing is too small by a small amount, then a small to moderate offset from the correct value is observed in the 'tail'. If the grid spacing is too small by a larger amount, the 'tail' grows with increasing time instead of slowly decaying to zero as shown in Figs. 3.3 and 3.4. In extreme cases, when the value of the grid spacing is much too

large, most if not all values in the computed time-domain Green's function are much larger than the correct values. Usually, Gibbs oscillations or errors in the 'heavy tail' or both are observed in time-domain Green's function calculations with 3D FFTs, although we were often able to manually select appropriate parameters that achieve a reasonable trade-off between these two types of numerical artifacts for the results shown in Figs. 3.3(a-h) and 3.4(a-d). Examples of typical results obtained after some parameter tuning are shown in Fig. 3.10(b) and 3.11(b), which contain Gibbs oscillations at the very beginning and good agreement with the Pantis results elsewhere. Interestingly, when the grid spacing is selected to reduce both types of numerical artifacts for one value of r, the time-domain Green's function calculated with 3D FFTs in other locations (e.g., $r/10$ and $10r$) consistently yield significant errors. This effect is shown in Fig. 3.10 with three different time-domain Green's functions calculated with 3D FFTs evaluated for breast at $r = 10$ nm, $r = 100$ nm, and $r = 1\,\mu$m with the same value for the grid spacing, namely $dx = dy = dz = 0.5$ nm. Fig. 3.10(b) (center panel) shows some Gibbs oscillations in the result computed with 3D FFTs near $t = 0$ and also good agreement in the heavy tail. In Fig. 3.10(a) (left panel), the grid spacing is too large. When the grid spacing is reduced to $dx = dy = dz = 0.2$ nm or $dx = dy = dz = 0.1$ nm in Fig. 3.10(a) (assuming that the number of spatial points is fixed and equal to 512 x 512 x 512), the agreement is much better (not shown), although some small Gibbs oscillations still remain in the result obtained with 3D FFTs near $t = 0$. In Fig. 3.10(c) (right panel), errors in the heavy tail are produced by frequency-domain aliasing. The errors in Fig. 3.10(c) are alleviated by increasing the grid spacing to approximately 5 nm, which also introduces a small amount of ringing at time $t = 0$. Similar results are also observed in Green's function calculations evaluated for liver at $r = 100$ zm, $r = 1$ am, and $r = 10$ am, which are shown in Fig. 3.11. Although time-domain Green's functions calculated with 3D FFTs produce a

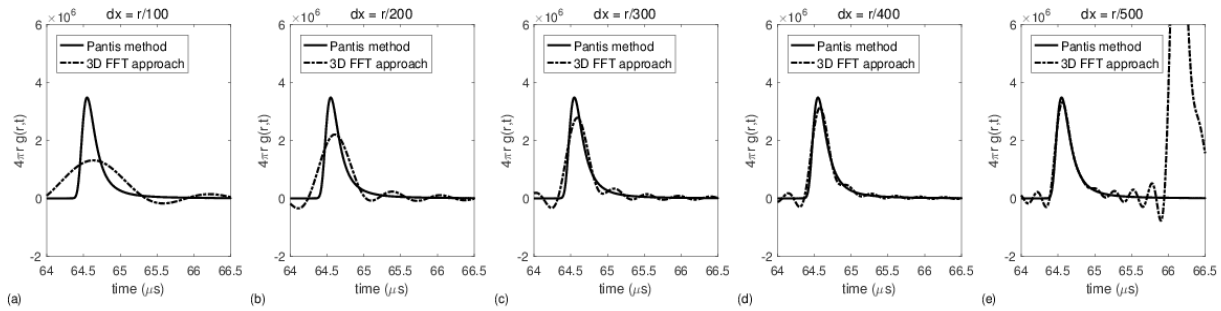

Figure 3.12: Time-domain Green's functions scaled by $4\pi r$ calculated for liver with $y = 1.139$, $\alpha_0 = 0.0459$ Np/cm/MHz$^{1.139}$, and $c_0 = 1540$ m/s evaluated at $r = 10$ cm with the Pantis method (solid line) and with 3D FFTs (dot-dashed line) using (a) $dx = r/100$, (b) $dx = r/200$, (c) $dx = r/300$, (d) $dx = r/400$, and (e) $dx = r/500$. In all simulations with 3D FFTs evaluated here, $dx = dy = dz$.

large grid of values, the results are only accurate in certain locations where the grid spacing is selected to avoid problems with Gibbs oscillations and with frequency-domain aliasing.

We also found that the time-domain Green's function calculations with 3D FFTs failed to converge for the results shown in Figs. 3.4(e-h). This is demonstrated in Fig. 3.12 using a time-domain Green's function calculated with 3D FFTs evaluated for liver at r = 10 cm with grid spacings ($dx = dy = dz$) of 1 mm, 500 μm, 333 μm, 250 μm, and 200 μm. The same types of problems are also observed for $r = 100\,\mu$m, $r = 1$ mm, and $r = 1$ cm. Thus, the Pantis method is also useful for determining which parameter combinations yield reasonable results in time-domain Green's function calculations with 3D FFTs.

3.7 Conclusion

Phase velocities and attenuation values were evaluated over a range of ultrasound frequencies, and time-domain Green's functions were calculated for the Chen-Holm, Treeby-Cox, and power law wave equations in breast and liver. In addition, the amplitudes and FWHM values of the time-domain Green's functions for these three fractional wave equations were calculated, and three-cycle Hanning-weighted pulses at two different center frequencies were convolved with the time-domain Green's functions for three fractional wave equations. An additional term was derived for the power series that describes $c(\omega)$ for the Chen-Holm

wave equation and additional terms were derived for the power series that describe $c(\omega)$ and $\alpha(\omega)$ for the Treeby-Cox wave equation, where these new power series more closely match the results obtained by numerically evaluating the dispersion relation than the previous approximations. Causality was also demonstrated analytically in the time domain for both the Chen-Holm and Treeby-Cox wave equations. The Pantis method was introduced as an effective approach for evaluating the highly oscillatory improper integrals that arise in numerical calculations of the time-domain Green's functions for the Chen-Holm and Treeby-Cox space-fractional wave equations. The time-domain Green's functions for all three time-domain Green's functions show a similar amount of temporal spreading and amplitude reduction, but the time-domain Green's functions for the Treeby-Cox and power law wave equations are skewed whereas the time-domain Green's function for the Chen-Holm wave equation is symmetric. The Chen-Holm space-fractional wave equation is non-dispersive in the sense that the phase velocity is nearly constant, but the Chen-Holm wave equation is also dispersive in the sense that waveform spreading is clearly evident in the computed time-domain Green's functions. The Treeby-Cox wave equation is dispersive in the sense that the phase velocity is non-constant and also in the sense that waveform spreading is clearly evident in the computed time-domain Green's functions. The Chen-Holm and Treeby-Cox space-fractional wave equations demonstrate approximately the same amount of attenuation and waveform spreading, but the phase velocities, time-domain Green's functions, and convolution results obtained with these time-domain Green's functions all differ significantly. Also, although the attenuation and phase velocity for the Treeby-Cox and power law wave equation differ slightly, the time-domain Green's functions and the convolution results obtained with the Green's functions for these two fractional wave equations converge to the same result.

Chapter 4

Perfectly matched layers for nonlinear ultrasound simulations with the KZK equation

4.1 Introduction

High intensity pulses are often used in applications of therapeutic ultrasound. Linear assumptions do not always predict the correct results in these cases. The attenuation and diffraction are also important in models of nonlinear ultrasound propagation. Thus, a model combining diffraction, attenuation, and nonlinearity is needed to analyze the propagation of ultrasonic waves.

The Khokhlov-Zabolotskaya-Kuznetsov (KZK) equation [62, 63] is a parabolic approximation to the Westervelt equation. Lee and Hamilton [17] propose an operator-splitting based numerical algorithm to solve the transient KZK equation numerically in the time domain, using a circular or spherically focused traducer. Cleveland [18] expands the application of this model by including the effect of relaxation. An approach for simulating nonlinear continuous wave (CW) pressure fields with the KZK equation is presented by Berntsen [19]. The validation of the KZK equation for axisymmetric ultrasound beams is evaluated by Soneson [64]. Curra and Filonenko [65, 66] numerically calculate solutions for the CW KZK equation to model heat deposition in biological tissue. Huijssen [67] compares the Iterative

Nonlinear Contrast Source (INCS) method with the KZK model for the computation of nonlinear, wide-angle, pulsed acoustic fields.

Attempts to calculate solutions to the KZK equation with finite difference simulations, however, are limited by the implementation of the boundary conditions. Since there is no absorbing boundary layer implemented in the KZK models of Berntsen [19] or Lee [17], large grids are needed for these calculations. In electromagnetics, this problem is addressed with absorbing boundary conditions or perfectly matched layers. For example, Mur [68] proposes an accurate absorbing boundary condition for both 2D and 3D time-domain electromagnetic-field equations. Berenger [69] introduces a perfectly matched layer (PML) for finite difference time domain (FDTD) simulations of electromagnetic waves, which is validated by Katz [70] in the 2D case and then extended to the 3D case. The PML is applied to acoustic models with different coordinate systems by Yuan and Liu [71, 72, 73]. Abarbanel and Hu [74, 75] have developed PML equations for 2D linearized Euler equations. Sheu [76] applies a PML to a photoacoustics model in axisymmetric cylindrical coordinates. Based on first-order auxiliary differential equations, Ma [77] proposes an unsplit PML for a second-order acoustic wave equation in 3D Cartesian coordinates. Ehrlich [78] combines the acoustic wave propagator and a PML to model acoustic propagation in the time domain. Pinton [79] implements a PML for a 3D nonlinear attenuating full-wave model in the time domain. Research on 3D acoustic scattering problems has also been performed in both the time and frequency domains by Kaltenbacher [80], Chen [81], Alles [82], and Katsibas [83]. Duru [84] also uses a PML in a 2D scalar wave equation for heterogeneous and layered media.

In the following section, a perfectly matched layer implemented through terms from the power law wave equation with $y = 0$ and $y = 2$ is derived for the transient and CW KZK equations. Artificial attenuation is introduced to reduce reflections from the radial boundary. Numerical validations are demonstrated for both linear and nonlinear media. With these new PML implementations, the size of the computational grid is reduced, which accelerates numerical solutions of the KZK equation.

4.2 Theory

4.2.1 The 2D wave equation with power law attenuation

The linear lossless wave equation in a two-dimensional cylindrical coordinate system is expressed as

$$\frac{\partial^2 p}{\partial t^2} = c_0^2 \left(\frac{\partial^2 p}{\partial z^2} + \frac{1}{r} \frac{\partial}{\partial r} \left(r \frac{\partial p}{\partial r} \right) \right). \tag{4.1}$$

When the effect of attenuation is introduced through the power law wave equation, the wave equation in 2D cylindrical coordinates becomes

$$\left(\frac{\partial^2 p}{\partial z^2} + \frac{1}{r} \frac{\partial}{\partial r} \left(r \frac{\partial p}{\partial r} \right) \right) - \frac{1}{c_0^2} \frac{\partial^2 p}{\partial t^2} - \frac{2\alpha_0}{c_0 \cos\left(\pi y/2\right)} \frac{\partial^{y+1} p}{\partial t^{y+1}} - \frac{\alpha_0^2}{\cos^2\left(\pi y/2\right)} \frac{\partial^{2y} p}{\partial t^{2y}} = 0. \tag{4.2}$$

For power law exponents $y = 0$ and $y = 2$, the power law wave equation in Eq. 4.2 is expressed as

$$\frac{\partial^2 p}{\partial t^2} = c_0^2 \left(\frac{\partial^2 p}{\partial z^2} + \frac{1}{r} \frac{\partial}{\partial r} \left(r \frac{\partial p}{\partial r} \right) \right) - 2\alpha_0 c_0 \frac{\partial p}{\partial t} - \alpha_0^2 c_0^2 p \quad y = 0, \tag{4.3}$$

and

$$\frac{\partial^2 p}{\partial t^2} = c_0^2 \left(\frac{\partial^2 p}{\partial z^2} + \frac{1}{r} \frac{\partial}{\partial r} \left(r \frac{\partial p}{\partial r} \right) \right) + 2\alpha_0 c_0 \frac{\partial^3 p}{\partial t^3} - \alpha_0^2 c_0^2 \frac{\partial^4 p}{\partial t^4} \quad y = 2. \tag{4.4}$$

4.2.2 Coordinate stretching

The analytical expressions that describe perfectly matched layers are often derived from an augmented model for the gradient that stretches each coordinate according to

$$\nabla = \hat{x} \frac{1}{s_x} \frac{\partial}{\partial x} + \hat{y} \frac{1}{s_y} \frac{\partial}{\partial y} + \hat{z} \frac{1}{s_z} \frac{\partial}{\partial z}, \tag{4.5}$$

where s_x, s_y, and s_z describe the effects of coordinate stretching in all three directions. In the x- direction, the coordinate stretching variable is defined as

$$s_x = \left(1 + \frac{\sigma(x)}{j\omega}\right), \tag{4.6}$$

and similar expressions are defined in the y- and z- directions. The lossless Helmholtz equation in axisymmetric cylindrical coordinates is expressed as

$$\frac{1}{r}\frac{\partial}{\partial r}\left(r\frac{\partial P}{\partial r}\right) + \frac{\partial^2 P}{\partial z^2} + k^2 P = 0, \tag{4.7}$$

where the wavenumber is $k = \frac{\omega}{c_0}$ and P is the pressure field. Applying coordinate stretching to Eq. 4.7 in both the radial and axial directions,

$$\frac{\partial}{\partial r} \rightarrow \frac{1}{\left(1 + \frac{\sigma_r(r)}{j\omega}\right)}\frac{\partial}{\partial r}, \quad \frac{1}{r} \rightarrow \frac{1}{\left(1 + \frac{\sigma_r(r)}{j\omega}\right)}\frac{1}{r}, \quad \frac{\partial}{\partial z} \rightarrow \frac{1}{\left(1 + \frac{\sigma_z(z)}{j\omega}\right)}\frac{\partial}{\partial z}, \tag{4.8}$$

yields

$$\frac{1}{\left(1 + \frac{\sigma_r(r)}{j\omega}\right)^2}\left(\frac{1}{r}\frac{\partial P}{\partial r} + \frac{\partial^2 P}{\partial r^2}\right) + \frac{1}{\left(1 + \frac{\sigma_z(z)}{j\omega}\right)^2}\frac{\partial^2 P}{\partial z^2} + k^2 P = 0, \tag{4.9}$$

which becomes

$$\begin{aligned}\left(1 + \tfrac{\sigma_z(z)}{j\omega}\right)^2\left(\tfrac{1}{r}\tfrac{\partial P}{\partial r} + \tfrac{\partial^2 P}{\partial r^2}\right) + \left(1 + \tfrac{\sigma_r(r)}{j\omega}\right)^2\tfrac{\partial^2 P}{\partial z^2} \\ + \left(1 + \tfrac{\sigma_r(r)}{j\omega}\right)^2\left(1 + \tfrac{\sigma_z(z)}{j\omega}\right)^2 k^2 P = 0\end{aligned} \tag{4.10}$$

after each term is multiplied by $\left(1 + \frac{\sigma_z(z)}{j\omega}\right)^2\left(1 + \frac{\sigma_r(r)}{j\omega}\right)^2$. Multiplying Eq. 4.10 by $(j\omega)^2$ and inverse Fourier transforming in time, the result is the lossy time-domain wave equation

$$\begin{aligned}\left(\tfrac{\partial}{\partial t} + \sigma_z(z)\right)^2\left(\tfrac{1}{r}\tfrac{\partial p}{\partial r} + \tfrac{\partial^2 p}{\partial r^2}\right) + \left(\tfrac{\partial}{\partial t} + \sigma_r(r)\right)^2\tfrac{\partial^2 p}{\partial z^2} \\ - \left(\tfrac{\partial}{\partial t} + \sigma_r(r)\right)^2\left(\tfrac{\partial}{\partial t} + \sigma_z(z)\right)^2\tfrac{1}{c_0^2}p = 0,\end{aligned} \tag{4.11}$$

which attenuates wave propagation in the radial and axial directions.

4.2.3 The KZK equation

The Westervelt equation is a full wave nonlinear model that combines the effects of diffraction, attenuation, and nonlinearity

$$\nabla^2 p - \frac{1}{c_0^2}\frac{\partial^2 p}{\partial^2 t} + \frac{2\alpha_0}{c_0}\frac{\partial^3 p}{\partial t^3} + \frac{\beta}{\rho_0 c_0^4}\frac{\partial^2 p^2}{\partial t^2} = 0. \tag{4.12}$$

After applying a parabolic approximation and a change of variables, Eq. 4.12 reduces to the KZK equation, which is defined in cylindrical coordinates (r, z) as

$$\frac{\partial^2 p}{\partial z \partial \tau} = \frac{c_0}{2}\nabla_\perp^2 p + \alpha_0 \frac{\partial^3 p}{\partial \tau^3} + \frac{\beta}{2\rho_0 c_0^3}\frac{\partial^2 p^2}{\partial \tau^2}, \tag{4.13}$$

where p is the pressure, c_0 is the sound speed, ρ_0 is the density, α_0 is the attenuation constant, and β is the nonlinearity parameter. The propagation direction of the sound beam is aligned with the z-axis, and $\nabla_\perp^2 = \frac{\partial^2}{\partial r^2} + \frac{1}{r}\frac{\partial}{\partial r}$ is the radial component of the Laplacian operator in cylindrical coordinates. A detailed derivation of the KZK wave equation is given in Appendix A. Due to axial symmetry, the spatial variables for the KZK equation are (r, z) in the cylindrical coordinate system. On the right-hand side of Eq. 4.13, the three terms from left to right represent the effects of diffraction, attenuation, and nonlinearity. Similar to the Westervelt equation, there is no analytical solution for the KZK equation. Thus, the KZK model is evaluated numerically. Although the KZK equation is only valid in the far field of the paraxial region, this model is still commonly applied to simulations of medical ultrasound due to the computational advantages of the parabolic approximation. As developed by Lee and Hamilton [17] and implemented in the KZK Texas code [17], the finite difference method numerically solves the transient KZK equation with operator splitting to separately account for these three effects at each step.

4.2.4 PML derivation for the KZK equation

Stretched coordinates for the nonlinear lossy KZK equation

Since waves propagate in the positive z direction but not in the negative z direction with the KZK model, there is no need for a PML in the axial direction. Eq. 4.13 in the frequency domain is given by

$$j\omega\frac{\partial P}{\partial z} = \frac{c_0}{2}\nabla_\perp^2 P + \alpha_0 (j\omega)^3 P + \frac{\beta}{2\rho_0 c_0^3}(j\omega)^2 P^2 \tag{4.14}$$

and when coordinate stretching is applied to the KZK equation for a PML in the radial direction, this yields

$$\begin{gathered} j\omega\frac{\partial P}{\partial z}\left(1+\frac{\sigma(r)}{j\omega}\right)^2 = \frac{c_0}{2}\left(\frac{\partial^2}{\partial r^2}+\frac{1}{r}\frac{\partial}{\partial r}\right)P + \\ \left(1+\frac{\sigma(r)}{j\omega}\right)^2 \alpha_0 (j\omega)^3 P + \left(1+\frac{\sigma(r)}{j\omega}\right)^2 \frac{\beta}{2\rho_0 c_0^3}(j\omega)^2 P^2. \end{gathered} \tag{4.15}$$

After expanding and inverse Fourier transforming with respect to time, the result is

$$\begin{gathered} \frac{\partial^2 p}{\partial z \partial \tau} + 2\sigma(r)\frac{\partial p}{\partial z} + \sigma(r)^2 \int_{-\infty}^{\tau} \frac{\partial p}{\partial z} d\tau' = \frac{c_0}{2}\left(\frac{\partial^2}{\partial r^2}+\frac{1}{r}\frac{\partial}{\partial r}\right)p \\ +\alpha_0\frac{\partial^3 p}{\partial \tau^3} + 2\sigma(r)\alpha_0\frac{\partial^2 p}{\partial \tau^2} + \alpha_0\sigma(r)^2\frac{\partial p}{\partial \tau} + \frac{\beta}{2\rho_0 c_0^3}\frac{\partial^2 p^2}{\partial \tau^2} + \frac{\sigma(r)\beta}{\rho_0 c_0^3}\frac{\partial p^2}{\partial \tau} + \frac{\sigma(r)^2\beta}{2\rho_0 c_0^3}p^2, \end{gathered} \tag{4.16}$$

which is a chanllenging to evaluate with finite difference calculations, in part due to the integral on the left-hand side.

Stretched coordinates for the lossless linear KZK equation

When only the contributions from the diffraction terms are considered, the lossless linear KZK equation is expressed in the frequency domain as

$$j\omega\frac{\partial P}{\partial z} = \frac{c_0}{2}\nabla_\perp^2 P. \tag{4.17}$$

If coordinate stretching for a PML is applied in the radial direction, Eq. 4.17 then becomes

$$j\omega\frac{\partial P}{\partial z}\left(1+\frac{\sigma\left(r\right)}{j\omega}\right)^{2}=\frac{c_{0}}{2}\left(\frac{\partial^{2}}{\partial r^{2}}+\frac{1}{r}\frac{\partial}{\partial r}\right)P. \tag{4.18}$$

After expanding and inverse Fourier transforming,

$$\frac{\partial^{2}p}{\partial z\partial\tau}+2\sigma\left(r\right)\frac{\partial p}{\partial z}+\sigma\left(r\right)^{2}\int_{-\infty}^{\tau}\frac{\partial p}{\partial z}d\tau'=\frac{c_{0}}{2}\left(\frac{\partial^{2}}{\partial r^{2}}+\frac{1}{r}\frac{\partial}{\partial r}\right)p, \tag{4.19}$$

which also contains an integral on the left-hand side.

Combining the power law equation with the KZK equation

When Eq. 4.6 is applied to the 1D wave equation,

$$\frac{\partial^{2}p}{\partial x^{2}}=\frac{1}{c_{0}^{2}}\frac{\partial^{2}p}{\partial t^{2}}+\frac{2\sigma\left(x\right)}{c_{0}^{2}}\frac{\partial p}{\partial t}+\frac{\sigma\left(x\right)^{2}}{c_{0}^{2}}p, \tag{4.20}$$

which, after substituting $\alpha_{PML}=c_{0}\,\sigma\left(x\right)$, is recognized as the 1D power law wave equation with $y=0$. This suggests that there is another possible approach for implementing a PML that utilizes the power law equation. The 3D power law wave equation for the $y=0$ case is expressed as

$$\nabla^{2}p=\frac{1}{c_{0}^{2}}\frac{\partial^{2}p}{\partial t^{2}}+\frac{2\alpha_{PML}}{c_{0}}\frac{\partial p}{\partial t}+\alpha_{PML}^{2}p. \tag{4.21}$$

After applying a parabolic approximation and a change of variables in an axisymmetric cylindrical coordinate system, Eq. 4.21 becomes

$$\frac{\partial^{2}p}{\partial z\partial\tau}=\frac{c_{0}}{2}\nabla_{\perp}^{2}p-\alpha_{PML}\frac{\partial p}{\partial\tau}-\frac{c_{0}}{2}\alpha_{PML}^{2}p. \tag{4.22}$$

Similarly, the 3D power law wave equation for the $y=2$ case is expressed as

$$\nabla^{2}p=\frac{1}{c_{0}^{2}}\frac{\partial^{2}p}{\partial t^{2}}-\frac{2\alpha_{PML}}{c_{0}}\frac{\partial^{3}p}{\partial t^{3}}+\alpha_{PML}^{2}\frac{\partial^{4}p}{\partial t^{4}}, \tag{4.23}$$

and the corresponding expression that is obtained from a parabolic approximation and a change of variables in an axisymmetric cylindrical coordinate system is

$$\frac{\partial^2 p}{\partial z \partial \tau} = \frac{c_0}{2}\nabla_\perp^2 p + \alpha_{PML}\frac{\partial^3 p}{\partial \tau^3} - \frac{c_0}{2}\alpha_{PML}^2\frac{\partial^4 p}{\partial \tau^4}. \tag{4.24}$$

Eqs. 4.22 and 4.24 provide two related yet different approaches for defining a perfectly matched layer for the transient KZK equation, where the distribution of α_{PML} values can vary spatially.

Using the power law wave equation with $y = 0$ (two terms) for the PML

Since the KZK equation is a one-way wave equation in the axial direction, a PML is only needed in the radial direction. This suggests that stretched coordinates are not required for the derivation of the PML and that the power law wave equation with $y = 0$ or $y = 2$ in the radial direction provide effective expressions for PMLs. This indicates that the stretched coordinate system is not central to the derivation of an effective PML. The power law wave equation is all that is required, combined with the concept introduced by Berenger [69] that the PML should be several cells thick with a slowly varying lossy impedance that attenuates the incident wave with minimal reflections. By applying $\frac{1}{c_0}\frac{\partial}{\partial t} \rightarrow \frac{1}{c_0}\frac{\partial}{\partial t} + \alpha_{PML}$ to the wave equation in the time domain and utilizing the parabolic approximation in retarded time, one such PML for the transient KZK equation is obtained from

$$\frac{\partial^2 p}{\partial z \partial \tau} = \frac{c_0}{2}\nabla_\perp^2 p - \alpha_{PML}\frac{\partial p}{\partial \tau} - \frac{c_0}{2}\alpha_{PML}^2 p \tag{4.25}$$

for $y = 0$. For numerical calculations, the expression in Eq. 4.25 is solved with the Thomas algorithm.

Using the Telegrapher's equation $y = 0$ (one term) for the PML

For the $y = 0$ case, the second term $\frac{c_0}{2}\alpha_{PML}^2 p$ can be neglected when the value of $\frac{c_0}{2}\alpha_{PML}^2$ is small. Thus, another expression that describes a PML for the transient KZK is given by

$$\frac{\partial^2 p}{\partial z \partial \tau} = \frac{c_0}{2}\nabla_\perp^2 p - \alpha_{PML}\frac{\partial p}{\partial \tau}, \tag{4.26}$$

which is the retarded time parabolic approximation to the 3D Telegrapher's equation.

Using the power law wave equation with $y = 2$ (two terms) for the PML

The key to an effective absorbing boundary layer appears to be independent of the stretched coordinate system and is much more strongly influenced by other factors such as the slowly increasing attenuation that minimizes reflections at the interface between any two adjacent cells in the computational grid. This motivates the construction of a third PML based on the retarded time parabolic approximation to the power law wave equation with $y = 2$, which is given by

$$\frac{\partial^2 p}{\partial z \partial \tau} = \frac{c_0}{2}\nabla_\perp^2 p + \alpha_{PML}\frac{\partial^3 p}{\partial \tau^3} - \frac{c_0}{2}\alpha_{PML}^2\frac{\partial^4 p}{\partial \tau^4}. \tag{4.27}$$

Numerically, the first term on the right hand side combined with the original attenuation term is solved with the Thomas algorithm. The addition of the second attenuation term requires a penta-diagonal matrix algorithm.

Using the Blackstock wave equation with $y = 2$ (one term) for the PML

Similar to the $y = 0$ case, the second attenuation term is negligible for small α_{PML} when $y = 2$, which enables a fourth PML that is very closely related to the KZK equation. This

PML evaluates a straightforward modification of the KZK equation,

$$\frac{\partial^2 p}{\partial z \partial \tau} = \frac{c_0}{2}\nabla_\perp^2 p + \alpha_{PML}\frac{\partial^3 p}{\partial \tau^3}, \tag{4.28}$$

which is the retarded time parabolic approximation to the Blackstock wave equation.

4.3 Methods

4.3.1 Error calculations

To validate these PMLs for the KZK equation, comparisons between simulations with and without PMLs that increase the radial boundary limit to avoid reflections are evaluated. The formula for calculating the difference between these two results is

$$D(r,z) = \frac{max|p(r,z) - p_{ref}(r,z)|}{max|p_{ref}|}, \tag{4.29}$$

where the denominator is the maximum value of the reference pressure evaluated at all spatial and temporal points, and the numerator is the maximum value of the difference between the reference and simulation results evaluated at one spatial point for all time points. The difference $D(r,z)$ is dependent on both radial and axial coordinates.

4.3.2 Finite difference calculations with the KZK equation

Numerical calculations with the KZK equation are often evaluated with the finite difference method. The pressure field is first discretized in both the radial and axial directions, after which finite difference calculations are evaluated layer-by-layer in the axial direction. Within each layer, the effects of diffraction, attenuation, and nonlinearity are calculated separately through operator splitting. For these calculations, two types of finite difference calculations are evaluated. For the first several iterations, the implicit backward Euler finite difference method (IBFD) is used, after which the Crank-Nicolson finite difference method (CNFD) is applied. Both of these methods are numerically stable, and the CNFD method

results in a smaller local truncation error than the IBFD method with the same step size. However, the CNFD method is sensitive to oscillations, which means that the computed result can contain spurious oscillations, especially in the region close to the edge of the transducer where there is a discontinuity in pressure amplitude. Thus, the IBFD method is applied as a low pass filter in this region. For these reasons, these two finite difference methods are combined for the numerical evaluations of the KZK equation.

For the transient KZK equation, three effects are calculated separately within one spatial step using operator splitting. Diffraction effects are modeled by

$$\frac{\partial p}{\partial z} = \int_{-\infty}^{\tau} \frac{c_0}{2} \left(\frac{\partial^2}{\partial r^2} + \frac{1}{r} \frac{\partial}{\partial r} \right) p d\tau', \tag{4.30}$$

which is obtained after the nonlinear and loss terms are neglected and the remaining terms are integrated on both sides. The indicies of the finite difference calculation in the temporal, radial, and axial directions are i, j, and k. Thus, finite difference approximations for Eq. 4.30 are defined as

$$\frac{\partial p}{\partial z} \rightarrow \frac{p^i_{j,k+1} - p^i_{j,k}}{(\triangle z)_k}, \quad \frac{1}{r}\frac{\partial p}{\partial r} \rightarrow \frac{p^i_{j+1,k+1} - p^i_{j-1,k+1}}{2j\,(\triangle r)^2}, \tag{4.31}$$

$$\frac{\partial^2 p}{\partial r^2} \rightarrow \frac{p^i_{j+1,k+1} - 2p^i_{j,k+1} + p^i_{j-1,k+1}}{(\triangle r)^2}, \tag{4.32}$$

$$\int_{\tau_{min}}^{\tau} f(\tau')d\tau' \rightarrow (\triangle\tau) \left[\sum_{m=1}^{i-1} f_m + \frac{1}{2}\left(f_0 + f_i\right) \right]. \tag{4.33}$$

When only the effect of attenuation is considered, Eq. 4.13 becomes

$$\frac{\partial p}{\partial z} = \alpha_0 \frac{\partial^2 p}{\partial \tau^2}. \tag{4.34}$$

Similarly, the finite difference approximations for Eq. 4.34 are defined as

$$\frac{\partial p}{\partial z} \rightarrow \frac{p^i_{j,k+1} - p^i_{j,k}}{(\triangle z)_k}, \quad \frac{\partial^2 p}{\partial \tau^2} \rightarrow \frac{p^{i+1}_{j,k+1} - 2p^i_{j,k+1} + p^{i-1}_{j,k+1}}{(\triangle\tau)^2}. \tag{4.35}$$

When only the nonlinear effect is considered, Eq. 4.13 reduces to

$$\frac{\partial p}{\partial z} = \frac{\beta}{\rho_0 c_0^3} p \frac{\partial p}{\partial \tau}. \tag{4.36}$$

As indicated by Lee and Hamilton [17], the solution to Eq. 4.36 is given by

$$p_{j,k+1}^i = \frac{p_{j,k}^i}{1 - \left[\left(p_{j,k}^{i+1} - p_{j,k}^i\right)/\triangle\tau\right]\beta\left(\triangle z\right)_k/\left(\rho_0 c_0^3\right)}, \quad p_{j,k}^i \geq 0 \tag{4.37}$$

and

$$p_{j,k+1}^i = \frac{p_{j,k}^i}{1 - \left[\left(p_{j,k}^i - p_{j,k}^{i-1}\right)/\triangle\tau\right]\beta\left(\triangle z\right)_k/\left(\rho_0 c_0^3\right)}, \quad p_{j,k}^i \leq 0. \tag{4.38}$$

For continuous wave propagation, the acoustic pressure is often described as series expansion of different harmonics

$$p\left(\tau, r, z\right) = \sum_{n=-N_{max}}^{N_{max}} C_n\left(r, z\right) e^{-jn2\pi f_0 \tau}, \tag{4.39}$$

where f_0 is the fundamental frequency, N_{max} is the total number of harmonics, and $C_n\left(r, z\right)$ is the complex amplitude of the n-th harmonic. When Eq. 4.39 is combined with the transient KZK equation, the amplitudes are expressed as

$$\begin{gathered}\frac{dC_n(r,z)}{dz} = j\frac{c_0}{4\pi n f_0}\left(\frac{\partial^2 C_n(r,z)}{\partial r^2} + \frac{1}{r}\frac{\partial C_n(r,z)}{\partial r}\right) - \alpha_0(2\pi n f_0)^2 C_n\left(r, z\right) \\ -\frac{jn2\pi f_0\beta}{2\rho_0 c_0^3}\sum_{m=-N_{max}}^{N_{max}} C_m\left(r, z\right) C_{n-m}\left(r, z\right), \\ n = \pm 1, \pm 2, ..., \pm N_{max}.\end{gathered} \tag{4.40}$$

In Eq. 4.40, all of the harmonics interact through nonlinear mixing. The derivatives in Eq. 4.40 are also defined in Eq. 4.31, as for the transient KZK equation.

4.3.3 Muir's method

To establish the accuracy of the numerical results calculated with linear finite difference implementations of the KZK wave equation, Muir's method is utilized as a reference. Other

methods for validation are given in Appendix B. Muir's method, which is valid for small aperture angle and large ka, is effective for calculating the linear pressure field generated by a spherically focused continuous-wave source. Muir's formula for the pressure distribution in cylindrical coordinates predicted by the linear lossless KZK equation is given by

$$P(r,z) = \frac{-jkp_0 exp(jkz + jk\frac{r^2}{2z})}{z} \int_0^a exp\left[\frac{jk\left(r'\right)^2}{2}\left(\frac{1}{R} - \frac{1}{z}\right)\right] J_0\left(k\frac{rr'}{z}\right) r'dr' \quad (z \neq R)\,, \tag{4.41}$$

$$P(0,z) = \frac{p_0 R exp(jkz)}{(R-z)}\left\{1 - exp\left[j\frac{ka^2}{2}\left(\frac{1}{z} - \frac{1}{R}\right)\right]\right\} \quad (z \neq R)\,, \tag{4.42}$$

$$P(r,R) = -j\frac{ka^2}{2R} p_0 exp\left(jkz + jk\frac{r^2}{2R}\right)\frac{2J_1\left(kar/R\right)}{kar/R}, \tag{4.43}$$

$$P(0,R) = -j\frac{ka^2}{2R} p_0 exp\left(jkR\right), \tag{4.44}$$

where p_0 is the pressure at the source, $k = \omega/c$ is the wavenumber, a is the aperture radius, R is the radius of curvature, and $J_0\left(\cdot\right)$ and $J_1\left(\cdot\right)$ are Bessel functions of the first kind of order 0 and 1, respectively.

Muir's method evaluates a single integral when calculating the off-axis pressure. For transient calculations, a Fourier transform operation is required before applying Muir's method. When calculating the transient pressure, the input pulse on the surface of the transducer is expressed as $p_0(t) = \sum_{n=1}^{N} P_n e^{jn\omega_0 t}$, where P_n is the pressure for frequency sample n, ω_0 is the fundamental frequency, and N is the number of frequency samples. Thus, for frequency sample n with wavenumber k_n, Muir's method in Eqs. 4.41-4.44 calculates the pressure distribution in 2D space for each frequency component with

$$P_n(r,z) = P\left(r,z,k_n\right) \quad n = 1,2,3..N. \tag{4.45}$$

Then, after evaluating the inverse Fourier transform in time, the solution in the time domain is

$$p(r,z,t) = \sum_{n=1}^{N} P_n(r,z) e^{jn\omega_0 t}. \tag{4.46}$$

Compared to finite difference KZK calculations, Muir's method is more time-consuming for transient calculations because of the large number of frequencies that are necessary to reconstruct the waveforms at each spatial point. However, Muir's method provides an accurate reference for validating solutions to the linear lossless KZK equation, which is useful for debugging finite difference calculations.

4.4 Results

These simulations were performed on a compute server (Dual Intel Xeon E5-2670 @ 2.5 GHz) with 256 GB RAM. The KZK simulation evaluates a finite difference code written in C++/Mex that runs on 64-bit MATLAB R2017a. Simulations for both linear and nonlinear media are evaluated. The transient input pressure, which is a one-cycle Gaussian weighted sine wave, is generated by a spherically focused transducer. The input pressure on the surface of the transducer is $P_0 = 1.5$ MPa, the aperture radius is $a = 1.5$ cm, the radius of curvature is $R = 6$ cm, the density is $\rho = 1000$ kg/m^3, and the sound speed is $c_0 = 1500$ m/s. The center frequency of the input pressure is $f = 1$MHz, and the wavelength at the center frequency is $\lambda = 0.15$ cm. The sampling frequency is $f_s = 200$ MHz. The finite difference KZK calculation that is employed as a reference utilizes a radial boundary at $r_{max} = 9$ cm, and the spatial step size is $\lambda/40$. The KZK simulation with a PML utilizes a radial boundary at $r_{max} = 3$ cm. For the KZK simulation with the PML, the PML starts at $r = 2.25$ cm and ends at $r_{max} = 3$ cm. The thickness of the layer is therefore equal to 0.75 cm.

4.4.1 KZK simulations for a linear lossless medium

KZK simulations are first performed without attenuation or nonlinearity. Fig. 4.1 compares two on-axis waveforms at $z = 6$ cm, where one is produced by KZK finite difference

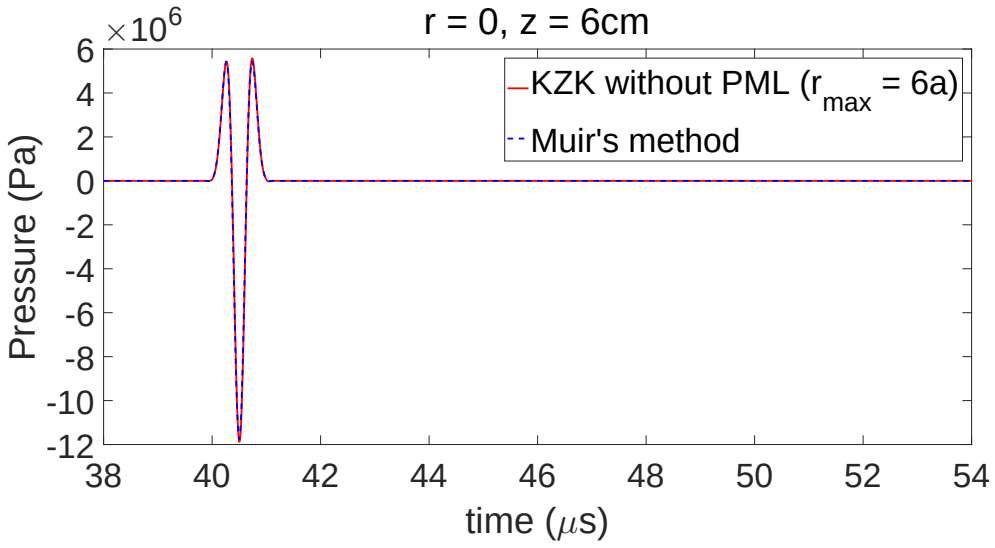

Figure 4.1: Comparison of simulated on-axis waveforms obtained from finite difference KZK calculations (solid line) and Muir's method (dashed line) evaluated in a linear lossless medium at $z = 6$ cm.

calculations (red solid line) and the other is generated by Muir's method (blue dashed line). Fig. 4.1 demonstrates that the results obtained with these two methods match closely at all temporal points in this location. Also, the direct wave and the edge wave have merged in this location.

Fig. 4.2(a) contains the on-axis waveforms evaluated at $z = 6$ cm using finite difference KZK calculations without a PML for a radial boundary at $r_{max} = 6a$ and the KZK simulation without a PML for a radial boundary at $r_{max} = 2a$. These two waveforms match closely for $t < 48\,\mu$s. Near $t = 50\,\mu$s, the reflection from the radial boundary at $r_{max} = 2a$ arrives, which indicates that either the boundary at $r_{max} = 2a$ is too close or that a PML is needed. Fig. 4.2(b) compares two other on-axis waveforms evaluated at $z = 6$ cm calculated with two different PMLs that start at $r = 2.25$ cm to the result without a PML that defines the radial boundary at $r_{max} = 6a$. The blue solid line describes the result calculated with a PML ($y = 0$ with one term) and the green solid line gives the result calculated with another PML

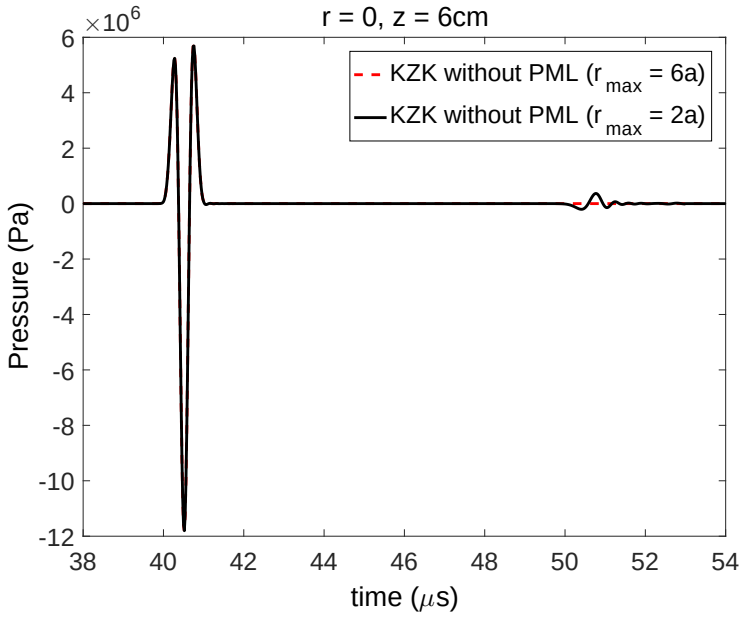

(a)

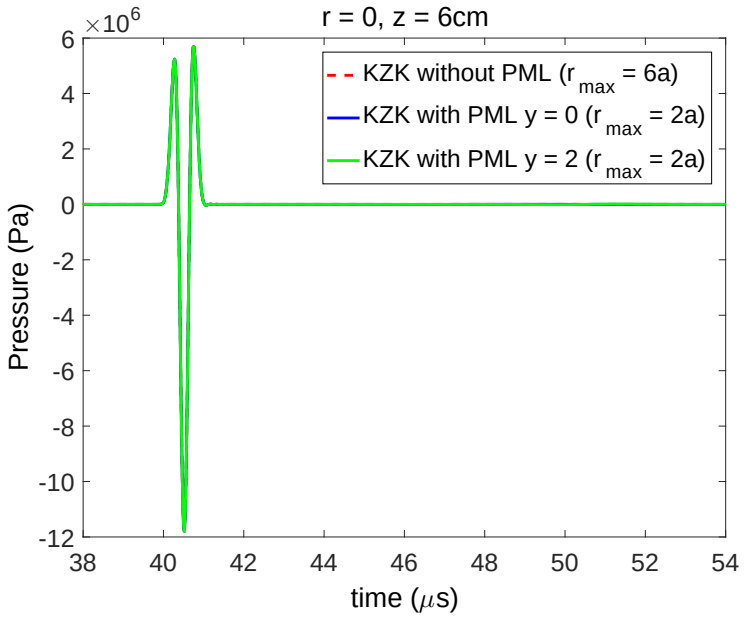

(b)

Figure 4.2: Comparison between on-axis waveforms generated by finite difference KZK calculations in a linear lossless medium at $z = 6$ cm with and without a PML using different radial boundaries. (a) KZK simulation without a PML that defines a radial boundary at $r_{max} = 2a$ (black solid line) and at $r_{max} = 6a$ (red dashed line). (b) KZK simulation without a PML that defines a radial boundary at $r_{max} = 6a$ (red dashed line), with a $y = 0$ single term PML that defines a radial boundary at $r_{max} = 2a$ (blue solid line), and with a $y = 2$ single term PML that defines a radial boundary at $r_{max} = 2a$ (green solid line).

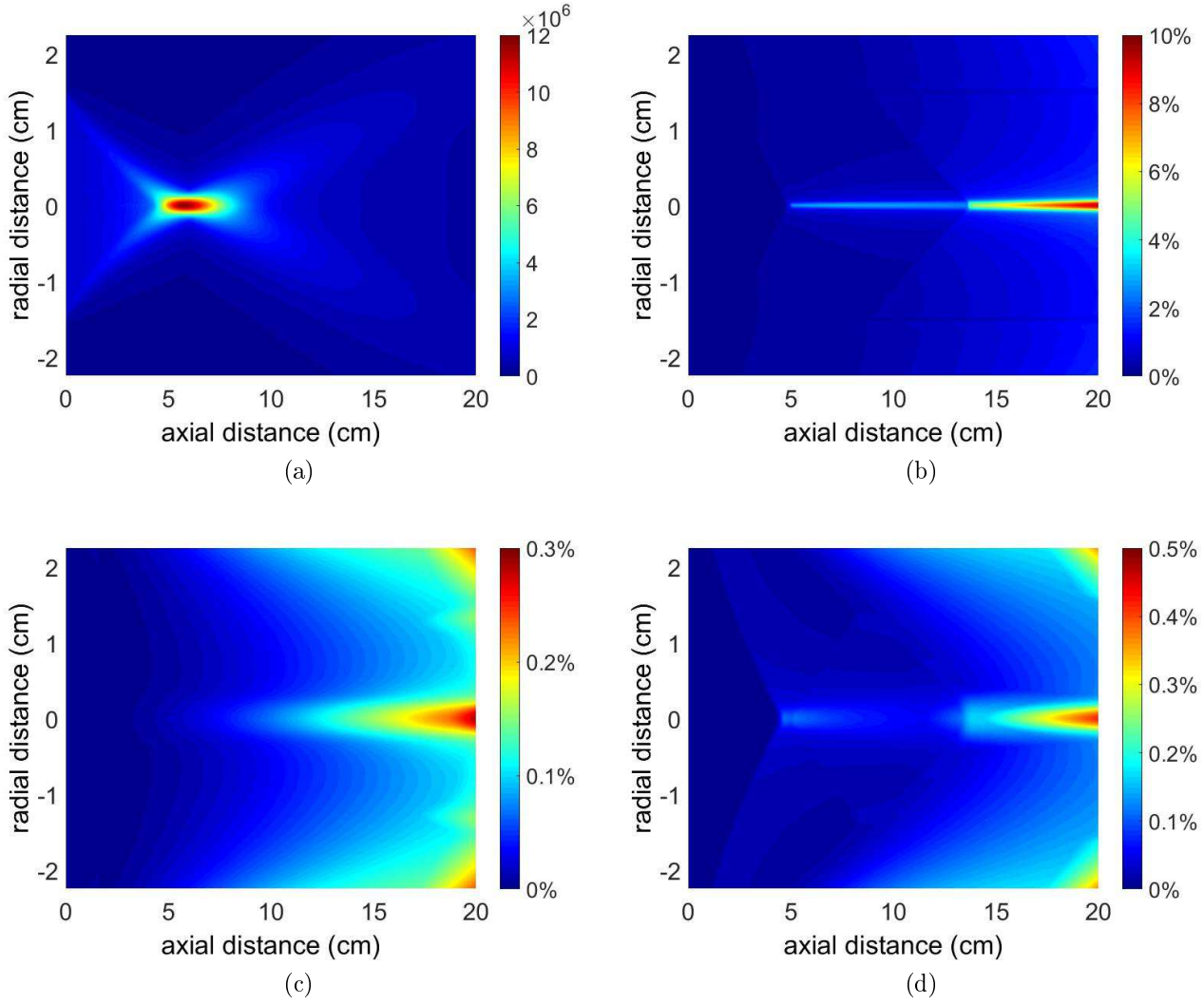

Figure 4.3: Simulated 2D pressure field and differences between KZK calculations without and with PMLs, where the radial boundaries are located at $r_{max} = 9$ cm and at $r_{max} = 3$ cm in a linear lossless medium. (a) The peak pressure distribution for the KZK simulation without a PML that defines a radial boundary at $r_{max} = 9$ cm. (b) The difference between the KZK simulation without a PML that defines a radial boundary at $r_{max} = 9$ cm and the KZK simulation without a PML that defines a radial boundary at $r_{max} = 3$ cm. (c) The difference between the KZK simulation without a PML that defines a radial boundary at $r_{max} = 9$ cm and the KZK simulation with a $y = 0$ single term PML that defines a radial boundary at $r_{max} = 3$ cm. (d) The difference between the KZK simulation without a PML that defines a radial boundary at $r_{max} = 9$ cm and the KZK simulation with a $y = 2$ single term PML that defines a radial boundary at $r_{max} = 3$ cm.

($y = 2$ with one term). Fig. 4.2(b) shows that the reflection from the boundary is removed by each of these PMLs.

Fig. 4.3(a) shows the 2D peak pressure distribution calculated with finite difference KZK calculations without a PML that defines a radial boundary at $r_{max} = 9$ cm ($r_{max} = 6a$), which is sufficiently large so that radial reflections are avoided in most locations. The on-axis focal peak is located at about $z = 6$ cm. The maximum pressure value is equal to 12 MPa. Fig. 4.3(b) shows the 2D difference between the finite difference KZK calculation without a PML for a radial boundary defined at $r_{max} = 9$ cm and the finite difference KZK calculation without a PML for a radial boundary defined at $r_{max} = 3$ cm. The peak value of the difference, which is about 10%, is located on-axis in the far field region. Off-axis, the difference is much smaller. Fig. 4.3(c) shows the 2D difference between the finite difference KZK calculation without a PML that defines a radial boundary at $r_{max} = 9$ cm and the finite difference KZK calculation with a $y = 0$ single term PML that defines a radial boundary at $r_{max} = 3$ cm. The peak value of the difference, which is now only about 0.3%, is again located on-axis in the far field region. There is also some difference off-axis in the far field region in Fig. 4.3(c) due to reflections that arrive later and/or a small amount of mismatch in the PML. Fig. 4.3(d) shows the 2D difference between the finite difference KZK calculation without a PML for a radial boundary defined at $r_{max} = 9$ cm and the finite difference KZK calculation with a single term $y = 2$ PML that defines a radial boundary defined at $r_{max} = 3$ cm. The peak value of the difference, which is about 0.5% for this PML, is also located on-axis in the far field region. Also, some small differences appear on-axis and off-axis in the far field. Comparisons between Fig. 4.3(c) and Fig. 4.3(d) indicate slightly better performance for the $y = 0$ single term PML.

4.4.2 KZK simulations for a nonlinear lossy medium

Simulations are also performed with the attenuation and nonlinearity values for water, which are $\alpha_0 = 2.2 \times 10^{-3}$ dB/cm/MHz^2 and $\beta = 3.5$. Fig. 4.4(a) shows a comparison between the on-axis waveforms evaluated at $z = 6$ cm obtained from the finite difference

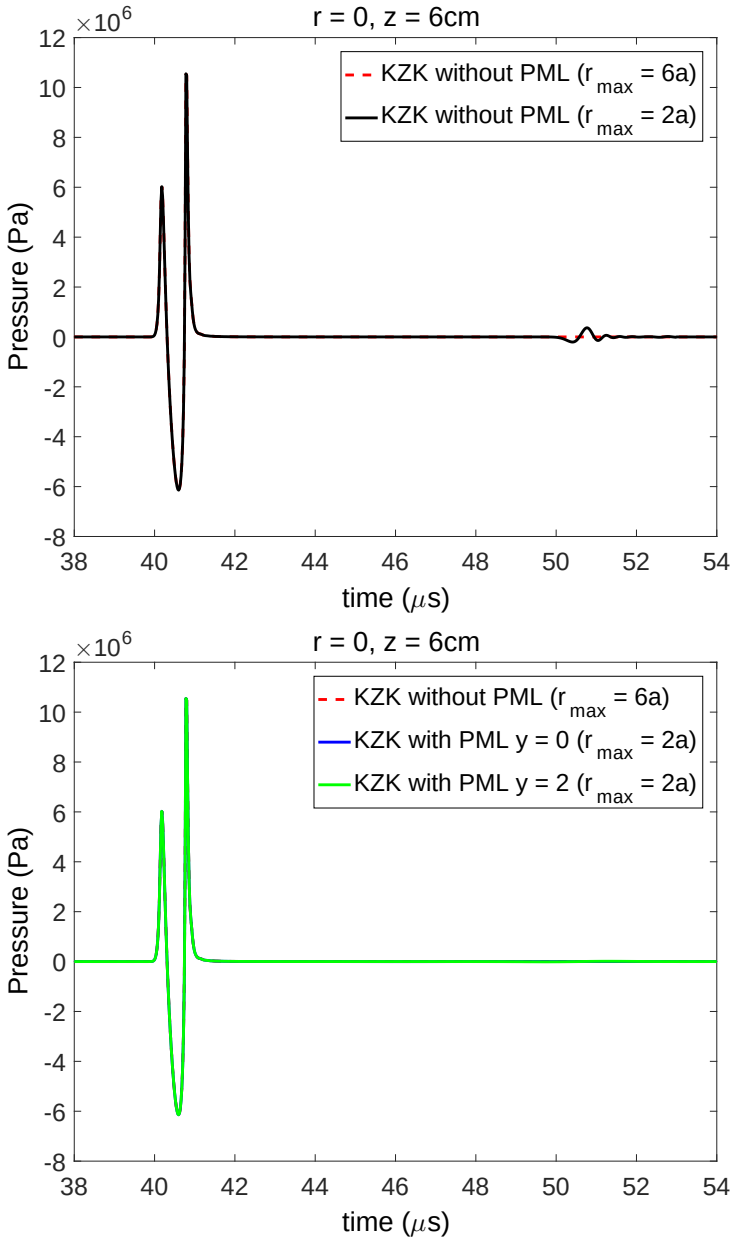

Figure 4.4: Comparison between on-axis waveforms generated by finite difference KZK calculations in a nonlinear medium at $z = 6$ cm with and without a PML for different radial boundaries. The attenuation parameter is $\alpha = 2.2 \times 10^{-3}$ dB/cm/MHz^2, and the nonlinearity parameter is $\beta = 3.5$. (a) KZK simulation without a PML that defines a radial boundary at $r_{max} = 2a$ (black solid line) and at $r_{max} = 6a$ (red dashed line). (b) KZK simulation without a PML that defines a radial boundary at $r_{max} = 6a$ (red dashed line), with a $y = 0$ single term PML that defines a radial boundary at $r_{max} = 2a$ (blue solid line), and with a $y = 2$ single term PML that defines a radial boundary at $r_{max} = 2a$ (green solid line).

KZK simulation without a PML that defines a radial boundary at $r_{max} = 6a$ (red dashed line) and the finite difference KZK simulations without a PML that defines a radial boundary at $r_{max} = 2a$. When nonlinearity is included, the waveforms are tilted where a shockwave is formed in the focal zone. The small difference near $t = 50\,\mu$s in the finite difference KZK simulation without the PML is again caused by the reflection at the radial boundary. Fig. 4.4(b) shows a comparison between the on-axis waveforms at $z = 6$ cm for the finite difference KZK simulation without a PML that defines a radial boundary at $r_{max} = 6a$ and the finite difference KZK simulation with two different PMLs that define a radial boundary at $r_{max} = 2a$. The blue solid line shows the result with a $y = 0$ single term PML and the green solid line describes the result with a $y = 2$ single term PML. Fig. 4.4(b) indicates that the reflection from the boundary is removed by each of these PMLs.

Fig. 4.5 shows the simulated 2D pressure field and the differences between KZK calculations without and with PMLs in a nonlinear medium. Fig. 4.5(a) shows the 2D peak pressure distribution calculated with the finite difference implementation of the KZK equation without a PML that defines a radial boundary at $r_{max} = 9$ cm. The focal peak is located at about $z = 6$ cm on axis, and the maximum pressure value is equal to 12 MPa. Fig. 4.5(b) shows the 2D difference between the finite difference KZK calculation without a PML that defines a radial boundary at $r_{max} = 9$ cm and the finite difference KZK calculation without a PML that defines a radial boundary at $r_{max} = 3$ cm. The peak value of the difference, which is about 10%, is located on-axis in the far field region. Fig. 4.5(c) shows the 2D difference between the finite difference KZK calculation without a PML that defines a radial boundary at $r_{max} = 9$ cm and the finite difference KZK calculation with the $y = 0$ single term PML that defines a radial boundary at $r_{max} = 3$ cm. The peak value of the difference, which is about 0.3%, is again located on-axis in the far region. There is also some difference in the far off-axis region in Fig. 4.5(c). Fig. 4.5(d) shows the 2D difference between the finite difference KZK calculation without a PML that defines a radial boundary at $r_{max} = 9$ cm and the finite difference KZK calculation with the $y = 2$ single term PML that defines a

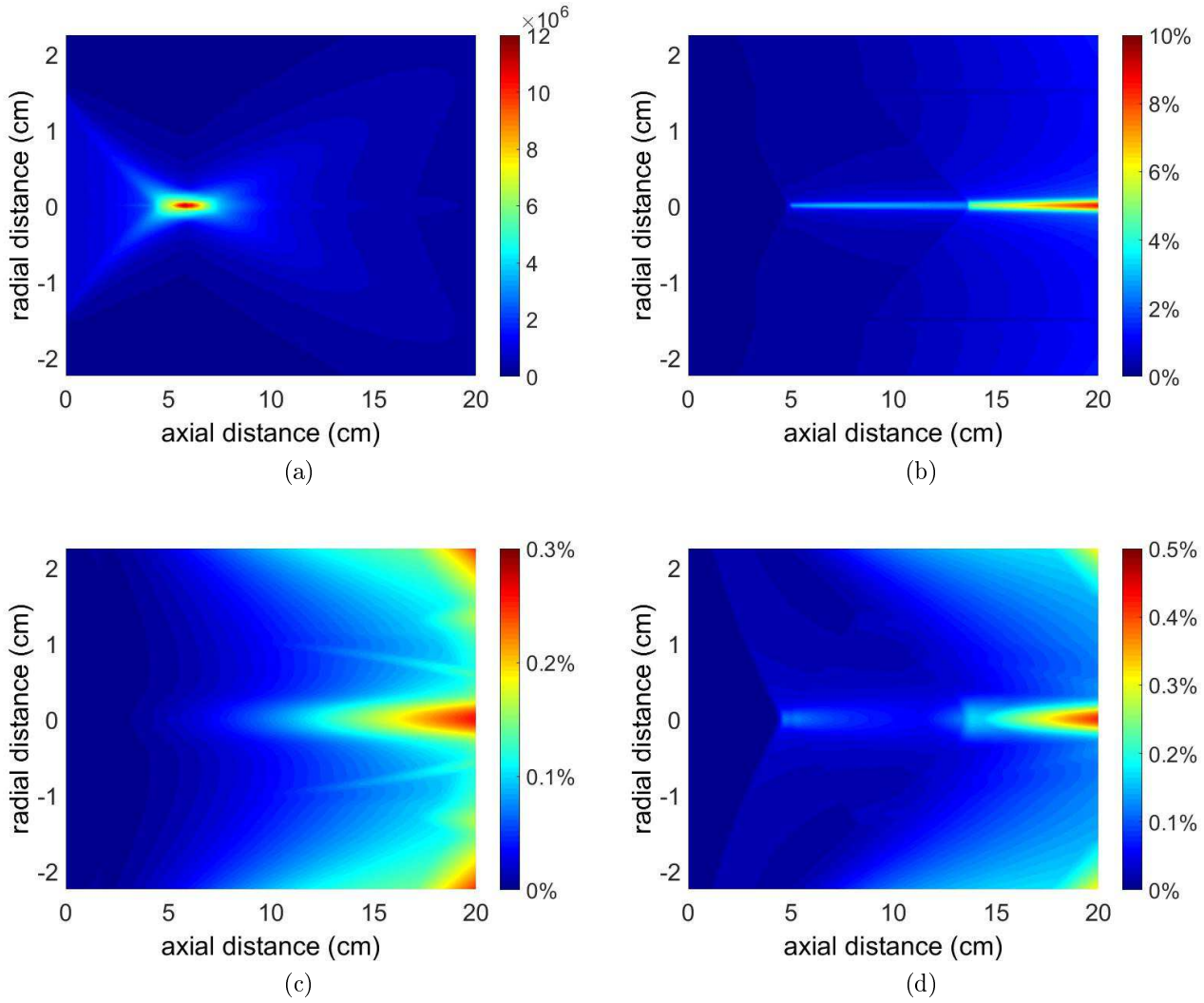

Figure 4.5: Simulated 2D pressure field and differences between KZK calculations without and with PMLs, where the radial boundaries are located at $r_{max} = 9$ cm and at $r_{max} = 3$ cm in a nonlinear medium. The attenuation parameter is $\alpha = 2.2 \times 10^{-3}$ dB/cm/MHz^2 and the nonlinearity parameter is $\beta = 3.5$. (a) The peak pressure distribution for the KZK simulation without a PML that defines a radial boundary at $r_{max} = 9$ cm. (b) The difference between the KZK simulation without a PML that defines a radial boundary at $r_{max} = 9$ cm and the KZK simulation without a PML that defines a radial boundary at $r_{max} = 3$ cm. (c) The difference between the KZK simulation without a PML that defines a radial boundary at $r_{max} = 9$ cm and the KZK simulation with a $y = 0$ single term PML that defines a radial boundary at $r_{max} = 3$ cm. (d) The difference between the KZK simulation without a PML that defines a radial boundary at $r_{max} = 9$ cm and the KZK simulation with a $y = 2$ single term PML that defines a radial boundary at $r_{max} = 3$ cm.

radial boundary at $r_{max} = 3$ cm. The peak value of the difference, which is about 0.5% for this PML, is also located on-axis in the far field region. Again, a smaller difference is observed in Fig. 4.5(d) than in Fig. 4.5(c), which indicates slightly better performance for the $y = 0$ single term PML.

4.5 Discussion

4.5.1 Computation time

Figs. 4.3 and 4.5 indicate that, for both linear and nonlinear KZK simulations, the PMLs with $y = 0$ and $y = 2$ are effective in suppressing reflections from the radial boundary, especially in the focal zone. The choice of α_{PML} balances the effect of impedance mismatch when α_{PML} is large versus the effect of boundary reflections when α_{PML} is too small. For each type of PML, our experience is that there is no significant difference in the PML when only one or two terms are considered in the power law wave equation. Thus, to further accelerate these KZK simulations, only one term is included in each simulation for the $y = 0$ and $y = 2$ PMLs. The computation time for the KZK finite difference calculation without a PML that defines a radial boundary at $r_{max} = 9$ cm shown in Fig. 4.3 is 2807s. For KZK simulations using a $y = 0$ single term PML that defines a radial boundary at $r_{max} = 3$ cm, the computation time is 913s. For KZK simulations using a $y = 2$ single term PML that defines a radial boundary at $r_{max} = 3$ cm, the computation time is 1028s.

4.5.2 Continuous wave (CW) KZK calculations

The same approach for defining a PML is also applicable to continuous-wave KZK simulations, as described in Appendix A. For the continuous wave KZK equation, a PML is only necessary in the radial direction. The strength of the PML, as implemented here, increases proportionally to the radial direction cubed. The effectiveness of the $y = 0$ and $y = 2$ single term PMLs is also demonstrated for CW calculations with the spherically-focused transducer evaluated in section 4.4. The input pressure on the surface of the transducer

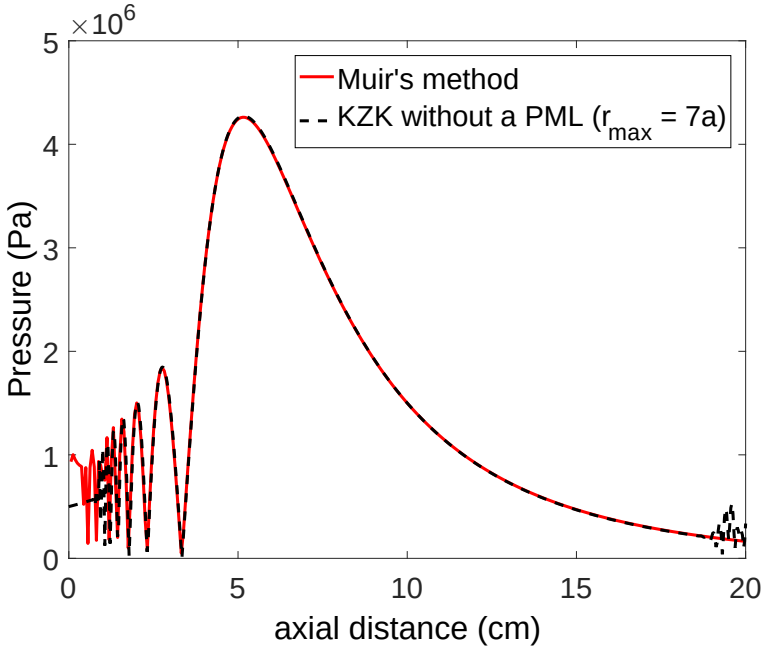

(a)

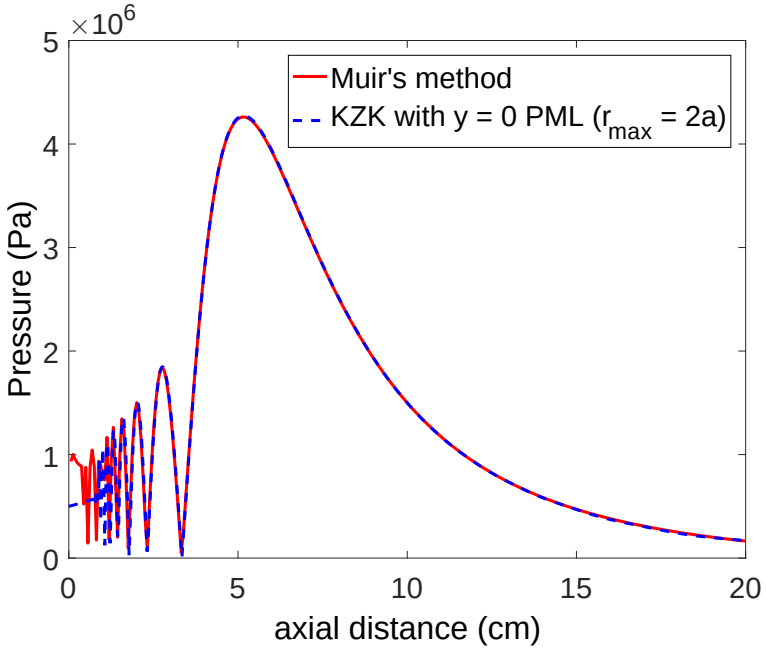

(b)

Figure 4.6: On-axis comparisons between continuous wave finite difference KZK simulations with the results calculated with Muir's method evaluated in a linear lossless medium. (a) The result obtained with Muir's method (red solid line) and the finite difference KZK simulation results without a PML that defines a radial boundary at $r_{max} = 10.5$ cm (blue dashed line). (b) The result with Muir's method (red solid line) and the finite difference KZK simulation results with a $y = 0$ PML that defines a radial boundary at $r_{max} = 3$ cm (blue dashed line).

is $P_0 = 0.5$ MPa. The density is $\rho = 1000$ kg/m^3, and the sound speed is $c = 1500$ m/s. The excitation frequency is $f = 1$ MHz, which corresponds to a wavelength of $\lambda = 0.15$ cm. For the finite difference KZK simulation without a PML, the radial boundary is located at $r_{max} = 10.5$ cm. For the finite difference KZK simulation with a $y = 0$ single term PML, the PML starts at $r = 2.25$ cm and ends at $r_{max} = 3$ cm, so the thickness of the PML is equal to 0.75 cm.

The finite difference solution to the continuous-wave KZK equation is first computed in a linear lossless medium. Only the first harmonic is computed in the simulation, where the spatial step size is equal to $\lambda/40$ in both directions. Fig. 4.6 describes the on-axis results for the continuous wave KZK simulations with and without a PML, which are compared to the results calculated with Muir's method. As shown in Fig. 4.6(a), the on-axis pressure waveform obtained from the finite difference KZK simulation without a PML closely matches the waveform computed with Muir's method in the focal zone; however, there is some difference in the far field region, even for the large radial boundary that is defined at $r_{max} = 10.5$ cm. Fig. 4.6(b) describes the on-axis waveform obtained from the finite difference KZK simulation with a $y = 0$ PML that defines a radial boundary at $r_{max} = 3$ cm, which closely matches the result obtained with Muir's method both in the focal zone and in the far field region. This indicates that the reflection from the boundary is removed by the PML.

Fig. 4.7 shows the continuous-wave 2D pressure distribution for a spherically-focused transducer with $a = 1.5$ cm, $R = 6$ cm, and $f = 1$ MHz calculated in a linear lossless medium with Muir's method. In Fig. 4.7, the peak pressure in the focal zone is approximately 4.3 MPa. Fig. 4.8(a) describes the difference between the finite difference KZK numerical calculation without a PML that defines a radial boundary at $r_{max} = 10.5$ cm and the results obtained with Muir's method. The reflection from the radial boundary is clearly evident in Fig. 4.8(a), which starts at the edge near $z = 16.5$ cm. The peak difference is about 0.5 MPa in the on-axis far field region. Fig. 4.8(b) shows that, after introducing a $y = 0$

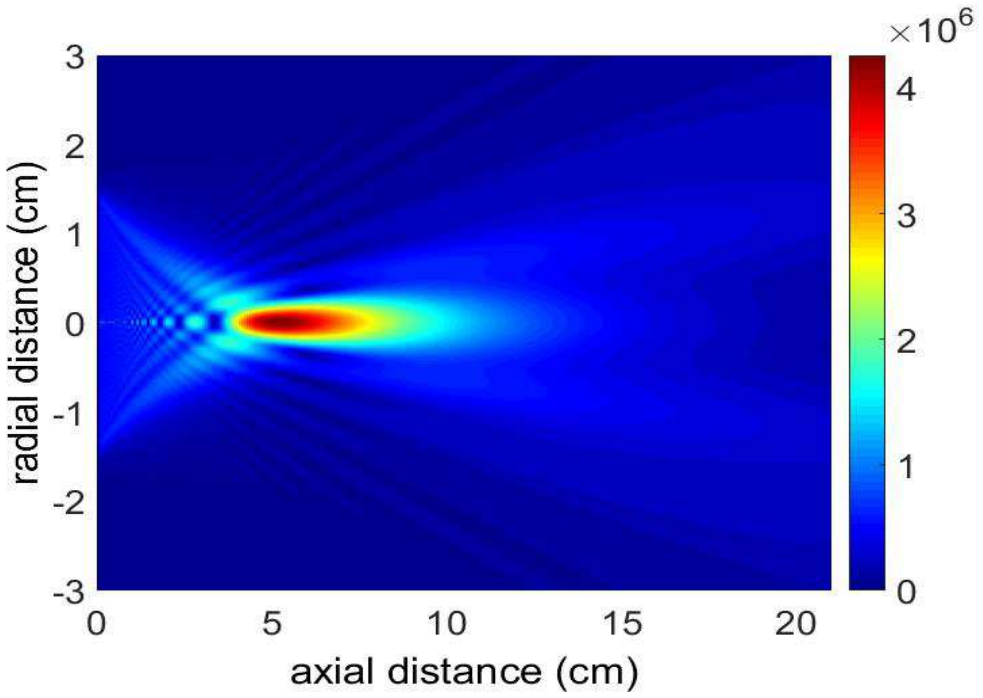

Figure 4.7: The continuous-wave 2D pressure distribution for a spherically-focused transducer with $a = 1.5$ cm, $R = 6$ cm, and $f = 1$ MHz calculated in a linear lossless medium with Muir's method.

PML that defines a radial boundary at $r_{max} = 3$ cm, the on-axis difference is much smaller than the on-axis difference without a PML in Fig. 4.8(a). The largest difference that occurs in Fig. 4.8(b) is observed where the PML is applied.

Simulations are then evaluated for the same transducer geometry using the attenuation and nonlinearity values of water, which are $\alpha_0 = 2.2 \times 10^{-3}$ dB/cm/MHz^2 and $\beta = 3.5$, respectively. The number of harmonics computed in this simulation is $N_{harm} = 50$, and the spatial step size is $\lambda/N_{harm}/40$. Fig. 4.9(a) shows the first four harmonics of the on-axis finite difference simulation results for the continuous wave KZK equation evaluated in water. This simulation defines a radial boundary at $r_{max} = 10.5$ cm without a PML. In Fig. 4.9(a), there is a very strong oscillation in the fundamental due to reflections from the boundary. However, no such oscillations appear in the higher harmonics. Fig. 4.9(b) shows the first four harmonics evaluated on-axis for the continuous-wave KZK equation in water with a $y = 0$ PML that defines a radial boundary at $r_{max} = 3$ cm. In Fig. 4.9(b), no oscillations appear

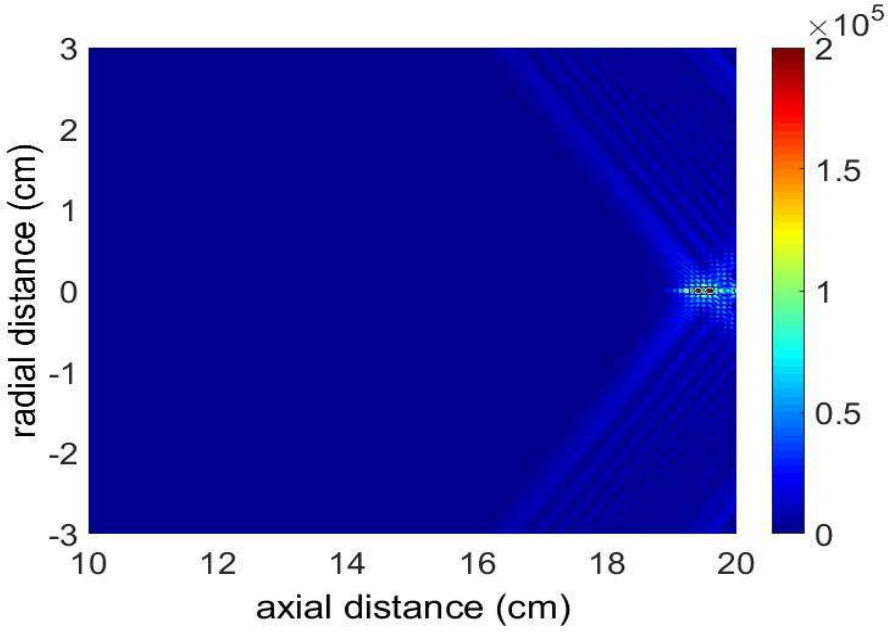

(a)

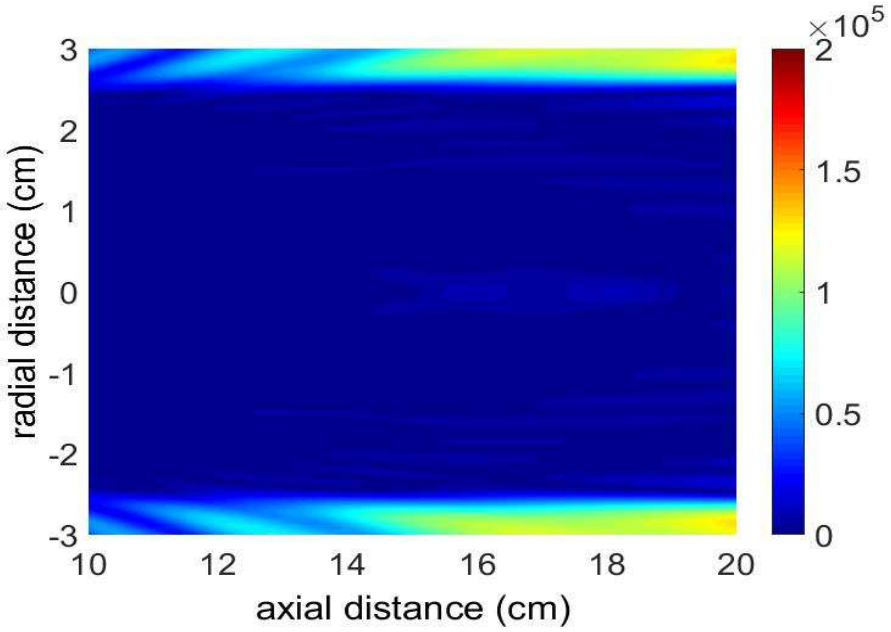

(b)

Figure 4.8: The 2D pressure difference between linear lossless finite difference KZK numerical results for a spherically-focused transducer with $a = 1.5$ cm, $R = 6$ cm, and $f = 1$ MHz and the results for the same configuration evaluated with Muir's method. (a) The difference between the finite difference KZK simulation without a PML that defines a radial boundary at $r_{max} = 10.5$ cm and the results obtained with Muir's method. (b) The difference between the finite difference KZK simulation with a $y = 0$ PML that defines a radial boundary at $r_{max} = 3$ cm and the results obtained with Muir's method.

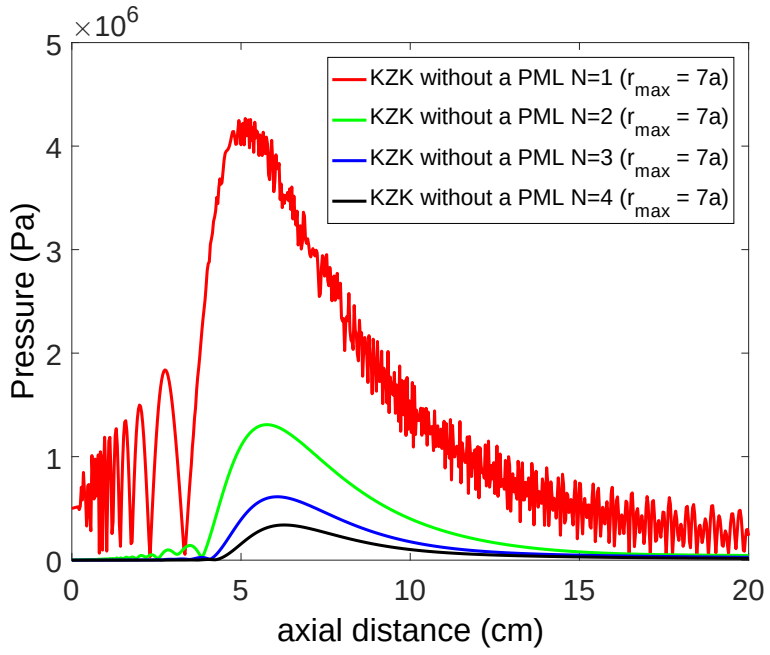

(a)

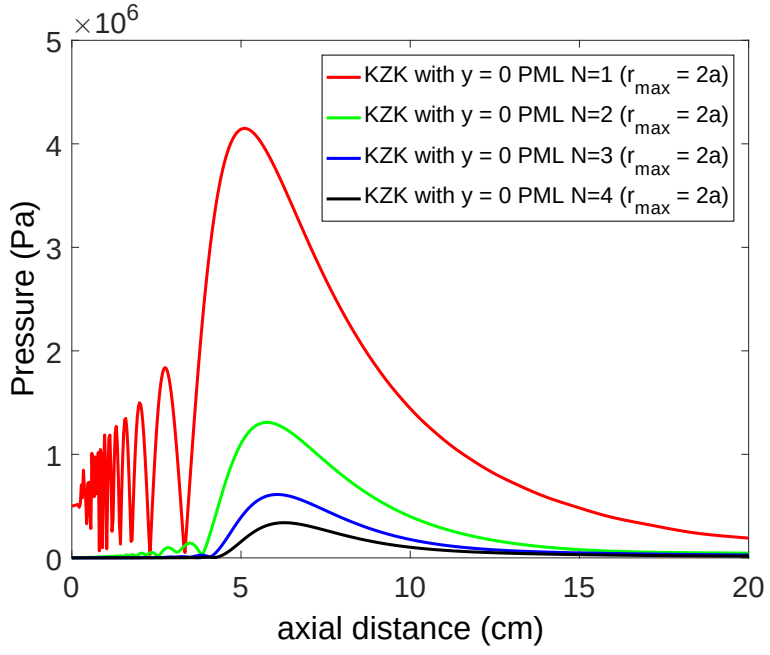

(b)

Figure 4.9: The first four harmonics generated by a spherically-focused transducer with $a = 1.5$ cm, $R = 6$ cm, and $f = 1$ MHz for on-axis finite difference simulations of the continuous wave KZK equation in water. The attenuation parameter is $\alpha = 2.2 \times 10^{-3}$ dB/cm/MHz^2, and the nonlinearity parameter is $\beta = 3.5$. (a) The finite difference KZK simulation results without a PML that defines a radial boundary at $r_{max} = 10.5$ cm. (b) The finite difference KZK simulation results with a $y = 0$ PML that defines a radial boundary at $r_{max} = 3$ cm.

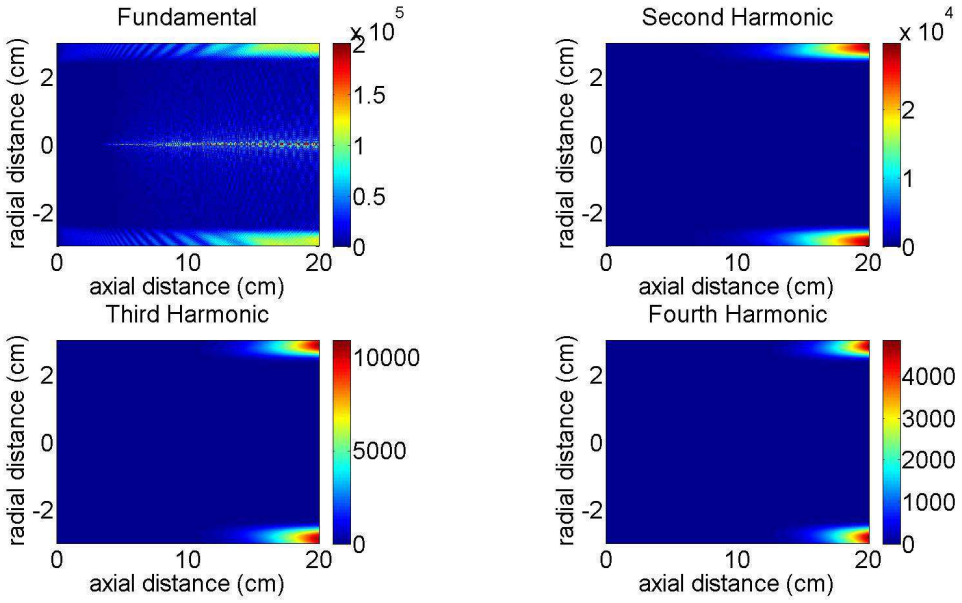

Figure 4.10: The 2D pressure difference between the finite difference KZK numerical results with and without a $y = 0$ PML in water with $\alpha_0 = 2.2 \times 10^{-3}$ dB/cm/MHz^2 and $\beta = 3.5$ evaluated for first four harmonics produced by a spherically-focused transducer with $a = 1.5$ cm, $R = 6$ cm, and $f = 1$ MHz.

in the fundamental or in any of the higher harmonics. For the higher harmonics, the finite difference solution to the continuous-wave KZK equation with or without a PML produces exactly the same on-axis result.

Fig. 4.10 shows the first four harmonics of the difference between the finite difference KZK numerical calculation without a PML that defines a radial boundary at $r_{max} = 10.5$ cm and the KZK numerical calculation with a $y = 0$ PML that defines a radial boundary at $r_{max} = 3$ cm. Fig. 4.10(a) indicates the main difference in the first harmonic occurs close to the central axis, where the source of this difference is the reflection from the radial boundary at $r_{max} = 10.5$ cm. Figs. 4.10(b-d) indicate that, for higher harmonics, the difference is negligible since the reflection from the radial boundary is much smaller for the higher frequency components.

4.6 Conclusion

A new perfectly matched layer was implemented for simulations of nonlinear wave propagation based on the Khokhlov-Zabolotskaya-Kuznetsov equation. Instead of deriving a PML with stretched coordinates, the power law wave equation is introduced as an alternative model for the attenuation that occurs within the PML. For each value of the power law exponent considered here, the two terms that are responsible for the attenuation are reduced to a single term, which yields the Telegrapher's equation within the PML when $y = 0$ and the Blackstock viscous wave equation when $y = 2$. Numerical simulations are evaluated in both linear lossless and nonlinear lossy media for inputs generated by a spherically focused transducer. The simulation results are compared to Muir's formula and to finite difference KZK solutions with a very large radial boundary. Comparisons show that the PMLs effectively eliminate the reflections from the radial boundary. In addition, the formulas for implementing PMLs are readily integrated into existing KZK simulation programs. With these new PMLs, reflections from the radial boundary are eliminated, which enables a considerable reduction in the computation time for finite difference simulations of the KZK equation.

Chapter 5

Conclusion

Chapter 2 numerically evaluates time-domain Green's functions for three time-fractional wave equations, and the results are compared at various distances for water, breast, and liver. At larger distances, the time-domain Green's functions for all three fractional wave equations converge to the same result in the water, breast, and liver models. The results also demonstrate that the Szabo and power law wave equations are noncausal and that the Caputo wave equation is causal, where the distinction between these is clearly evident at distances very close to the source. However, beyond a certain distance, the noncausal contributions are negligible for both the Szabo and power law wave equations. When these time-domain Green's functions are convolved with a three-cycle Hanning-weighted pulse, no noncausal behavior is observed in the time-domain results, and the FWHMs of the envelopes of the convolution results are all approximately the same.

In Chapter 3, improved approximations for the attenuation and phase velocity are derived for the Chen-Holm and Treeby-Cox wave equations. Numerical calculations of the attenuation and phase velocity for the Chen-Holm, Treeby-Cox, and power law wave equations in breast and liver are evaluated over a range of ultrasound frequencies. New expressions for power series match the results obtained by numerically evaluating the dispersion relation more closely than previous approximations. The time-domain Green's functions for these three fractional wave equations are calculated at various distances, and the amplitudes and FWHM values of the time-domain Green's functions are also evaluated. The results show some similarities and differences between these three fractional wave equations. For instance,

the attenuation terms in all three fractional wave equations are very similar, while the phase velocity for the Chen-Holm wave equation is nearly constant. Causality is demonstrated analytically and numerically in the time domain for both the Chen-Holm and Treeby-Cox wave equations. At much larger distances, the time-domain Green's functions for the Treeby-Cox and power law wave equations converge to the same result while the time-domain Green's function for the Chen-Holm wave equation clearly differs from the other two. The Pantis method is introduced as an effective approach for evaluating the highly oscillatory improper integrals that arise in numerical calculations of the time-domain Green's functions for the Chen-Holm and Treeby-Cox space-fractional wave equations. The Pantis method provides an accurate result when the number of Filon abscissas and the value of m are sufficiently large. Three-cycle Hanning-weighted pulses with two different center frequencies are convolved with the time-domain Green's functions for three fractional wave equations. The convolution results for the power law wave equation and the Treeby-Cox wave equation are very similar while the convolution result for the Chen-Holm wave equation clearly shows a time delay. The convolution results also indicate that there is more attenuation and waveform spreading in signals with higher center frequencies.

In Chapter 4, a new PML, which is based on the power law wave equation with $y = 0$ or $y = 2$, is implemented to accelerate nonlinear ultrasound simulations with the KZK equation. For each power law exponent, a single attenuation term is sufficient to avoid radial reflections. In addition, the finite difference structure of the KZK equation is also described. Numerical simulations for the transient and continuous-wave KZK equations are then evaluated for both linear lossless and nonlinear media, where the inputs are generated by a spherically focused transducer. These results are compared to Muir's formula and to finite difference KZK calculations with a large radial boundary. The comparisons indicate that the new PML effectively eliminates the reflections from the radial boundary, which subsequently reduces the computation time.

APPENDICES

APPENDIX A

Derivation of the nonlinear wave equations

The Westervelt equation

A wave equation that describes nonlinear wave propagation is derived from three fundamental equations, namely the equation of motion, the continuity equation, and the equation of state. The equation of motion is given by

$$\rho \frac{D\mathbf{u}}{Dt} + \overrightarrow{\nabla} P = 0, \tag{A.1}$$

where $\rho = \rho_0 + \rho_a$ is the total density, $P = P_0 + p$ is the total pressure, $\mathbf{u}$ is the velocity, and $\frac{D}{Dt} = \frac{\partial}{\partial t} + \mathbf{u} \cdot \overrightarrow{\nabla}$. Acoustic quantities are usually very small compared to the static values. The continuity equation is expressed as

$$\frac{D\rho}{Dt} + \rho \nabla \cdot \mathbf{u} = 0. \tag{A.2}$$

The equation of state is given by

$$P = P_0 + \left(\frac{\partial P}{\partial \rho}\right)_{\rho_0, s} \rho_a + \frac{1}{2}\left(\frac{\partial^2 P}{\partial \rho^2}\right)_{\rho_0, s} \rho_a^2 + \ldots . \tag{A.3}$$

For all three constitutive equations, all terms up to second order accuracy are retained with respect to ρ_a, p, and $\mathbf{u}$, which are sufficient for most applications of nonlinear acoustics in fluids. Accordingly, Eqs. A.1-A.3 are rewritten as

$$\rho_0 \frac{\partial \mathbf{u}}{\partial t} + \overrightarrow{\nabla} p = -\rho_a \frac{\partial \mathbf{u}}{\partial t} - \rho_0 \left(\mathbf{u} \cdot \overrightarrow{\nabla} \right) \mathbf{u}, \tag{A.4}$$

$$\frac{\partial \rho_a}{\partial t} + \rho_0 \overrightarrow{\nabla} \cdot \mathbf{u} = -\rho_a \overrightarrow{\nabla} \cdot \mathbf{u} - \mathbf{u} \cdot \overrightarrow{\nabla} \rho_a, \tag{A.5}$$

$$\rho_a - \frac{p}{c_0^2} \approx -\frac{B}{2A} \frac{p^2}{\rho_0 c_0^4}, \tag{A.6}$$

where $A = \rho_0 \left(\frac{\partial P}{\partial \rho} \right)_{\rho_0, s}$ and $B = \rho_0^2 \left(\frac{\partial^2 P}{\partial \rho^2} \right)_{\rho_0, s}$. The right hand sides of Eqs. A.4-A.6 contain the second order terms. Combining Eqs. A.4-A.6 yields the Westervelt equation

$$\nabla^2 p - \frac{1}{c_0^2} \frac{\partial^2 p}{\partial t^2} = -\frac{\delta}{c_0^4} \frac{\partial^3 p}{\partial t^3} - \frac{\beta}{\rho_0 c_0^4} \frac{\partial^2 p^2}{\partial t^2}, \tag{A.7}$$

where δ and $\beta = 1 + B/2A$ are the attenuation and nonlinearity parameters.

The KZK equation

To obtain an approximate nonlinear wave equation that describes one way wave motion in the axial direction, let z represent the direction of propagation, where (x, y) indicates the coordinates perpendicular to the z axis. Assuming that, for a source with radius a, $ka \gg 1$ and $z > 0.5ka^2$ are both satisfied, the effects of diffraction are $O(\tilde{\varepsilon}^2)$ in each direction are scaled by different amounts according to

$$p = p(x_1, y_1, z_1, t'), \quad (x_1, y_1, z_1) = (\tilde{\varepsilon}^{1/2} x, \tilde{\varepsilon}^{1/2} y, \tilde{\varepsilon} z), \quad t' = t - z/c_0. \tag{A.8}$$

The Laplacian that appears in the Westervelt equation is then rewritten as

$$\nabla^2 = \tilde{\varepsilon} \left(\frac{\partial^2}{\partial x_1^2} + \frac{\partial^2}{\partial y_1^2} \right) + \tilde{\varepsilon}^2 \frac{\partial^2}{\partial z_1^2} - \tilde{\varepsilon} \frac{2}{c_0} \frac{\partial^2 p}{\partial z_1 \partial t'} + \frac{1}{c_0^2} \frac{\partial^2}{\partial t'^2}. \tag{A.9}$$

If only $O(\tilde{\varepsilon})$ terms are retained, the left side of the Westervelt equation becomes

$$\nabla^2 p - \frac{1}{c_0^2}\frac{\partial^2 p}{\partial t^2} = \tilde{\varepsilon}\left(\frac{\partial^2}{\partial x_1^2} + \frac{\partial^2}{\partial y_1^2}\right) p - \tilde{\varepsilon}\frac{2}{c_0}\frac{\partial^2 p}{\partial z_1 \partial t'}. \tag{A.10}$$

Let $\nabla_\perp = \frac{\partial^2}{\partial x^2} + \frac{\partial^2}{\partial y^2}$ and replace (x_1, y_1, z_1) with (x, y, z) to obtain the KZK (Khokhlov-Zabolotskaya-Kuznetsov) equation

$$\frac{\partial^2 p}{\partial z \partial t'} = \frac{c_0}{2}\nabla_\perp p + \frac{\delta}{2c_0^3}\frac{\partial^3 p}{\partial t'^3} + \frac{\beta}{2\rho_0 c_0^3}\frac{\partial^2 p^2}{\partial t'^2}. \tag{A.11}$$

This yields a simplified model that includes the effects of diffraction, attenuation, and nonlinearity. When the source is a circular transducer, the pressure field is symmetric in the radial direction. In axisymmetric cylindrical coordinates, the KZK equation is given by

$$\frac{\partial^2 p}{\partial z \partial t'} = \frac{c_0}{2}\left(\frac{\partial^2 p}{\partial r^2} + \frac{1}{r}\frac{\partial p}{\partial r}\right) + \frac{\delta}{2c_0^3}\frac{\partial^3 p}{\partial t'^3} + \frac{\beta}{2\rho_0 c_0^3}\frac{\partial^2 p^2}{\partial t'^2}. \tag{A.12}$$

Burgers' equation

Burgers' equation, which is a one dimensional nonlinear equation, can be derived directly from the Westervelt equation. After the operators in Eq. A.7 are factored, this yields

$$\left(\frac{\partial}{\partial z} - \frac{1}{c_0}\frac{\partial}{\partial t} + \frac{\delta}{2c_0}\frac{\partial^2}{\partial t^2} + \frac{\beta p}{\rho_0 c_0^3}\frac{\partial}{\partial t}\right)\left(\frac{\partial}{\partial z} + \frac{1}{c_0}\frac{\partial}{\partial t} - \frac{\delta}{2c_0}\frac{\partial^2}{\partial t^2} - \frac{\beta p}{\rho_0 c_0^3}\frac{\partial}{\partial t}\right) p = 0. \tag{A.13}$$

In Eq. A.13, $\frac{\delta}{2c_0}\frac{\partial^2}{\partial t^2}$ and $\frac{\beta p}{\rho_0 c_0^3}\frac{\partial}{\partial t}$ are higher order terms, and the product of these are discarded when transforming Eq. A.13 back to Eq. A.7. Assuming one way approximation and retaining only the forward propagation terms gives

$$\frac{\partial p}{\partial z} - \frac{1}{c_0}\frac{\partial p}{\partial t} + \frac{\delta}{2c_0}\frac{\partial^2 p}{\partial t^2} + \frac{\beta p}{\rho_0 c_0^3}\frac{\partial p}{\partial t} = 0. \tag{A.14}$$

applying the change of variables $z' = z - c_0 t$, Burgers' equation is obtained

$$\frac{\partial p}{\partial z'} + \frac{\delta}{2c_0}\frac{\partial^2 p}{\partial t^2} + \frac{\beta p}{\rho_0 c_0^3}\frac{\partial p}{\partial t} = 0. \tag{A.15}$$

APPENDIX B

Simulations of ultrasound wave propagation

The fast nearfield method

The fast nearfield method (FNM) simulates the linear lossless pressure field generated by transducers of various shapes. In time domain, the pressure field produced by a circular piston is given by:

$$p(r,z;t) = \frac{\rho_0 ca}{\pi}\int_0^{\pi} \frac{r\cos\psi - a}{r^2 + a^2 - 2ar\cos\psi} \times [v(t-\tau_1) - v(t-\tau_2)]d\psi, \tag{B.1}$$

$$\tau_1 = \sqrt{z^2 + r^2 + a^2 - 2ar\cos\psi}/c, \qquad \tau_2 = z/c, \tag{B.2}$$

where a is the radius of the circular piston, τ_1 and τ_2 are the delay times, and v is the normal velocity for source points on the piston. The fast nearfield method is an accurate method for computing pressures in both the near field and the far field.

The Cole-Hopf Model

The Cole-Hopf model gives an exact solution to Burgers' equation for given values of the nonlinearity and attenuation coefficients. For an arbitrary source pressure on the piston,

$$p(0,t) = p_0 F(t), \tag{B.3}$$

the Cole-Hopf solution including both nonlinearity and attenuation is given by

$$p(z,t') = p_0 \frac{\int_{-\infty}^{\infty} F(t'') e^{E_\zeta} e^{-E_G} dt''}{\int_{-\infty}^{\infty} e^{E_\zeta} e^{-E_G} dt''}, \tag{B.4}$$

$$E_\zeta(t'') = \frac{\beta p_0}{\rho_0 \delta} \int_{-\infty}^{t''} F(t''') dt''', \tag{B.5}$$

$$E_G = \frac{c_0^3 (t' - t'')^2}{2z\delta}, \tag{B.6}$$

where $t' = t - z/c_0$ is retarded time, β is the nonlinearity coefficient, and δ is the attenuation coefficient. When β equals zero, E_ζ equals zero, and the Cole-Hopf solution simplifies to the linear case. For each frequency ω, the amplitude is attenuated by $exp(-\omega^2 z\delta/2c_0^3)$ after a distance z. Thus, for a single frequency excitation, the linear Cole-Hopf solution with attenuation only is given by

$$p(z,t') = p_0 e^{-\omega^2 z\delta/2c_0^3} \sin(\omega t') . \tag{B.7}$$

Fay and Fubini Model

When only nonlinearity is considered in the simulation, the Fay and Fubini solutions can be used for comparison. For periodic waves, the expression for the pressure can be expanded as a Fourier series, which clearly shows how the harmonics grow as the periodic waves propagate. In Fubini's model, the source pressure is given by

$$p(0,t) = p_0 \sin(\omega t) . \tag{B.8}$$

For this input, the Fubini solution for a single frequency source is

$$p(\sigma,t') = p_0 \sum_{n=1}^{\infty} \frac{2}{n\sigma} J_n(n\sigma) \sin(n\omega t') , \tag{B.9}$$

where σ is a dimensionless distance. The Fubini solution is only valid in the pre-shock region $\sigma \leq 1$. In this region, when σ increases, the amplitude of the fundamental component decreases and the energy is transferred to higher harmonic components.

After the shock wave is fully developed, the Fay solution is chosen instead of the Fubini solution since the Fay solution is valid for larger values of σ. When both attenuation and nonlinearity are included, the Fay solution is expressed as

$$p(\sigma, t') = p_0 \frac{2}{\Gamma} \sum_{n=1}^{\infty} \frac{\sin(n\omega t')}{\sin[n(1+\sigma)/\Gamma]}, \tag{B.10}$$

where Γ is a parameter that describes the attenuation. When only the effects of nonlinearity are included, the Fay solution simplifies to a sawtooth wave

$$p(\sigma, t') = p_0 \frac{2}{1+\sigma} \sum_{n=1}^{\infty} \frac{\sin(n\omega t')}{n}, \tag{B.11}$$

which is valid for the region where $\sigma > 3$. Thus, by combining the Fubini and Fay solutions, results obtained with Burgers' equation can be validated. If additional comparisons are needed in the region $1 < \sigma \leq 3$, the solution in the transition region is needed [85].

BIBLIOGRAPHY

BIBLIOGRAPHY

[1] P. Laugier and G. Haïat. Introduction to the physics of ultrasound. In *Bone Quantitative Ultrasound*, pages 29–45. Springer, 2011.

[2] S. A. Goss, L. A. Frizzell, and F. Dunn. Ultrasonic absorption and attenuation in mammalian tissues. *Ultrasound in Medicine & Biology*, 5(2):181–186, 1979.

[3] K. J. Parker. Ultrasonic attenuation and absorption in liver tissue. *Ultrasound in Medicine & Biology*, 9(4):363–369, 1983.

[4] A. S. Khimunin. Numerical calculation of the diffraction corrections for the precise measurement of ultrasound absorption. *Acta Acustica United with Acustica*, 27(4): 173–181, 1972.

[5] N. Purdie and M. M. Farrow. The application of ultrasound absorption to reaction kinetics. *Coordination Chemistry Reviews*, 11(3):189–226, 1973.

[6] K. K. Shung. On the ultrasound scattering from blood as a function of hematocrit. *IEEE Transactions on Sonics and Ultrasonics*, 29(6):327–330, 1982.

[7] L. Y. L. Mo, I. Y. Kuo, K. K. Shung, L. Ceresne, and R. S. C. Cobbold. Ultrasound scattering from blood with hematocrits up to 100%. *IEEE Transactions on Biomedical Engineering*, 41(1):91–95, 1994.

[8] F. A. Duck. *Physical Properties of Tissue (First Edition)*, pages 99–124. Academic Press, London, 1996.

[9] T. Lin, J. Ophir, and G. Potter. Frequency-dependent ultrasonic differentiation of normal and diffusely diseased liver. *J. Acoust. Soc. Am.*, 82(4):1131–1138, 1987.

[10] F. S. Foster and J. W. Hunt. Transmission of ultrasound beams through human tissue–focusing and attenuation studies. *Ultrasound Med. Biol.*, 5(3):257–268, 1979.

[11] C. Li, N. Duric, and L. Huang. Breast imaging using transmission ultrasound: Reconstructing tissue parameters of sound speed and attenuation. In *International Conference on BioMedical Engineering and Informatics, 2008.*, volume 2, pages 708–712. IEEE, 2008.

[12] P. Laugier, P. Giat, and G. Berger. Broadband ultrasonic attenuation imaging: a new imaging technique of the os calcis. *Calcified Tissue International*, 54(2):83–86, 1994.

[13] M. Ribault, J.Y. Chapelon, D. Cathignol, and A. Gelet. Differential attenuation imaging for the characterization of high intensity focused ultrasound lesions. *Ultrasonic Imaging*, 20(3):160–177, 1998.

[14] L. Bjørnø. Introduction to nonlinear acoustics. *Physics Procedia*, 3(1):5–16, 2010.

[15] P. N. Wells. Ultrasonic imaging of the human body. *Reports on Progress in Physics*, 62 (5):671, 1999.

[16] P. J. Westervelt. Parametric acoustic array. *The Journal of the Acoustical Society of America*, 35(4):535–537, 1963.

[17] Y. S. Lee and M. F. Hamilton. Time-domain modeling of pulsed finite-amplitude sound beams. *The Journal of the Acoustical Society of America*, 97(2):906–917, 1995.

[18] R. O. Cleveland, M. F. Hamilton, and D. T. Blackstock. Time-domain modeling of finite-amplitude sound in relaxing fluids. *The Journal of the Acoustical Society of America*, 99(6):3312–3318, 1996.

[19] J. A. R. L. E. Berntsen. Numerical calculations of finite amplitude sound beams. *Frontiers of Nonlinear Acoustics*, pages 191–196, 1990.

[20] E. Hopf. The partial differential equation ut+ uux= μxx. *Communications on Pure and Applied Mathematics*, 3(3):201–230, 1950.

[21] S. Kutluay, A. R. Bahadir, and A. Özdeş. Numerical solution of one-dimensional Burgers equation: explicit and exact-explicit finite difference methods. *Journal of Computational and Applied Mathematics*, 103(2):251–261, 1999.

[22] R. O. Illing, J. E. Kennedy, F. Wu, G. R. Ter Haar, A. S. Protheroe, P. J. Friend, F. V. Gleeson, D. W. Cranston, R. R. Phillips, and M. R. Middleton. The safety and feasibility of extracorporeal high-intensity focused ultrasound (HIFU) for the treatment of liver and kidney tumours in a Western population. *British Journal of Cancer*, 93(8): 890–895, 2005.

[23] L. Poissonnier, J. Y. Chapelon, O. Rouviere, L. Curiel, R. Bouvier, X. Martin, J. M. Dubernard, and A. Gelet. Control of prostate cancer by transrectal HIFU in 227 patients. *European Urology*, 51(2):381–387, 2007.

[24] C. C. Coussios, C. H. Farny, G. Ter Haar, and R. A. Roy. Role of acoustic cavitation in the delivery and monitoring of cancer treatment by high-intensity focused ultrasound (HIFU). *International Journal of Hyperthermia*, 23(2):105–120, 2007.

[25] F. Tranquart, N. Grenier, V. Eder, and L. Pourcelot. Clinical use of ultrasound tissue harmonic imaging. *Ultrasound in Medicine & Biology*, 25(6):889–894, 1999.

[26] R. S. Shapiro, J. Wagreich, R. B. Parsons, A. Stancato-Pasik, H. C. Yeh, and R. Lao. Tissue harmonic imaging sonography: evaluation of image quality compared with conventional sonography. *AJR. American Journal of Roentgenology*, 171(5):1203–1206, 1998.

[27] E. L. Rosen and M. S. Soo. Tissue harmonic imaging sonography of breast lesions: improved margin analysis, conspicuity, and image quality compared to conventional ultrasound. *Clinical Imaging*, 25(6):379–384, 2001.

[28] A. Hirschberg, J. Gilbert, R. Msallam, and A. P. J. Wijnands. Shock waves in trombones. *The Journal of the Acoustical Society of America*, 99(3):1754–1758, 1996.

[29] A. Kilbas, H.M. Srivastava, and J.J. Trujillo. Theory and Applications of Fractional Differential Equations, Elsevier, North-Holland Mathematics Studies, 204. *Fractional Calculus and Applied Analysis*, 9(1):71, 2006.

[30] M. Caputo. Linear models of dissipation whose Q is almost frequency independent-II. *Geophys. J. R. Astr. Soc.*, 13:529–539, 1967.

[31] A. Atangana and D. Baleanu. New fractional derivatives with nonlocal and non-singular kernel: theory and application to heat transfer model. *arXiv preprint arXiv:1602.03408*, 2016.

[32] U. N. Katugampola. A new approach to generalized fractional derivatives. *Bull. Math. Anal. Appl*, 6(4):1–15, 2014.

[33] M. Ishteva. Properties and applications of the Caputo fractional operator. *MSc. Thesis*, 2005.

[34] I. Podlubny. *Fractional Differential Equations: an Introduction to Fractional Derivatives, Fractional Differential Equations, to Methods of Their Solution and Some of Their Applications*, volume 198. Academic Press, 1998.

[35] K. Singh, R. Saxena, and S. Kumar. Caputo-based fractional derivative in fractional Fourier transform domain. *IEEE Journal on Emerging and Selected Topics in Circuits and Systems*, 3(3):330–337, 2013.

[36] S. A. Goss, R. L. Johnston, and F. Dunn. Comprehensive compilation of empirical ultrasonic properties of mammalian tissues. *J. Acoust. Soc. Am.*, 64(2):423–457, 1978.

[37] S. A. Goss, R. L. Johnston, and F. Dunn. Compilation of empirical ultrasonic properties of mammalian tissues. II. *J. Acoust. Soc. Am.*, 68(1):93–108, 1980.

[38] T. L. Szabo. Time-domain wave-equations for lossy media obeying a frequency power-law. *J. Acoust. Soc. Am.*, 96(1):491–500, 1994.

[39] J. F. Kelly, R. J. McGough, and M. M. Meerschaert. Analytical time-domain Green's functions for power-law media. *J. Acoust. Soc. Am.*, 124(5):2861–2872, 2008.

[40] M. G. Wismer. Finite element analysis of broadband acoustic pulses through inhomogenous media with power law attenuation. *J. Acoust. Soc. Am.*, 120(6):3493–3502, 2006.

[41] W. Chen and S. Holm. Fractional Laplacian time-space models for linear and nonlinear lossy media exhibiting arbitrary frequency power-law dependency. *J. Acoust. Soc. Am.*, 115(4):1424–1430, 2004.

[42] B. E. Treeby and B. T. Cox. Modeling power law absorption and dispersion for acoustic propagation using the fractional Laplacian. *J. Acoust. Soc. Am.*, 127(5):2741–2748, 2010.

[43] P. He. Simulation of ultrasound pulse propagation in lossy media obeying a frequency power law. *IEEE Trans. Ultrason. Ferroelect. Freq. Contr.*, 45(1):114–125, 1998.

[44] K. R. Waters, M. S. Hughes, J. Mobley, G. H. Brandenburger, and J. G. Miller. On the applicability of Kramers-Kronig relations for ultrasonic attenuation obeying a frequency power law. *J. Acoust. Soc. Am.*, 108(2):556–563, 2000.

[45] T. L. Szabo. Causal theories and data for acoustic attenuation obeying a frequency power-law. *J. Acoust. Soc. Am.*, 97(1):14–24, 1995.

[46] D. T. Blackstock. Transient solution for sound radiated into a viscous fluid. *J. Acoust. Soc. Am.*, 41(5):1312–1319, 1967.

[47] J. P. Nolan. Numerical calculation of stable densities and distribution functions. *Commun. Statist. Stoch. Models*, 13(4):759–774, 1997.

[48] M. J. Buckingham. Causality, Stokes' wave equation, and acoustic pulse propagation in a viscous fluid. *Phys. Rev. E Stat. Nonlin. Soft Matter Phys.*, 72(2 Pt 2):026610, 2005.

[49] J. P. Nolan. User Manual for STABLE 5.1. 2009.

[50] D. Chen, J. F. Kelly, and R. J. McGough. A fast nearfield method for calculations of time-harmonic and transient pressures produced by triangular pistons. *J. Acoust. Soc. Am.*, 120(5):2450–2459, 2006.

[51] J. F. Kelly and R. J. McGough. A time-space decomposition method for calculating the nearfield pressure generated by a pulsed circular piston. *IEEE Trans. Ultrason. Ferroelect. Freq. Contr.*, 53(6):1150–1159, 2006.

[52] T. L. Szabo. The material impulse response for broadband pulses in lossy media. *IEEE Symposium on Ultrasonics*, 1:748–751, 2003.

[53] X. Zhao and R. J. McGough. Time-domain comparisons of power law attenuation in causal and noncausal time-fractional wave equations. *The Journal of the Acoustical Society of America*, 139(5):3021–3031, 2016.

[54] S. Holm and R. Sinkus. A unifying fractional wave equation for compressional and shear waves. *J. Acoust. Soc. Am.*, 127(1):542–548, 2010.

[55] S. Holm and S. P. Näsholm. A causal and fractional all-frequency wave equation for lossy media. *J. Acoust. Soc. Am.*, 130(4):2195–2202, 2011.

[56] G. Pantis. The evaluation of integrals with oscillatory integrands. *Journal of Computational Physics*, 17(2):229–233, 1975.

[57] P. K. Kythe and M. R. Schäferkotter. *Handbook of Computational Methods for Integration*. CRC Press, 2004.

[58] L. N. G. Filon. III.-On a Quadrature Formula for Trigonometric Integrals. *Proceedings of the Royal Society of Edinburgh*, 49:38–47, 1930.

[59] J. E. T. Penny and G. R. Lindfield. *Numerical Methods Using Matlab*. Upper Saddle River, NJ : Prentice Hall, 2nd edition, 2000. ISBN 0130126411 (paper). Previous ed.: 1995.

[60] P. J. Davis and P. Rabinowitz. *Methods of Numerical Integration*. Courier Corporation, 2007.

[61] B. E. Treeby and B. T. Cox. A k-space Green's function solution for acoustic initial value problems in homogeneous media with power law absorption. *J. Acoust. Soc. Am.*, 129(6):3652–3660, 2011.

[62] E. A. Zabolotskaya. Quasiplane waves in the nonlinear acoustics of confined beams. *Sov. Phys. Acoust.*, 15:35–40, 1969.

[63] V. P. Kuznetsov. Equation of nonlinear acoustics. *Sov. Phys. Acoust.*, 16(4):467–470, 1971.

[64] J. E. Soneson. A parametric study of error in the parabolic approximation of focused axisymmetric ultrasound beams. *The Journal of the Acoustical Society of America*, 131 (6):EL481–EL486, 2012.

[65] F. P. Curra, P. D. Mourad, V. A. Khokhlova, R. O. Cleveland, and L. A. Crum. Numerical simulations of heating patterns and tissue temperature response due to high-intensity focused ultrasound. *IEEE Transactions on Ultrasonics, Ferroelectrics, and Frequency Control*, 47(4):1077–1089, 2000.

[66] E. A. Filonenko and V. A. Khokhlova. Effect of acoustic nonlinearity on heating of biological tissue by high-intensity focused ultrasound. *Acoustical Physics*, 47(4):468–475, 2001.

[67] J. Huijssen and M. D. Verweij. An iterative method for the computation of nonlinear, wide-angle, pulsed acoustic fields of medical diagnostic transducers. *The Journal of the Acoustical Society of America*, 127(1):33–44, 2010.

[68] G. Mur. Absorbing boundary conditions for the finite-difference approximation of the time-domain electromagnetic-field equations. *IEEE Transactions on Electromagnetic Compatibility*, (4):377–382, 1981.

[69] J. P. Berenger. A perfectly matched layer for the absorption of electromagnetic waves. *Journal of Computational Physics*, 114(2):185–200, 1994.

[70] D. S. Katz, E. T. Thiele, and A. Taflove. Validation and extension to three dimensions of the Berenger PML absorbing boundary condition for FD-TD meshes. *IEEE Microwave*

and Guided Wave Letters, 4(8):268–270, 1994.

[71] X. Yuan, D. Borup, J. W. Wiskin, M. Berggren, R. Eidens, and S. A. Johnson. Formulation and validation of Berenger's PML absorbing boundary for the FDTD simulation of acoustic scattering. *IEEE Transactions on Ultrasonics, Ferroelectrics, and Frequency Control*, 44(4):816–822, 1997.

[72] Q. H. Liu and J. Tao. The perfectly matched layer for acoustic waves in absorptive media. *The Journal of the Acoustical Society of America*, 102(4):2072–2082, 1997.

[73] Q. H. Liu. Perfectly matched layers for elastic waves in cylindrical and spherical coordinates. *The Journal of the Acoustical Society of America*, 105(4):2075–2084, 1999.

[74] S. Abarbanel, D. Gottlieb, and J. S. Hesthaven. Well-posed perfectly matched layers for advective acoustics. *Journal of Computational Physics*, 154(2):266–283, 1999.

[75] F. Q. Hu. On absorbing boundary conditions for linearized euler equations by a perfectly matched layer. *Journal of Computational Physics*, 129(1):201–219, 1996.

[76] Y. L. Sheu and P. C. Li. Simulations of photoacoustic wave propagation using a finite-difference time-domain method with Berenger's perfectly matched layers. *The Journal of the Acoustical Society of America*, 124(6):3471–3480, 2008.

[77] Y. Ma, J. Yu, and Y. Wang. A novel unsplit perfectly matched layer for the second-order acoustic wave equation. *Ultrasonics*, 54(6):1568–1574, 2014.

[78] J. H. Ehrlich. Time domain modeling of acoustic propagation with acoustic wave propagator and absorbing boundary conditions. *Journal of the Acoustical Society of America*, 123(5):3530, 2008.

[79] G. F. Pinton, J. Dahl, S. Rosenzweig, and G. E. Trahey. A heterogeneous nonlinear attenuating full-wave model of ultrasound. *IEEE Transactions on Ultrasonics, Ferroelectrics, and Frequency Control*, 56(3), 2009.

[80] B. Kaltenbacher, M. Kaltenbacher, and I. Sim. A modified and stable version of a perfectly matched layer technique for the 3-d second order wave equation in time domain with an application to aeroacoustics. *Journal of Computational Physics*, 235:407–422, 2013.

[81] Z. Chen and X. Wu. Long-time stability and convergence of the uniaxial perfectly matched layer method for time-domain acoustic scattering problems. *SIAM Journal on Numerical Analysis*, 50(5):2632–2655, 2012.

[82] E. J. Alles and K. W. van Dongen. Perfectly matched layers for frequency-domain integral equation acoustic scattering problems. *IEEE Transactions on Ultrasonics, Ferroelectrics, and Frequency Control*, 58(5):1077–1086, 2011.

[83] T. K. Katsibas and C. S. Antonopoulos. A general form of perfectly matched layers for for three-dimensional problems of acoustic scattering in lossless and lossy fluid media.

IEEE Transactions on Ultrasonics, Ferroelectrics, and Frequency Control, 51(8):964–972, 2004.

[84] K. Duru. A perfectly matched layer for the time-dependent wave equation in heterogeneous and layered media. *Journal of Computational Physics*, 257:757–781, 2014.

[85] D. T. Blackstock. Connection between the Fay and Fubini solutions for plane sound waves of finite amplitude. *The Journal of the Acoustical Society of America*, 39(6): 1019–1026, 1966.